Development of a nanofabricated magnetometer at very low temperature (30 mK) and high magnetic field (16 T) : new magnetic states in frustrated nanomagnets

Ovidiu Florea

Communauté
UNIVERSITÉ Grenoble Alpes

THÈSE

Pour obtenir le grade de

DOCTEUR DE LA COMMUNAUTÉ UNIVERSITÉ GRENOBLE ALPES

Spécialité : Physique de la Matière Condensée et du Rayonnement

Arrêté ministériel : 25 mai 2016

Présentée par

Ovidiu FLOREA

Thèse dirigée par **Rafik (phys) BALLOU**, , , et
codirigée par **Elsa (phys) LHOTEL** Chargée de Recherche , CNRS

préparée au sein du **Laboratoire Institut Néel**
dans **l'École Doctorale Physique**

Développement d'un magnétomètre nanofabriqué très basse température (30 mK) et fort champ magnétique (16 T) - Etude de nouveaux états magnétiques apparaissant dans les nanoaimants frustrés

Development of a nanofabricated magnetometer at very low temperature (30 mK) and high magnetic field (16 T) - New magnetic states in frustrated nanomagnets

Thèse soutenue publiquement le **21 décembre 2015**,
devant le jury composé de :

Monsieur RAFIK BALLOU
DIRECTEUR DE RECHE, CNRS DELEGATION ALPES, Directeur de these
Madame ELSA LHOTEL
CHARGE DE RECHERCHE, CNRS DELEGATION ALPES, CoDirecteur de these
Monsieur ERIC VINCENT
DIRECTEUR DE RECHERCHE, CEA SACLAY, Rapporteur
Monsieur SEAN GIBLIN
MAITRE DE CONFERENCES, UNIVERSITE DE CARDIFF - GRANDE-BRETAGNE, Rapporteur
Monsieur ILYA SHEIKIN
DIRECTEUR DE RECHERCHE, CNRS DELEGATION ALPES, Président
Monsieur FABRICE BERT
PROFESSEUR, UNIVERSITE PARIS-SUD, Examinateur

Contents

Introduction

This thesis had two objectives. The main objective was the development of a Faraday force magnetometer that will enable absolute magnetization measurements under extreme conditions: very low temperature (30 mK), high magnetic fields (16 T) and small samples. Second, the use of this unique magnetometer to probe the consequences of magnetic frustration in quantum molecular magnets.

The main effort during my PhD was made on the experimental set-up. The performance of our magnetometer were chosen to complement the existing instruments of very low temperature magnetometry in Grenoble, namely: i) a micro-SQUID magnetometer (30 mK, 3 T) and a micro-Hall probe magnetometer (30 mK, 7 T), (W. Wernsdorfer, Néel Institute), ii) a scanning micro-SQUID magnetometer (50 mK, 0.1 T), (K. Hasselbach, Néel Institute), iii) two very low temperature SQUID magnetometers (60 mK, 8T) (C. Paulsen, Néel Institute) and iv) a torque magnetometer (40 mK, 34 T) allowing the measurement of the perpendicular components of the magnetization (I. Sheikin, LNCMI-G). Our magnetometer will thus contribute to making Grenoble a unique center of high sensitivity and low temperature magnetometry in a large range of magnetic fields.

Faced with extreme conditions, 30 mK - 16 T, we have chosen a magnetometer using a capacitive detection of the Faraday force, which is especially suited for high fields and low temperature measurements. Up to this date, only a few Faraday magnetometers which operate at very low temperatures exist. The first design is in the group of Sakakibara in Japan [1]. They can perform magnetization measurements down to 100 mK and up to 15 T with a sensitivity of 10^{-4} emu. Recently, a second device was developed in United Kingdom in the group of Mackenzie [2]. They can perform fast sweep-rate magnetization measurements down to 50 mK and in applied magnetic fields up to 15 T with a sensitivity of 10^{-5} emu. We aim to achieve at least the same sensitivity of 10^{-5} emu. In addition, we will expand the variety of magnetic samples that we can measure (different sample forms and sensitivity requirements).

In parallel to my construction of the magnetometer, I have been involved in the experimental study of frustrated magnets. A magnet is generically identified as being frustrated when it is impossible to simultaneously minimize all the interactions between its magnetic moments. This might arise from competition between exchange interactions or exchange pathways, which defines exchange frustration.

It can also, even for first neighbor exchange interactions only, result from the nature of the magnetic moments network (geometric units and connectivity), which defines geometric frustration. A main outcome in certain instances is that there are infinite numbers of moment configurations of the same energy, which prevents the system to condense into a Néel order. Unconventional phases can then be stabilized, either through secondary mechanisms leading to complex freezing of the magnetic moments or through more subtle mechanisms leading to unexpected dynamical states, of which the spin liquids and spin ices had been illustrative examples in the past. A wealth of additional novel phases should emerge when the quantum nature of the moments cannot be ignored.

I considered during my thesis two oxide compounds: $Gd_3Ga_5O_{12}$ (GGG) and $Gd_3Al_5O_{12}$ (GAG), which can be considered as examples of classical frustrated magnets. I was also interested in two copper based molecular magnets, which were anticipated as possible examples of quantum frustrated magnets: i) the cluster $[Cu_{44}(\mu_8\text{-}Br)_2\text{-}(\mu_3\text{-}OH)_{36}(\mu\text{-}OH)_4(ntp)_12Br_8(OH_2)_{28}]Br_2 \cdot 81H_2O$ (Cu_{44}) made of frustrated tetrahedra, in which we aimed to study the role of frustration in finite quantum frustrated systems, and ii) the extended system $\{Cu_3Cs(\mu Cl)_3(Hntp)_2(H2O)_3\}_\infty$ (Cu_3), made of frustrated triangles arranged on a kagome lattice, with alternating strong and weak exchange interactions, in which we aimed to study the role of hierarchic interactions as a function of temperature.
I investigated their properties by magnetization measurements making use of the already available magnetometers at the Néel Institute. In the case of GGG, I also participated to a polarized neutron elastic experiment at the Institut Laue Langevin in Grenoble.

Accordingly, my thesis is divided into two main parts. In the first part, I present the instrumental development. I start, as a first chapter, by introducing the principle of a Faraday force magnetometer. Since the aim for our magnetometer is to operate at very low temperatures, down to 30 mK, I briefly present in a second chapter the principle of the dilution refrigerator, the only refrigerator that permits to reach temperatures below 300 mK in a continuous mode. I then emphasize the dimensions of our dilution refrigerator, its characterization and optimization. In a third chapter I detail the characteristics of the main coil providing the magnetic field of 16 T and of the coils producing the field gradient. In a fourth chapter, I describe two capacitive sensors, a nanofabricated microelectromechanical system (MEMS), designed to reach high sensitivities, and a plastic sample holder, designed

for compounds with larger magnetic moments. In a fifth chapter, I discuss about the capacitive detection. We developed in this context a cold amplifier stage (4 K) in order to increase the sensitivity of our device. I end this first part of the thesis with a partial conclusion indicating that, unfortunately, the magnetometer is not yet fully operational. I indeed encountered different technical problems that are discussed. Solutions are proposed of which some are in order to be implemented.

In the second part of the thesis, I present my magnetic study on several frustrated compounds. I start with a first chapter presenting the experimental methods that I used, then I recall in a second chapter some of the outcomes of magnetic frustration. In a third chapter, I describe my experimental study of the GGG frustrated oxide compounds by systematic and thorough magnetization measurements, on a polycrystalline sample and on a single crystal. The aim was to get more insights into its extremely complex H T phase diagram. Neutron diffraction was carried out on the same polycrystalline sample as the one measured on the magnetometers, to prevent us from inconsistencies in the results, as existing in the literature, that might be answerable to possible sample dependent properties. A specific point, at which all phases seem to converge, appears to emerge in the H T phase diagram. In a fourth chapter, I report on my magnetization measurements on a polycrystalline sample of GAG, which I carried out to check the robustness of the GGG magnetic phases. In a fifth chapter, I discuss the magnetization measurements I have performed on the Cu_{44} and the Cu_3 molecular magnets. These compounds unfortunately revealed themselves inadequate or unsuccessful for the study of quantum frustration either because they presented complex exchange interaction paths, involving both intercluster and intracluster interactions, as in the case of Cu_{44}, or they showed so far unexplained chemical structural aging effects, as in the case of Cu_3. I end this second part of the thesis again with a partial conclusion.

Part I

Faraday Force Magnetometer

Introduction au magnétomètre de Faraday

Dans ce chapitre, je présente les objectifs du développement instrumental de cette thèse: construire un magnétomètre à force de Faraday pour réaliser des mesures absolues de l'aimantation à très basse température (30 mK) et sous fort champ magnétique (16 T), avec une sensibilité de 10^{-8} A.m^2.

Pour cela, j'introduis les différentes techniques de mesures d'aimantation, et justifie le choix d'un magnétomètre à force de Faraday avec une détection capacitive. Cette technique est effectivement parfaitement adaptée aux mesures à très basse température et en fort champ magnétique.

Je détaille ensuite le principe d'un tel magnétomètre, basé sur la force de Faraday induite par l'aimantation en présence d'un gradient de champ. Je précise les points clés de sa conception. Deux électrodes en regard définissent une capacité initiale. L'une est mobile et peut se déplacer sous l'effet de la force de Faraday, induisant ainsi une variation de capacité que l'on va mesurer. Les paramètres permettant d'améliorer directement la sensibilité sont la valeur du gradient de champ et la raideur des ressorts permettant à la membrane de se déplacer.

Enfin, je présente l'état de l'art de ce type de magnétomètres. Deux prototypes existent actuellement capables de travailler à très basse température et sous fort champ magnétique: l'un construit au Japon par T. Sakakibara, et l'autre développé récemment au Royaume-Uni dans l'équipe de A. Mackenzie.

Chapter 1

Introduction

1.1 Experimental techniques for magnetization measurements

Different methods exist to assess the response of a material to the applied magnetic field. A classification can be made depending on the physical quantity which is measured:

- *Macroscopic techniques* provide information about the bulk properties of the material. The most common devices are the vibrating sample magnetometer (VSM), superconducting quantum interference device (SQUID) or the extraction magnetometer. These different techniques provide absolute values of the magnetization in a wide range of temperatures and applied magnetic field. In these devices, the sample is placed into detection coiled coupled inductively with the sensor. A different type of magnetometer is the Faraday Force Magnetometer. In that case, the magnetization is determined through the measurement of the displacement induced by the Faraday force.

- *Microscopic techniques* probe directly the properties of the magnetic spin itself, for example through the interaction between the magnetic spins and an incident particle. They can provide information on the local environment of the magnetic spin, but also on the arrangement of these spins inside the lattice. A few examples of such techniques are neutron scattering (detailed

in section 2.2), nuclear magnetic resonance spectroscopy (NMR), muon spin spectroscopy (μSR) and Mossbauer spectroscopy .

- *Local techniques* provide information about the magnetization through the measurement of the magnetic field at the surface of the materials. The most common used devices are the micro Hall probe or the micro SQUID. They have a great sensitivity, but they do not provide absolute value of magnetization.

The goal of this thesis was the development of a new magnetometer which can provide absolute magnetization measurements at temperatures down to 30 mK and under applied magnetic fields up to 16 T with a sensitivity of 10^{-8} A·m^2 (10^{-5} emu). When absolute values of magnetization are required, we have to choose among the macroscopic technique devices. Even if all these devices have been successfully applied over a large ranges of temperatures and applied magnetic fields, each one has its advantages and disadvantages. A VSM can work without any problem in high applied magnetic fields, however is not as suitable at very low temperatures where vibrations and eddy current heating can affect the measurement. A SQUID is a highly sensitive magnetometer but the use of superconducting materials makes it unsuitable for applied magnetic fields higher than 12 T. A Faraday force magnetometer is suitable for very low temperatures and high magnetic fields but it is susceptible to torque and has a lower sensitivity than conventional magnetometers.
Magnetization measurements which require magnetic fields larger than 12 T prevent the use of SQUID sensors and the VSM is not reliable at very low temperatures. Therefore, we opted for a Faraday Force Magnetometer.

1.2 Principle of the Faraday Force Magnetometer

In a Faraday Force Magnetometer, the magnetization, M, is obtained by measuring the Faraday force, F, exercised on a magnetic sample placed in a magnetic field gradient

$$\vec{F} = \vec{M} \cdot \nabla \vec{B} \tag{1.1}$$

where $\vec{F}$ is the Faraday force and $\vec{B}$ is the magnetic field gradient.

There are various methods to measure the Faraday force. Figure 1.1 shows the capacitive detection method which is especially suited for measurements in our extreme conditions: very low temperature and high magnetic field. A sample

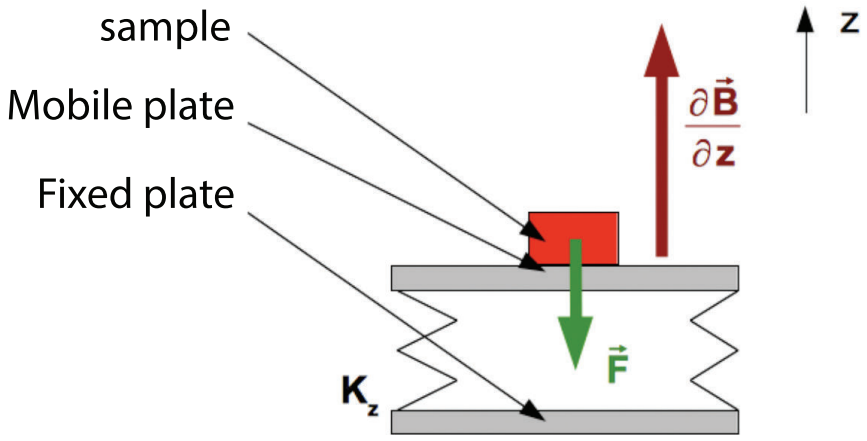

FIGURE 1.1: Principle of the magnetization measurements in a Faraday force magnetometer with a capacitive detection

holder is made out of two parallel metallic plates faced to each other. A movable plate is supported by springs above a fixed plate and they form the two electrodes of a capacitor. The magnetic sample is mounted on the movable plate and once a field gradient is applied, a Faraday force is exerted. We assume that the Faraday force is perpendicular to the two plates of the capacitor. The created force will then create a displacement of the movable plate, until the resorting force of the springs will balance it.

For small deflections of the springs, the plate's displacement is proportional to the Faraday force and can be detected as a change in capacitance ΔC. Assuming a field gradient along the z direction, we can write:

$$F_z = M_z \cdot \frac{\partial B}{\partial z} = K_z \Delta d \tag{1.2}$$

where K_z is the stiffness of the springs, and Δd the induced displacement. The resulting capacitance is:

$$C = C_0 + \Delta C = \frac{\epsilon_0 S}{d_0 \quad \Delta d} \tag{1.3}$$

where d_0 is the initial gap between the two electrodes of the capacitor, C_0 is the initial capacitance value, S the surface of the electrodes and ΔC the variation of

capacitance when the Faraday force is exerted. It results that

$$\frac{\Delta C}{C_0} = \frac{\Delta d}{d_0} \tag{1.4}$$

From the above equations, we can observe that the sensitivity of the measurement can be increased in two ways: either by changing the field gradient or by reducing the initial distance between the two electrodes of the capacitor. For this reason, we decided to work with gap as small as possible, and to design a nanofabricated capacitive sensor as I will later describe.

Another important aspect is to ensure that the displacement of the movable plate happens only in the z direction. In the case of anisotropic materials, the magnetization is not always parallel to the applied magnetic field. If that is the case, a component of the magnetization in the xy direction may be observed. If the sample holder can move on the xy direction, the sample will create lateral displacements with different capacitive values and it will not be possible to access the absolute value of the magnetization along z anymore.
Thus, the main drawback of this method is the change in the capacitance due to torque effects. Therefore, a proper treatment of the stiffness of the strings in the z direction compared to the x and y directions is required.

1.3 State of the Art

To my knowledge, up to this date, only a couple of Faraday magnetometers which are working at very low temperature exists. The first design is in the group of Sakakibara in Japan [1]. A schematic view of the capacitive sensor is shown in figure 1.2 left. The movable plate, made of epoxy, is supported by two pairs of phosphor-bronze crossed wires (0.1-0.2 mm diameter). The movable plate has a 10 mm diameter with a gap of 0.1 mm which results in an unloaded capacitance of 7 pF. The design of the crossed wires ensures that the movable plate is less sensitive to radial forces or to torque. The capacitance of the sensor is acquired with a commercial capacitor bridge, Andeen-Hagerling 2500A.
The main coil produces magnetic fields up to 15 T with a 10^{-5} homogeneity for a 10 mm spherical volume diameter. The magnetic coils used to create the field gradient are situated outside of the main coils and can provide a field gradient up to 10 T/m. For a field gradient of 10 T/m they are able to perform magnetization

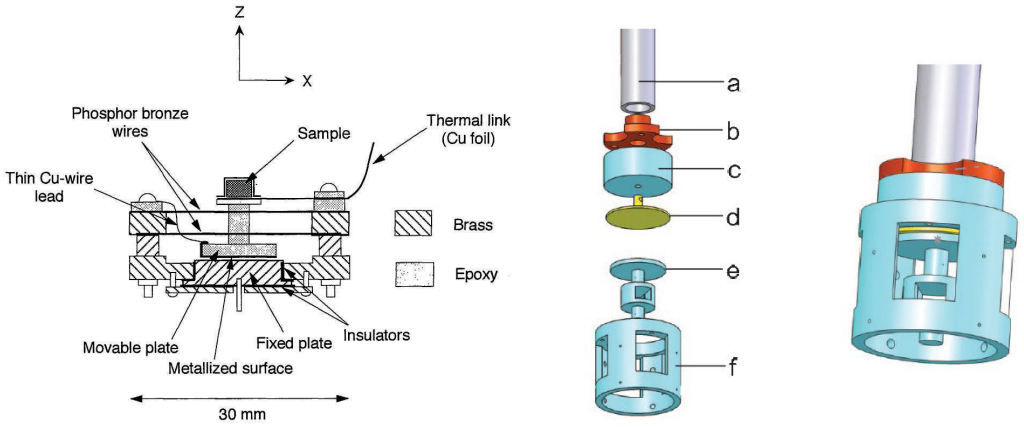

FIGURE 1.2: Faraday force magnetometer with a capacitive detection. Left: Sakakibara's design (from Ref. [1]. Right: Slobinsky's design (from Ref. [2]).

measurements down to 100 mK in magnetic fields up to 10 T with a sensitivity of 10^{-7} A.m^2.

A second Faraday Magnetometer was recently developed in the group of Mackenzie in United Kingdom [2]. They use the same principle of a capacitive detection but they changed the design of the sample holder (figure 1.2 right) to be suitable for their fast sweep rates measurements. Because of the large sweeping rates, they opted for a sample holder made out of insulating materials (Tufset–Tufnol Composites Limited) in order to avoid heating due to eddy currents. It is made out of two components with an inverse design compared to Sakakibara's group. The first component includes the fixed plate and it is connected to the mixing chamber. The second component consists of a body which can be screwed in the first component and the sample holder (which includes the movable plate). With this design, they have the control of the initial value of the capacitance. The capacitance of the sensor is acquired with a commercial capacitor bridge, Andeen-Hagerling 2500A. The top electrode is made out of brass, but the movable plate is made out of tufset. Therefore it is painted with silver paste and connected to the magnetometer body with a 25 μm gold wire. The sample holder is fixed in position by two pairs of 0.19 mm diameter nylon fishing line. They have available a 4 x 3 mm^2 space in the z plane which is suitable for thin magnetic samples.
The main coil produces magnetic fields up to 15 T and two superconducting Helmholtz gradient field coils, placed between the main coils and the calorimeter, produces field gradients of less than 1 T/m. For a field gradient of 1 T/m

they can perform magnetization measurements down to 50 mK in magnetic fields up to 15 T with a sensitivity of 10 ^{8} A.m^2.

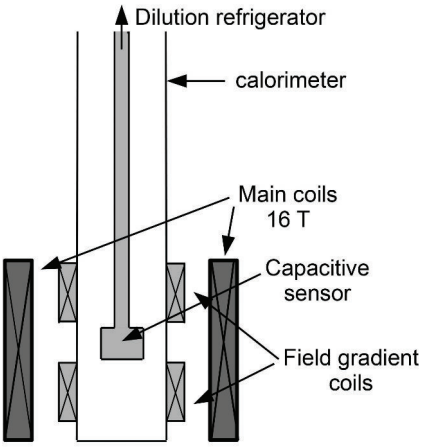

FIGURE 1.3: Faraday magnetometer: schematic view of the capacitive sensor, main and field gradient coils.

Our Faraday force magnetometer will use the same capacitive detection proven to be suitable for very low temperature measurements. The main and field gradient coils, as well as the capacitive sensor are schematically presented in figure 1.3. The sample holder is positioned between resistive copper magnetic coils which can provide a vertical field gradient of 3.7 T/m.A (see section 3). Around the calorimeter and the field gradient coils we have a superconducting main coil which can provide fields up to 16 T (we possess a 16 T superconducting coil but a higher field coil could replace the actual one).

We will aim to achieve at least the same sensitivity as the Mackenzie group, but we will try to expand the variety of magnetic samples that we can measure (different sample forms and sensitivity requirements). For that we developed two sample holders which will be described in chapter 4. In addition, we created a home made capacitance bridge with a cold amplifier stage to achieve the desired sensitivity described in chapter 5.

In the following part, I will present our Faraday force magnetometer. First, I will focus on the principle of the dilution refrigerator and in the second part I will present all the components of the magnetometer and the preliminary tests we performed.

Le réfrigérateur à dilution

L'un des éléments clés de notre magnétomètre est la nécessité de travailler à très basse température. Dans ce chapitre, je présente le moyen d'obtenir des très basses températures de façon continue: le réfrigérateur à dilution.

J'introduis tout d'abord le principe du fonctionnement du réfrigérateur à dilution, basé sur la circulation d'un mélange d'Helium 3 et d'Helium 4, et ses différentes composantes: boîte à 1 K, bouilleur et boîte à mélange.

Je présente ensuite le réfrigérateur à dilution que j'ai utilisé au cours de ma thèse. Il a été construit au laboratoire, et n'avait pas été mis en fonctionnement à mon arrivée. Je détaille donc ses dimensions, les précautions prises pour le câblage des fils de mesure, et les thermomètres utilisés pour le caractériser et mesurer la température à différents points du système.

J'en viens ensuite à l'optimisation du réfrigérateur à dilution lui-même en présentant les différentes procédures utilisées. i) circulation d'Helium 4 seul pour s'assurer de l'absence de superfuites. ii) injection petit à petit du mélange ^{3}He-^{4}He pour déterminer la quantité optimale nécessaire au bon fonctionnement du réfrigérateur. iii) tests de puissance pour caractériser le réfrigérateur et son point de fonctionnement optimal (ajustement de la température du bouilleur).

En parallèle, je détaille toutes les difficultés que nous avons rencontrées: superfuite, changement d'impédance, instabilité de fonctionnement.
Nous avons pu déterminer les meilleurs conditions de fonctionnement: 36 L de mélange ^{3}He-^{4}He, avec une quantité d'Helium 3 estimée à 25 %, bouilleur à 850 mK, qui nous ont permis d'obtenir une température minimale d'environ 40 mK avec une puissance froide de 20 μW à 100 mK.
Cependant, par la suite ces performances se sont dégradées sans que nous puissions en déterminer la cause, malgré des tests systématiques sur chacune des parties de

la dilution. Nous avons conclu que ces problèmes étaient peut-être associés à un défaut dans la conception mécanique, qui aurait aussi nui à la mesure magnétique elle-même. Nous avons donc décidé de redessiner et reconstruire complètement la partie basse ($T < 4$ K) du réfrigérateur.

Chapter 2

The Dilution Refrigerator

2.1 Principle

The principle of the dilution refrigerator was proposed by London at the beginning of the 1951 [3], but the first realization was made only 15 years later by Das et al [4]. Even now, the ^{3}He-^{4}He dilution refrigerators are the most convenient refrigerators that permit to reach temperatures below 300 mK in a continuous mode. In fact, the ^{3}He-^{4}He dilution refrigerators are the most common devices for temperatures below 1 K, with the minimum temperature achieved in the mK range.
A dilution refrigerator is based on the properties of ^{3}He and ^{4}He mixtures. It can be understood once the properties of the mixture is known. The phase diagram of the ^{3}He-^{4}He mixture is presented in figure 2.1. To illustrate the behavior of the mixture we choose as an example a 50/50 percentage of ^{3}He and ^{4}He which is cooled down along the vertical line. Above 1.3 K, the liquid exists as a normal fluid of ^{3}He and ^{4}He in solution, but below it becomes superfluid. At 0.78 K, point A in figure 2.1 left, a phase separation occurs, with the formation of a new ^{3}He-rich "concentrated" phase and a new ^{4}He-rich "dilute" phase. As we further cool down the mixture, the difference between the two phases gradually widens. A remarkable feature of the mixture is that at the lowest temperature the concentrated phase consists of pure ^{3}He, but the dilute phase still contains around 6.4% of ^{3}He at 0 bar pressure. This finite concentration is the property which allows ^{3}He-^{4}He dilution refrigerators to reach very low temperatures. A detailed study on the properties of the ^{3}He and ^{4}He can be found for example in the book of F. Pobell [5].

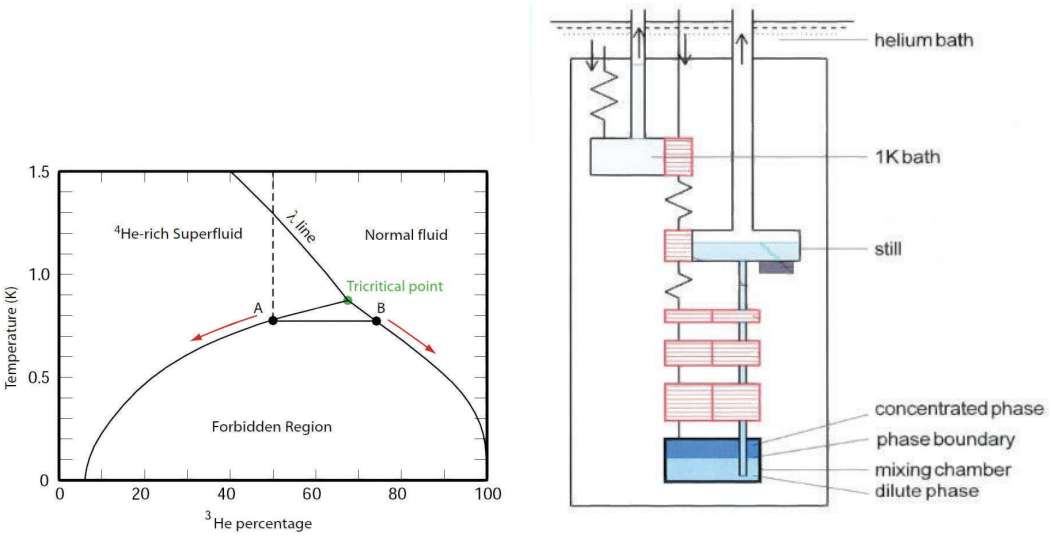

FIGURE 2.1: Left: phase diagram of liquid ^{3}He-^{4}He mixture. The critical point occurs at 0.87 K below which the liquid separates into a ^{4}He rich phase and one rich in ^{3}He. Right: schematic view of a dilution refrigerator.

Figure 2.1 right shows a schematic view of a ^{3}He-^{4}He dilution refrigerator. The mixture is first precooled by a liquid ^{4}He bath at 4.2 K. Then it is condensed around 1.5 K through a second ^{4}He bath which is pumped, commonly known as the 1 K pot. Below the 1 K pot there is a flow impedance which has the role to sustain the necessary pressure for the incoming mixture to condense. The liquid then flows through heat exchangers inside a still at a temperature around 0.7 K. Two inter-penetrated heat exchangers connects the still to the mixing chamber where the phase separation occurs. Actually, the volume of ^{3}He and ^{4}He are adjusted so that the phase boundary is situated in the mixing chamber. Because of its lower density, the concentrated ^{3}He phase floats on top of the dilute phase. In the still there is mainly ^{4}He liquid with a small concentration of ^{3}He liquid (typically around 1 %). By applying heat on the still and then pumping on it with an external pump, a flow of mainly ^{3}He vapor is created in the closed circuit. By pumping ^{3}He from the still, the concentration will decrease which develops an osmotic pressure difference that will drive ^{3}He from the mixing chamber into the still. Because the concentration of ^{3}He is finite at low temperatures, a flow of ^{3}He from the concentrated to the dilute phase is thus created.

The cooling power of a dilution refrigerator is achieved in the process of driving ^{3}He from the rich to the dilute phase. The cooling capacity in the ^{3}He-^{4}He mixture

is two fold. On one hand, the enthalpy, ΔH, given by

$$\Delta H \sim \int \Delta C dT \tag{2.1}$$

where ΔC is the difference between the specific heats of the two phases.
The second quantity is the concentration of the dilute phase, x, but at very low temperatures ($T < 0.1$ K) it is expected to be constant. How the specific heats of the concentrated and dilute phase are proportional to the temperature in this regime, the cooling power of the ^{3}He-^{4}He dilution refrigerator is

$$\dot{Q} \sim x\Delta H \sim T^2 \tag{2.2}$$

In practice, for $T < 0.1$ K, the cooling power is given by

$$\dot{Q} = 84\dot{n}_3(T^2 \quad T_0^2) \tag{2.3}$$

where T_0 is the minimum temperature of the dilution refrigerator.
In order to increase the ^{3}He flow, the still is heated without exceeding ~ 0.9 K. The cold flow of ^{3}He from the mixing chamber to the still is used to precool the incoming ^{3}He in the inter-penetrated heat exchangers. The circulating ^{3}He gas is condensed back to liquid by the 1 K pot and returns to the mixing chamber creating the continuously operating refrigerator.
The performance of any dilution refrigerator is therefore characterized by its minimum temperature and its cooling power.

2.2 Our dilution refrigerator

When I started my Phd, I had a dilution refrigerator developed and built at the Néel Institute (Cryogenic service: Y. Launay, G. Pont, G. Donnier-Valentin, S. Triqueneaux). It was not optimized or characterized, therefore my first job put it into operation. The main components of our dilution refrigerator are:

- The dilution refrigerator is placed in a vacuum stainless steel calorimeter.
- The calorimeter is immersed in a ^{4}He cryostat, which is the first cooling stage of the ^{3}He-^{4}He mixture.

- Because we perform magnetization measurements, a 16 T superconducting coil is used. The superconducting coil is in fact a 14 T coil at 4.2 K and by pumping on the ^{4}He bath, magntic fields up to 16 T can be obtained.
- The design of the main coil support imposes the dimension of the 4 K flange: 83 mm (see figure 2.2).
- The design of the magnetic coil imposes that the field gradient coils are placed between the calorimeter and the main coils which reduced the available space for the very low temperature part of the dilution refrigerator

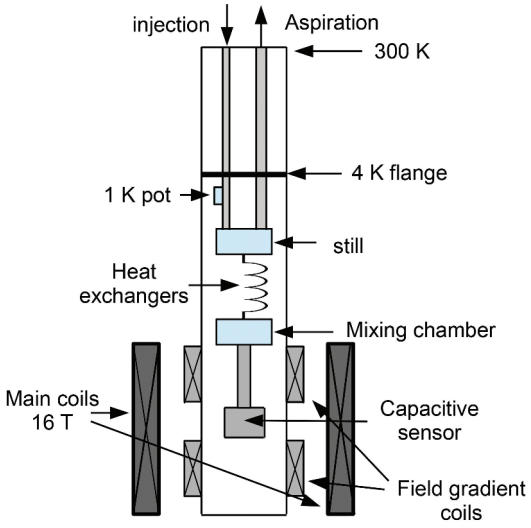

FIGURE 2.2: Schematic view of the position of the main and field gradient coils compared to the low part of the dilution refrigerator.

The main components of the low temperature part of our dilution refrigerator are presented in figure 2.3 left. It is composed of:

- The first cooling stage of the mixture is the ^{4}He bath.
- The second cooling stage is made with the use of a 1 K pot. It usually works at 1.2 K at a pressure of 0.6 mbar.
- Below the 1 K pot, a flow impedance made of copper-nickel is used to ensure the desired pressure to condensate the mixture. It is a cylindrical tube of 83 μm diameter and 1.4 m long.
- The still and the mixing chamber are made of copper and have roughly the same size: 45 mm diameter and 21 mm height. To ensure the thermal

isolation, we separated them by a 25 cm long fiberglass rod. Inside the mixing chamber, a $\sim$ 2 mm hight sintered silver powder ensures a better thermal heat exchange with the ^{3}He-^{4}He mixture.

- Between the still and the mixing chamber, the mixture flows through cylindrical copper-nickel heat exchangers. The heat exchangers are made of a small tube (injection) which passes through a larger one (aspiration).

- Because we perform magnetization measurements in high magnetic fields and our mixing chamber is made out of copper, we placed it at the upper part of the main coil (see figure 2.2) to avoid the heating due to Eddy currents. Therefore, a 22 cm long copper rod connects the sample holder to the mixing chamber.

- The sample holder is placed at the center of the main coil and the field gradient coils are placed on the calorimeter in order to ensure a maximum field gradient on the magnetic sample. The sample holder is made of a copper plate separated by three 5 cm long copper rods from the capacitive sensor made out of an isolating material. The upper plate is screwed into the rod, connected to the mixing chamber.

With the dimensions of the dilution refrigerator set, we calculated the required ^{3}He-^{4}He mixture to reach the desired temperatures. The calculated volumes of the main components are displayed in table 2.1. As I mentioned above, in the mixing chamber we have a sintered silver powder to ensure a better thermal heat exchange with the ^{3}He-^{4}He mixture. We extracted the volume of the sintered silver powder and we used this value for the volume of the mixing chamber. All these values and the volumes of the pumping pipes were used to calculate the theoretical volume of the ^{3}He-^{4}He mixture. 60 L of ^{3}He-^{4}He mixture is used during all the experiments with a 25% concentration of ^{3}He.

Component	1 K pot	Still	Mixing chamber	Impedance	Heat exchangers
Volume (cm^3)	4.8	30.5	25	0.16	22

TABLE 2.1: Volume of the dilution components.

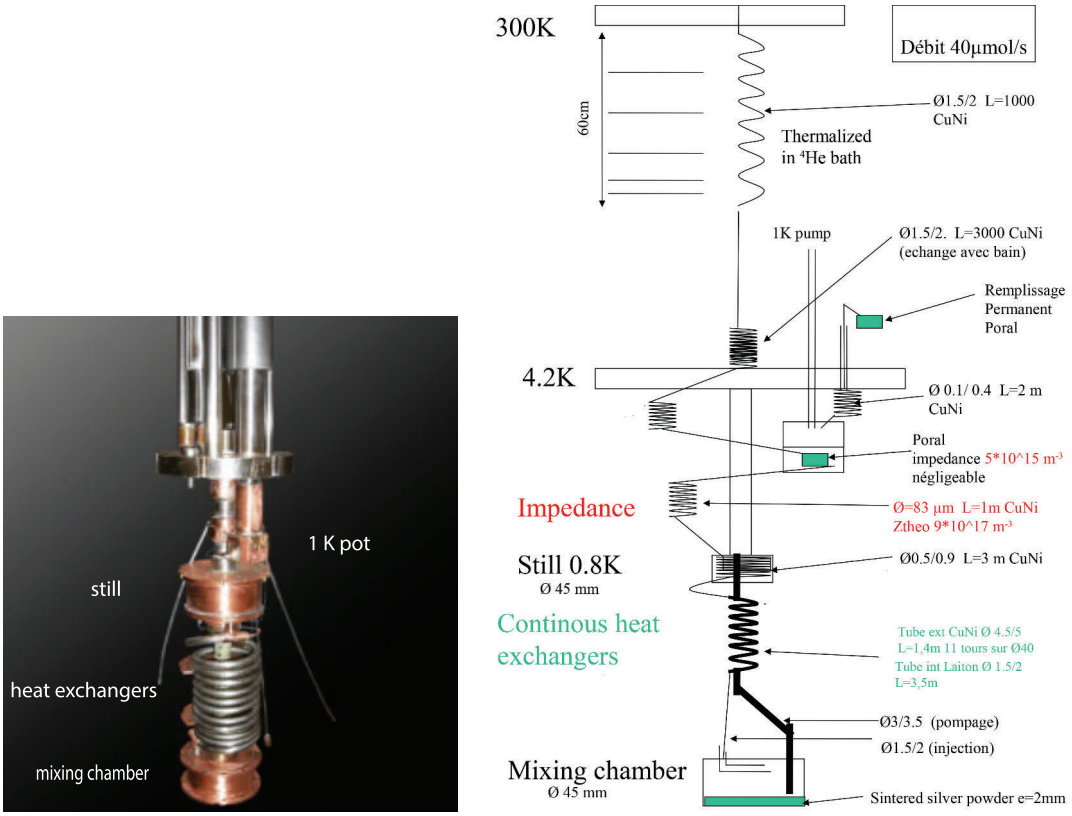

FIGURE 2.3: Lower part of our dilution fridge. Right: dimensions of the main components of the dilution refrigerator

2.3 Wiring

The goal of the device is not only to achieve very low temperatures, but to perform capacitive measurements under applied magnetic field. Therefore, wiring from 300 K down to the lowest temperature part of the dilution fridge is required. Wires are required for the different thermometers (1 K pot, still, mixing chamber, sample holder), for heating various components of the fridge or for the electronic detection.

When taking down wires from 300 K down to the lowest temperature, thermal energy is conducted by the wires and can be problematic for the good behavior of the dilution fridge. Therefore, a good analysis of the thermal properties of the chosen materials is required. The thermal energy conducted by the wires is expressed by the Fourier's heat conductance law

$$P_{wire} = \frac{S}{L} \int_{T_0}^{T} k(T) d(T) \tag{2.4}$$

where S is the surface, L is the length, k is the thermal conductivity of the wires and T is the temperature.

A second heating effect appears due to the Joule effect. When a current is injected through a wire, it will heat due to this effect. The heat energy from the Joule effect is expressed with the formula

$$P_{Joule} = RI^2 \tag{2.5}$$

where R is the resistance of the wires and I is the supplied electrical current.

In usual materials, a bad thermal conductivity is often associated with a large electric resistivity. It is thus necessary to make a compromise between these two heating effects, depending of the working conditions of the wires. In order to achieve very low temperatures and perform reliable measurements, different type of wires were selected.

As mentioned above, we need wires for four thermometers (1 K pot, still, mixing chamber and the sample holder). Because we use the four point method, four wires are required for each thermometer. They are supplied with a low current values (of the order of nA), and must not heat the thermometers: it is necessary to choose wires with a poor thermal conductivity, while the electrical resistivity is not so important.
For this reason, we choose phosphor-bronze wires which have a poor thermal conductivity. The conductivity of the material at 300 K and 4 K is 48 respectively 1.6 W/m/K. The wires have a diameter of 0.127 mm and roughly 1.5 m length. Using (2.4) and the tabulated values of $k(T)$ for 4 K and 300 K, the calculated heat energy conducted by one wire is ~ 66 μW.
Their electrical resistance is not so high (about 10 Ω/m). Therefore the heating from the Joule effect is almost negligible (below 5 pW).

To heat the different components (1K pot, still and mixing chamber), supplied currents of a few mA are required. Therefore, important heating effects are expected due to the Joule effect. It is thus necessary to choose wires with a low electrical resistivity. Copper wires were thus naturally chosen. A small diameter is better to minimize the heat by conduction effect. After a few tests, a diameter of 0.14 mm was chosen as such wires were proved to be robust enough for the manipulation in the dilution fridge. The electrical resistance of these wires are in the range of few

Ohms (3-5 Ω), thus the heating from the Joule effect is in the range of 3-5 μW for each wire. They have a large thermal conductivity (400 and 300 W/m/K at 300 and 4 K respectively). The calculated thermal energy conducted from 300 to 4 K by one wire is $\sim$ 1 mW.

Magnetization in our magnetometer is measured through a capacitive method. Capacitive measurements at very low temperatures are very sensitive to noise and parasite capacitors, therefore specialized wires (which have a low capacitance) are required. The design for our home made electronic detection (see chapter 5) requires the use of two wires from the low temperature amplifier to the room temperature amplifier stage. It is made in two stages. From 300 K to the 4 K flange, we used two semi-rigid Cu-Be coaxial wires. They are placed in the ^{4}He bath so it is correct to assume no thermal energy are conducted from 300 K down to the 4 K flange.
From the 300 K flange down to the sample holders, low capacitive flexible coaxial wires are used. Its core is made of an 0.1 mm diameter stainless steel, isolated with a teflon sheath from the stainless steel tress which shields the core of the cable. The electrical resistance is quite important (70 Ω/m), therefore a good thermalization is required.It is hard to exactly calculate the heat conducted by the low capacitance wires due to different material components. However, a calculation of the worst case (all wire made of stainless steel) was made and a value of $\sim$ 8 mW was found. In conclusion, a total energy of $\sim$ 30 mW is conducted from 300 to 4 K from both effects. All the wires are thermalized on the 4 K flange, therefore such low values are expected to be easily evacuated by our 83 mm stainless steel flange.
Between 4 K and the lowest temperature point, the sensors wires are thermalized in multiple points. The conductivity at very low temperature for phosphor bronze is 0.22 W/m/K. The calculated heat energy transfer to the environment in this region is $\sim$ 40 nW. The Cu-Be wires stops at the 4 K flange and the heat energy for the stainless steel wires in the 4 K to very low temperature is negligible (below nW values).
In conclusion, $\sim 1\mu$W values of energy is expected to be conducted by the wires to the mixing chamber. Such small value is acceptable for a dilution fridge of our dimensions.

2.4 Thermometry

2.4.1 General introduction

A thermometer is a device by which the temperature of an object can be measured through a change of one of its property, related to the temperature. There are various requirements for a thermometer to fulfill a quality measurement. First, a good knowledge on the physical law which relates the temperature to the object's property is required. It should operate over a wide temperature range and be insensitive to changes of the environment (magnetic field for example). The measured property should be defined by a simple law and must be quick and reproducible. An important property of the thermometer is that it must reach thermal equilibrium in a short time. The thermal contact between the sensor and the measured object should also be of good quality. Therefore, a thermometer should have a small heat capacity, a good thermal conductivity and a good thermal coupling with the object whose temperature is measured. In very low temperature measurements, this coupling is often optimized through the wires of the thermometer.

There are two types of thermometers (for more details, see for example reference [5]): primary and secondary. In *primary sensors*, the property of the object related to the temperature is well known, therefore it provides a reliable result without any calibration. Examples of primary thermometers are gas sensors (in which the temperature of the object is related to the pressure and volume of the gases through the ideal gas relation), noise thermometers (in which the thermal noise of an electrical resistor is measured) or acoustic gas thermometers (in which the velocity of sound in a gas is measured). For the *secondary thermometers*, the theory is not enough to provide directly the temperature of the object. Usually they are more sensitive than primary ones, but they require a calibration (usually with primary thermometers). In this category we can find resistive (in which the electrical resistance is related to the temperature), capacitive (suitable in applied magnetic field environments) or magnetic thermometers (based on the T^{-1} dependence of the magnetization of a paramagnet).

For our refrigerator dilution, we are using three types of resistive thermometers. The reason behind is:

- they are sensitive at very low temperature
- they have a compact design, thus easily manipulated in the requirements of dilution refrigerators
- they are easy to measure and implement
- they have a low cost

The technique used for measuring the resistance of such thermometers at low temperature is the four wires method. This method uses two separate pairs of current-carrying and voltage-sensing electrodes to make an accurate measurement (see figure 2.4). Indeed, it allows to measure the thermometer resistance without the contribution of the wires.

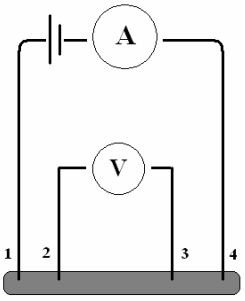

FIGURE 2.4: Schematic view of the 4 wires resistance method used for our thermometers. The current is injected through the terminal 1 and 4 and its resistance is measured through terminal 2 and 3.

2.4.2 Our thermometers

Our experiment requires four thermometers:

- for the 1 K pot
- for the still
- for the mixing chamber
- for the sample holder

Three types of thermometers were chosen depending on the temperature range for which they are used.

For the 1 K pot a Cernox sensor has been chosen. The excellent stability of the

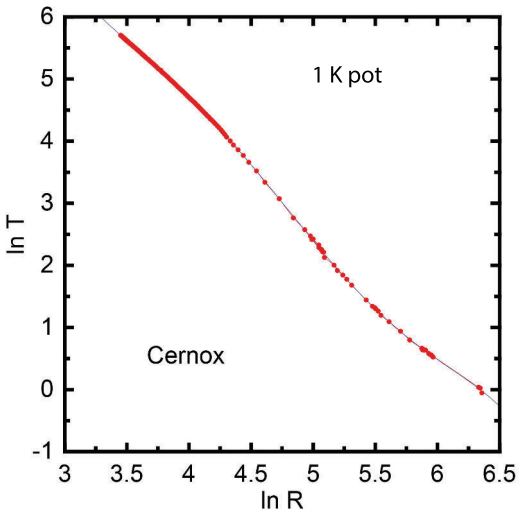

FIGURE 2.5: Temperature dependence of the resistance for the Cernox Cx 63518 thermometer. Fit parameters are displayed in table 2.2

Cernox sensor, Cx 63518 Lake Shore, at temperatures between 100 mK and 400 K makes it a good candidate for the 1 K pot. It has a high sensitivity at low temperatures and good sensitivity for the high temperature regime. The thermometer was calibrated before my arrival. The temperature dependence is shown in figure 2.5. A Cryogenic Control System (Cryocon) is used to read the temperature of the 1 K pot.

For the still we are using a ruthenium oxide (RuO_2) sensor, Rx 15, one of the only two resistive thermometers able to measure below 100 mK. The sensor was calibrated at the laboratory before my arrival. The temperature dependence of the thermometer is presented in figure 2.6 and the fit parameters are displayed in table 2.2.

For the mixing chamber we are using a Lake Shore germanium sensor, Ge 30588. Germanium sensors have the highest sensitivity due to their large resistance variation with temperature ($\backsim$ 20 Ω at 4 K and $\backsim$ 250 kΩ at 50 mK). They provide a great stability in time, and can thus be used as reference thermometers. However, below 50 mK, their resistance tends to saturate so that their sensitivity strongly decreases. In addition, because of their high magnetoresistance they are not appropriate for high magnetic fields environments. The Germanium sensor was calibrated by the Lake Shore company down to 50 mK. We extrapolated the

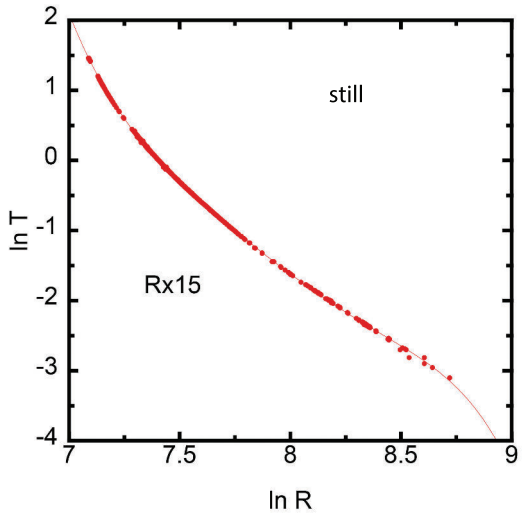

FIGURE 2.6: Temperature dependence of the resistance for the RuO_2 Rx15 thermometer. Fit parameters are displayed in table 2.2

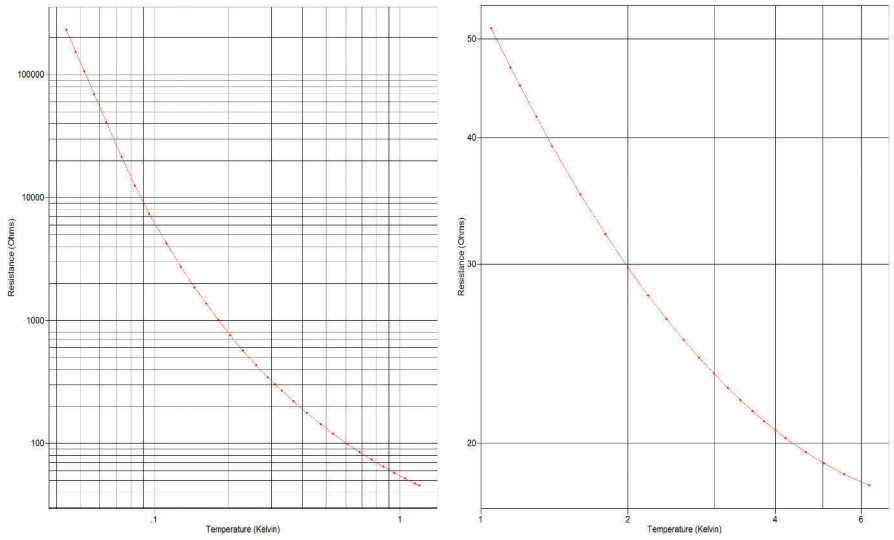

FIGURE 2.7: Temperature dependence of the resistance for the Ge 30588, data results by LakeShore. Fit parameters are displayed in table 2.2

fit below 50 mK to obtain the minimal temperatures in our dilution fridge. The temperature dependence of the resistance for the Ge resistor is displayed in figure 2.7 and the fit parameters are displayed in table 2.2.

For the sample holder we are using a second RuO_2 sensor. I have performed the calibration for the second RuO_2 sensor (see figure 2.8). For the calibration, we wrapped the RuO_2 sensor in a copper shell and placed it close to the germanium sensor on the mixing chamber. We performed multiple thermal cycles and we fitted the data using the germanium temperature values. Later, the RuO_2 sensor

was moved to the sample holder at approximately 5 cm from the sample. It is less sensitive than germanium sensors but its advantage is a low magnetoresistance which makes it a strong candidate for high magnetic fields measurements below 1 K (at 2 K for an applied magnetic field of 8 T, the $\Delta T/T$ errors are 7.9 for RuO_2 compared to 60 for Ge sensors).

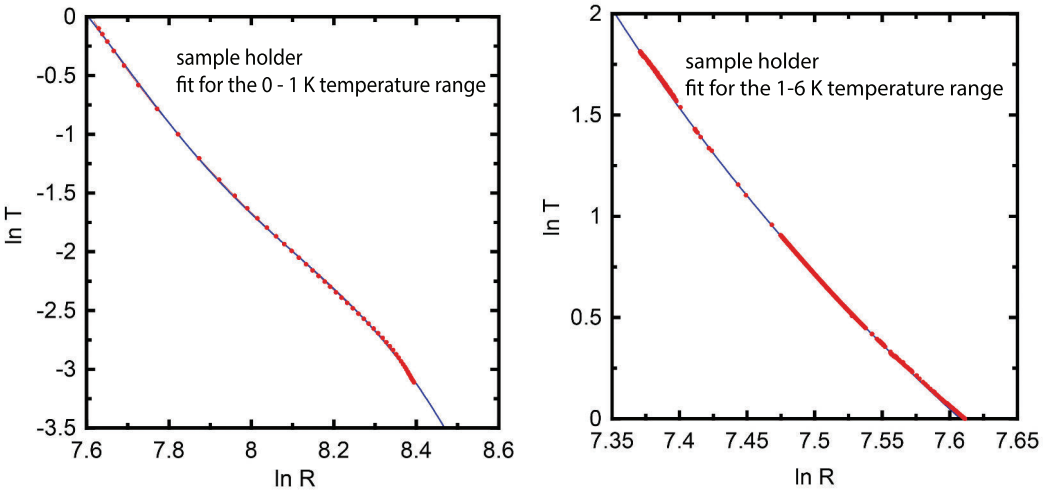

FIGURE 2.8: Temperature dependence of the resistance for RuO_2. Fit parameters are displayed in table 2.2

For all thermometers, a polynomial function ($ln(T) = M_0 + M_1 ln(R) + M_2 (ln(R))^2 + M_3 (ln(R))^3 + M_4 (ln(R))^4 + M_5 (ln(R))^5 + M_6 (ln(R))^6 + M_7 (ln(R))^7 + M_8 (ln(R))^8$) is used for the calibration of the data. The fit parameters are displayed in table 2.2.

	Cernox	Ge (0-1K)	Ge (1-6K)	RuO_2 (0-1K)	RuO_2 (1-6K)	Rx15
M_0	-81.739	30.719	656.6795	-487.050	1040.757	-0.023
M_1	179.959	-28.758	1068.829	95.230	-176.011	253.77
M_2	-138.941	12.487	-2389.963	0.871	-5.038	453453.101
M_3	55.169	-3.222	1413.458	0.916	0.437	-166867660
M_4	-12.381	0.522	-270.909	-0.11	0.085	3.2 e+10
M_5	1.575	-0.053	-48.318	-0.043	-0.012	-2.384e+12
M_6	-0.105	0.003	30.626	-0.0007	0.006	
M_7	0.002	-0.0001	-5.071	0.00085	-0.00044	
M_8		1.914 e-06	0.294	-1.9e-06	-7.44e-06	

TABLE 2.2: Fit parameters for our thermometers.

As mentioned above, it is important that the sensor and the measured object can achieve thermal equilibrium in a short time. For this reason, Apiezon N grease is used to ensure a good thermal contact between the sensors and the measured objects. In addition, when a current is supplied to the thermometer, it will heat due to the Joule effect, so that a careful thermalization of the wires is needed.

A home made three channel resistance measuring module (MMR3/MGC3 developed at Néel Institute) allows us to control and regulate the temperature of still, mixing chamber and sample holder. Data acquisition is performed through GPIB protocol using a custom made Labview software, that I have developed. After several thermal cycles, we observed that the home made three channel resistance measuring module, used for controlling and reading the thermometers, is heating the environment, thus creating false readings. A filter was installed before the resistance module to correct the anomaly. No further problems were encountered.

2.5 Dilution fridge characterization

2.5.1 Optimization of the base temperature

The first tests performed with the dilution refrigerator were using only ^{4}He gas in order to test the possible leaks. We operate the circulation of ^{4}He in the same conditions as will be used for the ^{4}He-^{3}He mixture (see section 2.1). ^{4}He is injected in the dilution fridge and a ^{4}He vapor gas is created by pumping on the still. The gas is condensed by the 1 K pot cooling stage creating superfluid ^{4}He in the closed circuit.
The existence of superfluid leaks which are otherwise undetectable can be tested with this protocol. Unfortunately, our first tests confirmed the existence of such leaks. By isolating different components of the dilution fridge and starting again the ^{4}He circulation, we were able to find the superfluid leak in the mixing chamber. However, this was a long process which caused delays in our schedule and forced us to replace the mixing chamber.
With the new chamber in place, we connected again the wires on the dilution fridge and tested it again with ^{4}He gas. A temperature of 0.9 K which remained stable over night is consistent with no superfluid leaks which allowed us to proceed with the next step: the ^{3}He-^{4}He mixture tests.

At that point we had no possibility in the lab to measure the exact composition of the mixture. We started with 60 L ^{3}He-^{4}He mixture for which the proportion of ^{3}He was unknown and estimated to be between 20 to 40% (ideally is around 25%).

The method to optimize the quantity of mixture we need to inject in the system is the following. We condense gradually the mixture to the point where the temperature of the still starts to drop. By the design of our dilution refrigerator, at this point we know that there is liquid mixture in both mixing chamber and still. We further condense the mixture and at the same time we start pumping on the still, creating the closed circulation of ^{3}He. At this point, the temperature of the mixing chamber and still should decrease to $\sim$ 500-600 mK. To increase the flow of ^{3}He in the circuit, therefore cooling further the system, we heat the still to temperatures between 750 and 900 mK. Different temperatures of the still are tested to determine the optimal conditions for the dilution refrigerator. We further condense little by little, with enough time between steps to reach thermal equilibrium, up to when the minimum temperature on the mixing chamber is achieved.

The minimal temperature achieved when performing the first test was 0.045 K with a still temperature of 0.8 K. Although a promising start, the injection pressure was quite high ($\sim$ 700 mbar compared to expected values below 500 mbar) and the aspiration pressure quite low (0.05 mbar). We concluded that our flow impedance was too important for our system (limits the ^{3}He flow); we changed its length from 1.4 to roughly 0.9 meter. The new impedance gave us an acceptable injection and aspiration pressures, 500 and 0.14 mbar respectively, for a 0.8 K still temperature. The minimal temperature achieved is in this case, 0.049 K. Table 2.3 shows the injection, aspiration and the flow for the two impedance values to better illustrate the behavior of our dilution fridge.

$L_{Impedance}$ (m)	flow (cm^3/min)	P_{inj} (mbar)	P_{asp} (mbar)
1.4	1.6	700	0.05
0.9	1.1	500	0.14

TABLE 2.3: Working parameters depending on the impedance length

By performing several cooling down tests, we observed that the base temperature of the still was too low ($\sim$ 0.45 K). First thought was that it was due to a high concentration of ^{3}He in our mixture, thus a higher concentration of ^{3}He in the

still. If we add ^{4}He in the mixture, we could expect better performances and a lower base temperature. Therefore, we added more ^{4}He in the mixture ($\sim$ 50 mbar) which raised the still base temperature from 0.45 to 0.6 K, but it did not improved the base temperature of the mixing chamber.

Although we did not reach the minimum expected temperature, we found good working conditions with 36 l of ^{3}He-^{4}He mixture, a 500 mbar injection pressure, a 0.14 mbar aspiration pressure and a 0.8 K still. We thus decided to perform cooling power tests in the actual mixture configuration.

During these tests, we encountered problems with the 1 K pot. In order to maintain a 1.2 K, we pump on a small ^{4}He bath which is the 1 K pot. A small impedance connects the 1 K pot to the ^{4}He cryostat to ensure a constant flow of ^{4}He in the 1 K pot. After several thermal cycles, the impedance blocked. A poral system was built at the entrance of the 1K pot aspiration tube in order to prevent possible impurities from entering and blocking the impedance.

2.5.2 Cooling Power

The protocol for characterizing the base temperature and the cooling power of the dilution is the following:

- condense the mixture and wait for the stabilization of the system
- heat the still at the desired value $\rightarrow$ increase the ^{3}He flow in the closed circuit $\rightarrow$ cool down and achieve the minimal temperature of your system
- heat the mixing chamber with different applied power values and wait the system to stabilize
- plot the applied power as a function of temperature
- check for the expected T^2 dependence behavior of the cooling power (equation 2.3)
- find the optimal base temperature - cooling power - loss for the dilution fridge

Applied power	$T_{mixing\ chamber}$		
	T_{still}	T_{still}	T_{still}
(μW)	650 mK	800 mK	850 mK
0	43.8	41.6	47
1	49.5	43.1	
5	67.9	53.2	62
10	84.9	72.8	76.5
16	103.2	90	89
20	115	113	99.8

TABLE 2.4: Cooling power of our refrigerator dilution.

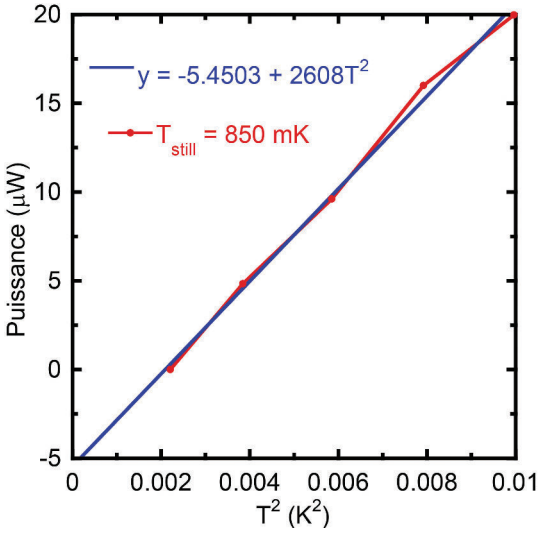

FIGURE 2.9: Cooling power of the dilution as a function of square temperature

Table 2.4 shows the values for several still temperatures and the optimal conditions for our dilution refrigerator are plotted in figure 2.9.

We recover the expected T^2 dependence behavior of the cooling power for all still temperatures.
The best performance is obtained for a 0.85 K still temperature. In these conditions, the dilution fridge provided a 20 μW cooling power at 0.1 K which is normal for a dilution fridge of our dimensions. The intrinsic losses is around 5.5 μW, a larger value than expected. A reason for these values can be the presence of mechanical vibration in the lower part of the dilution refrigerator or it can come from a malfunction of a part of the fridge.

From these parameters: volume of the dilution, minimal temperature, the injection and extraction pressures we can estimate the ^{3}He/^{4}He ratio using a home made

software (developed by S. Triqueneaux - Institut Néel). The proportion of ^{3}He we obtain in the final mixture is $\backsim$ 25%.

2.5.3 Implementation of the sample holder

At this point, we had found optimal working conditions with the dilution refrigerator: they are a minimum temperature $T_{min} = 47$ mK with a cooling power of 20 μW at 0.1 K for a still temperature of 0.85 K. 36 l gas ^{3}He-^{4}He mixture was injected with a pressure of 500 mbar and the extraction pressure is $\sim$ 0.11 mbar.

I thus started focusing on the design and development of the sample holders and the electronic detection described in Chapter 4.
The next step was to test the dilution fridge when connecting the sample holder. Unfortunately, we encountered stability problems when I connected the sample holder to the mixing chamber and I started to perform several thermal cycles. We first recovered base temperatures in the 0.05 K range, but when we performed a second thermal cycle, we were not able to recover temperatures below 0.1 K. In addition, the base temperature was not stable in time anymore. In the same time we observed a coupling between the 1 K pot and the still temperature, the values of the first strongly affecting the second one.

We first thought that the problems encountered were due to the presence of the sample holder. By removing the sample holder the problems remained, with the conditions of the dilution refrigerator deteriorating daily. Figure 2.10 displays the odd behavior encountered when we performed cooling power tests after we took out the sample holder. The times to reach equilibrium are very long and sometimes we can observe a heating effect before cooling down.

Using the same ^{3}He-^{4}He mixture, having in general the same conditions, we started to think at the possible problems that could have occurred in the time we did not use our dilution fridge.
We first checked that there were not thermal short circuit, i.e. warm wires or capillary tubes which would have been in contact we cold ones. But it did not solve the problem.
We thus thought that there could be a problem with the flow of ^{3}He in the system. Not having a regular flow can heavily affect the base temperature of the mixing chamber. We tested the debit flow of our dilution to check the stability of the

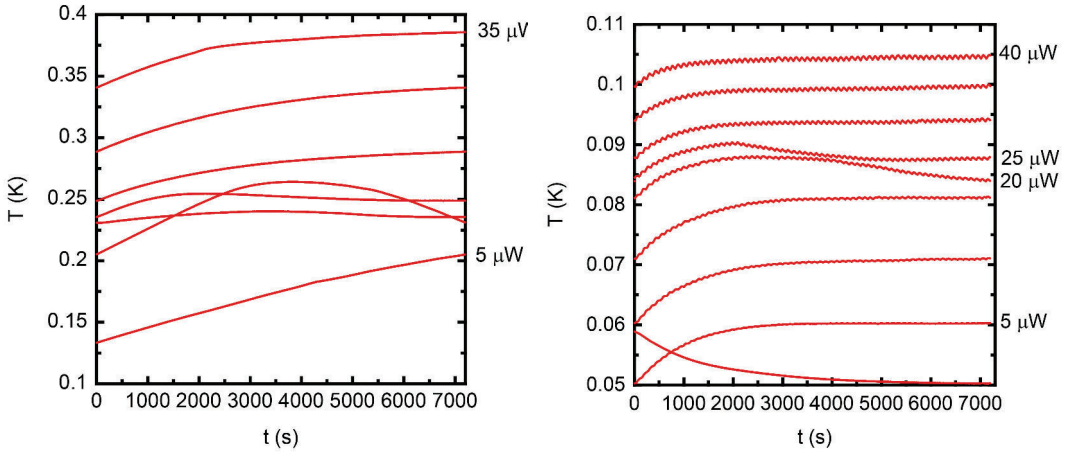

FIGURE 2.10: Encountered problems when performing cooling power tests. The two tests are made in two conseccutive days.

system from this point of view. It was tested with two different methods. The first one is a home made experiment; the protocol is described below and schematically displayed in figure 2.11. We applied a 2 bar pressure of ^{4}He gas on the injection

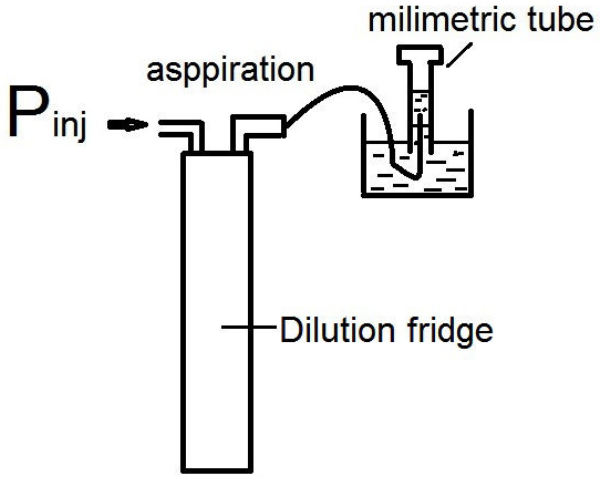

FIGURE 2.11: Home made experiment to detect the ^{4}He flow in our dilution refrigerator

of the dilution fridge. We connected the extraction to a flexible tube which we immersed in a millimeter tube filled with alcohol. We noted the initial level value of the alcohol. Using a clock to measure the time, we noted at different moments the alcohol level removed from the millimeter tube by the ^{4}He gas. We repeated several times this protocol at 4 K and room temperature and we found a steady ^{4}He flow in both cases ($\sim$ 1.6 cm^3/min at 300 K). Later on, we performed another

test with a mass spectrometer which gave a consistent results. These values are consistent with what is expected from the calculation with the dimensions of the dilution refrigerator (impedances, capillary, tubes, etc...).

Because it was not a problem of the global steady flow, we tested separately different parts of the dilution refrigerator. We disconnected the dilution refrigerator at several points: before the first flow impedance (see figure 2.3 left), before and after the mixing chamber. The results were consistent with what is expected for a normal behavior. By reconnecting the dilution refrigerator, the problems mentioned above were unfortunately still present.

Another possible problem could have been the creation of a superfluid ^{4}He film in the still which would expand to the impedance after the still. In that case, heating the still would release ^{4}He in the circuit which deteriorates the performances of the dilution. A resistance was placed on the tube leaving the still, just above it. The aim was to prevent the apparition of the superfluid film, but no change was seen with or without heating it.

There could also exist a leak between the heat exchanger (it is made of a small capillary tube - injection - which passes through a larger one - extraction). In that case, a part of the ^{3}He would flow through the heat exchanger, by-passing the mixing chamber. In this situation, the final flow could be the same, but the behavior of the mixing chamber is affected. For this reason we separated the heat exchangers from the dilution refrigerator and tested it. No leak was found.

We thus performed all the possible tests for this anomalous behavior, and had not found its origin. All the parts of the dilution fridge behaved normally when tested separately. We thus considered other reasons. As I mentioned before, the connection between the still and mixing chamber is made via a fiberglass rod screwed at both extremities which has possibly deteriorated. If not well fixed, this design can induce vibrations which disturb the He flow and heats the low temperature part of the fridge. Unfortunately we had no possibility to improve it.

Losing a lot of time already, and reaching no clear response of the reason behind these anomalies, we decided to change the lower part of the refrigerator dilution. We took advantage of this change and we redesigned the connection between the still and the mixing chamber to be more robust. Three carbon glass rods provide now a better stability which we hope to resolve our problems with the cryogenic part.

Les bobines de champ magnétique

Dans ce chapitre, je présente les propriétés des bobines de champ magnétique qui ont été utilisées pour générer le champ magnétique dans notre magnétomètre: une bobine supraconductrice 14-16 T, et des bobines de gradient de champ en cuivre.

Je détaille d'abord les caractéristiques de notre bobine supraconductrice, commerciale, faite de NbTi et de Nb_3Sn: elle permet d'atteindre 14 T à 4.2 K, 16 T à 2 K, grâce à un système de pompage sur le bain. Elle possède un diamètre intérieur de 53 mm. Un mode persistent est disponible, et l'homogénéité du champ magnétique est de l'ordre de 10^{-2} sur une hauteur de quelques centimètres.

Je précise ensuite la conception et les dimensions des bobines de gradient de champ que nous avons développées au laboratoire: deux bobines enroulées dans deux directions opposées, avec un fil de cuivre de 0.16 mm, sur un diamètre intérieur de 42 mm permettant de les fixer au calorimètre de la dilution. Le gradient de champ obtenu avec ces bobines est de 3.7 $T.m^{-1}.A^{-1}$.

Chapter 3

Magnetic Coils

Various magnetic coils are available at the moment, which can provide magnetic fields from few mili tesla up to 90 T using non-destructive magnets or up to hundreds of tesla using single-shot magnets. Our set up requires a high stability and low temperatures which imposes the use of a superconducting coil.

3.1 Main coil

We use a commercial 14 16 T superconducting coil with a 53 mm internal diameter. It is made out of two coils connected in series. The inner coil is made out of Nb_3Sn, while the outer coil is made of NbTi. It is designed to produce magnetic fields up to 14 T at 4 K, and 16 T at 2 K in a persistent mode. We can perform measurements in a persistent mode which guarantees a lower ^{4}He consume as well as a better stability of the field as a function of time.
The persistent mode shunt is made of a superconducting wire which is connected to the two terminals of the coil windings. When the shunt is heated above its transition temperature, it is highly resistive and acts as an open switch: current can enter in the coil through the current supply line (see figure 3.1). When it is superconductive, in the "closed" "x" regime, the current circulates in the superconducting coil without loss of energy, thus no further supplied current is needed. The protocol for the persistent mode is

- heat the shunt above the transition temperature → open regime

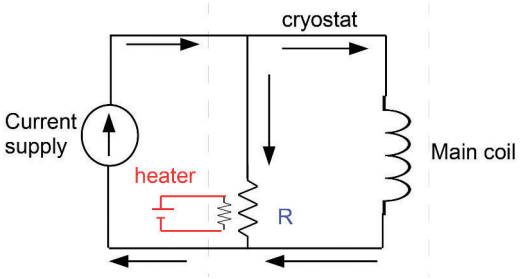

FIGURE 3.1: Schematic view of the shunt required for persistent mode of the main coil.

- ramp up the supplied current until the desired magnetic field is obtained
- cool down the shunt → closed regime
- ramp down the supplied current

The current is supplied by a commercial +/ 10 V Bouhnik power supply which has two current ranges: +/ 12 A and +/ 120 A. It is equipped with a flux gate system (a technology developed by the electronic department of Néel Institute) to guarantee a high stability over time (10 ^{5}I, with noise in the range of +/ 2·10 ^{6}I) even in non persistent mode. The power supply is controlled via a computer through an IEEE/RS232 interface, connected to a data acquisition board (DAQ NI PCI6221). A home made software that I developed controls the power supply and recovers the datas.

A calibration of the superconducting coil has been performed with the help of a hall probe. Figure 3.2 left displays the good agreement between the data provided by the manufacturer (solid blue line) and the results with the hall probe (red circle dots). The homogeneity of the magnetic field profile was measured and is shown in figure 3.2 right. We observe an homogeneity better than 10 ^{2} T of the magnetic field over a distance of $\sim$ 3 cm from the middle of the coil, which is compatible with our requirements since the capacitive sensor is a few mm height and we use small (few mm) magnetic samples.

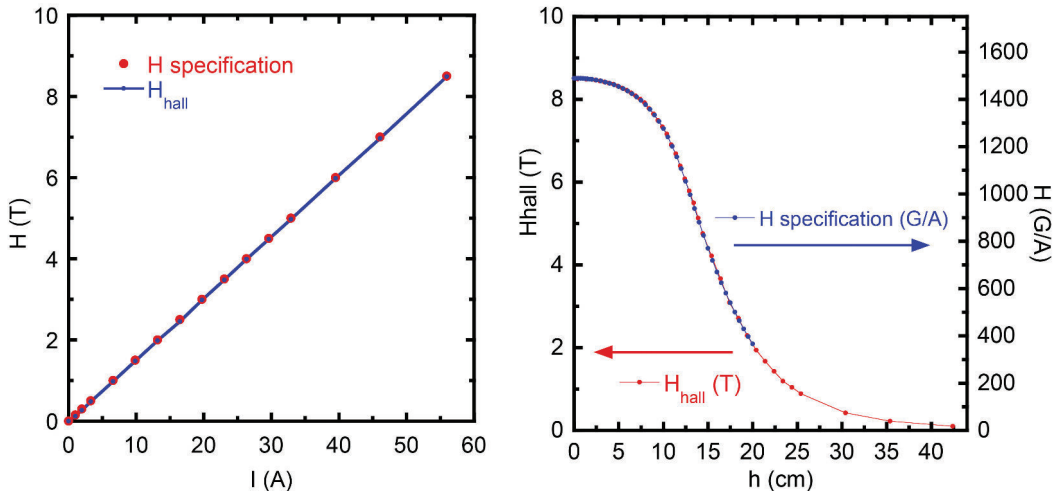

FIGURE 3.2: 16 T superconducting coil. Left: data provided by the manufacture (solid blue line) and verification with a hall probe (red circle dots). Right: magnetic field profile as a function of distance (0 cm = the middle of the coil).

3.2 Field gradient coils

In addition to the DC magnetic field, a field gradient is required for our measurements. A field gradient can be achieved in two ways: either by using a permanent magnet at a fixed distance from the sample, or by using magnetic coils. We have chosen to use field gradient coils to be able to control the field gradient (both amplitude and sign) depending on our experiments.

The design of the main coil implies the pumping on the ^{4}He bath below the magnetic coil to obtain magnetic fields up to 16 T (it uses the principle of a "Claudet" bath). For this reason, the field gradient coils have to be placed inside the main coil, between the coil and the calorimeter. So, because we perform magnetization measurements up to 16 T, we are forced to use resistive field gradient coils, since NbTi coils could not work in these conditions.

Our gradient coils are made of two magnetic coils wound in opposite directions, built by the cryogenic service of the laboratory (G. Barthélémy). Our first gradient coils were wound on a 42 mm diameter fiberglass tube. In addtition, we took advantage of the possibility to wind coils in our laboratory, to build a second set of gradient coils with a new material, the stratified composite material "Dellit Pertinax", and check whether it is suitable for such coil applications.

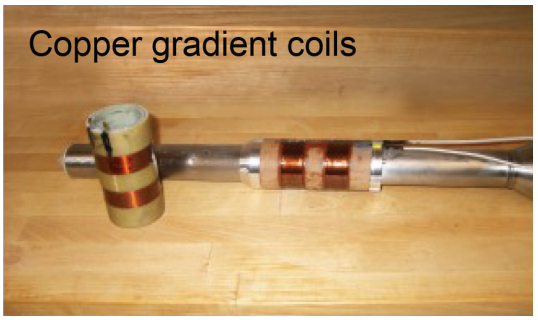

FIGURE 3.3: Gradient field coils (developed by G. Barthélémy at Néel Institute).

In order to avoid large ^{4}He consumption, we opted for small copper coils. Preliminary calculations were performed to determine the optimal design of the gradient coils. Given the constraint on the internal and external diameters (fixed by the main coil and the calorimeter), the parameters are: the wire diameter, the number of layers and turns, and the separation between the coils, in order to obtain the lowest dissipated power for a field gradient of 1 T/m.

For the calculations, we assumed a copper resistivity of 1.7 10 ^{6} Ω.cm at 300 K, and a resisdual resistivity ratio $RRR = \rho_{300\mathrm{K}}/\rho_{0K} \sim 100$. The total resistance at low temperatures, R_{tot}, the required supplied current, I, and the dissipated power are

$$\begin{cases} R_{tot}(\Omega) = 1.7 \cdot 10^{-10} \dfrac{L(m)}{\pi r^2_{wire}(m)} \\ \text{for a field gradient of 1 T/m,} \quad I(A) = \dfrac{100}{\dfrac{\partial H}{\partial z}\ (G/A/cm)} \\ P(W) = R_{tot} I^2 \end{cases} \tag{3.1}$$

where L and r are the length and the radius of the copper wire. The values for several wire diameters and distances between the two coils, are presented in Table 3.1.

A 0.16 diameter copper wire was chosen for the two coils (small enough to make a large enough number of layers, together with a large enough robustness, necessary for the winding). The centers of each coil are separated of 3.8 cm from each other, which was, given the coil width, the smallest distance possible to have enough space between the coils. Each coil was wound with 22 layers for the fiberglass tube and 23 layers for the "Dellit Pertinax" one. A kapton was glued over the wires to protect the coils and avoid deterioration of the coils in time. The external diameter is 50.1 mm for the fiberglass coil and 51.2 mm for the "Dellit Pertinax"

Φ wire (mm)	distance (cm)	Φ int (cm)	N spires/layer	N layers	grad H (G/A/m)	L wire km	R_{tot} (Ω)	I (A)	P (W)
0.1	3	2.1	100	35	647	1.01	21.98	0.15	0.52
0.1	3.8	2.1	150	30	714	1.28	27.89	0.14	0.54
0.16	3	2	105	23	431	0.69	5.82	0.23	0.31
0.16	3	2	100	28	511	0.79	6.73	0.19	0.25
0.16	3.8	2.1	105	23	374	.70	5.95	0.27	0.42
0.16	3.8	2.1	100	23	357	.67	5.65	0.28	0.44

TABLE 3.1: Several theoretical values for the field gradient coils for a field gradient of 1 T/m.

one.

Figure 3.4 shows the magnetic field profile of the two field gradient coils. It was

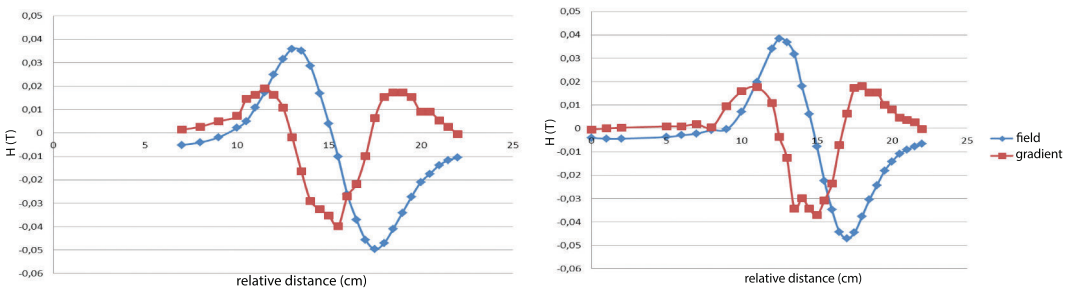

FIGURE 3.4: Magnetic field profile of the field gradient coils: left - fiberglass support, right - "Dellit pertinax" support

performed at the institute with the help of Aiteb Naimi (during her internship). The maximum field gradient was obtained in both cases at a value of 3.7 T/m/A, which is consistent with the result obtained from calculations. We opted for the fiberglass support coil as it has a more suitable field gradient shape. Nevertheless, these tests, together with several thermal cyclings approve the use of the "Dellit Pertinax" material as a valuable material for cyrogenic applications.

A specific current supply for the field gradient coils, was built at the laboratory to provide a continous current with a great stability over time within the +/ 1 A range.

Capteurs capacitifs

Dans ce chapitre, je présente les capteurs que nous avons conçus et réalisés afin de mesurer de façon capacitive le déplacement induit par la force de Faraday dans notre magnétomètre.

Le choix a été fait d'utiliser un système micro électromécanique (MEMS) nanofabriqué afin de diminuer le plus possible la distance initiale entre électrodes, et ainsi augmenter la sensibilité. Le design de ce MEMS est basé sur de précédentes réalisations au laboratoire. Il est constitué d'une membrane en silicium, suspendue par des ressorts en silicium eux-aussi, au-dessus d'une électrode en or. Le silicium utilisé est très dopé, afin d'avoir des propriétés conductrices à très basse température, et jouer le rôle ds'électrode. Je précise les conditions de fonctionnement d'un tel MEMS, et en particulier la sensibilité que l'on peut attendre.

Après avoir testé la faisabilité de l'utilisation de ce type de dispositif à très basse température, nous avons adapté la géométrie du capteur afin d'avoir la sensibilité requise dans notre expérience, à savoir une variation de capacité $\Delta C/C = 10^{-6}$ pour une variation d'aimantation de 10^{-8} A.m^2 tout en gardant une membrane suffisamment robuste, et en limitant les effets de couple. Cela implique notamment des ressorts plus larges et moins espacés, et une épaisseur de membrane d'environ 60 μm.

Cependant, après ces étapes de conception, le procédé d'élaboration (auquel je n'ai pas directement participé) a échoué, à cause des problèmes de changements des matériaux nécessaires à la nanofabrication. Pendant qu'un autre process était à l'étude, j'ai donc développé un nouveau capteur en m'inspirant du travail de Slobinsky et al. au Royaume-Uni. Ce capteur, fabriqué grâce à un processus d'imprimante 3D, est composé de deux parties en plastique: l'une sur laquelle sera posée l'échantillon est la partie mobile. Elle est suspendue à un support extérieur par des fils en nylon. L'autre, fixe pendant la mesure, est vissée dans ce

support extérieur de façon à ajuster la capacité initiale au cours de la mesure. Les deux surfaces en regard sont recouvertes de laque d'argent pour créer des surfaces conductrices. Ce capteur de test s'est avéré prometteur pour faire des mesures moins sensibles, ou avec des plus gros échantillons que le MEMS décrit plus haut.

Chapter 4

Capacitive Sensors

In section 1.2 I presented the principle of the Faraday force magnetometer (see figure 4.1). The magnetization, M, is obtained by measuring the Faraday force, $\vec{F} = \vec{M} \cdot \nabla \vec{B}$, exercised on a magnetic sample placed in a magnetic field gradient. To measure the Faraday force, we use a capacitive detection method which is especially suited for measurements in our extreme conditions: very low temperature and high magnetic field. Before I present the geometry of our two sample holders, I quickly remind the important ingredients required in such a design.

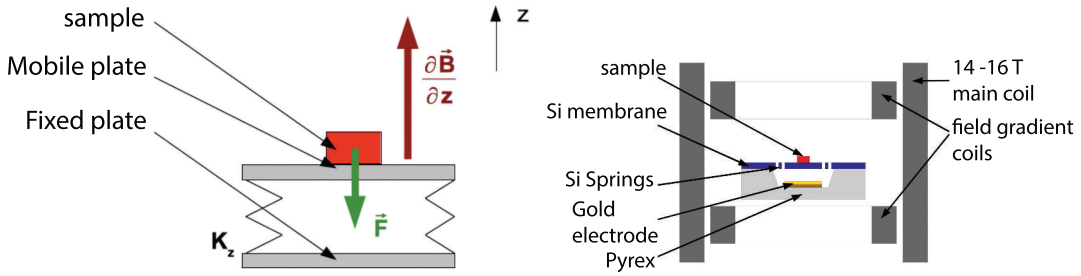

FIGURE 4.1: Left: Principle of the magnetization measurements in a Faraday force magnetometer with a capacitive detection. Right: nanofabricated MEMS capacitive sensor.

The capacitive sensor is made of two parallel metallic plates, the two electrodes of a capacitor. The magnetic sample is placed on a movable plate, supported by springs above a fixed plate. In such design, the applied field on the direction z creates a Faraday force, F_z, which creates a displacement, Δd, of the movable plate, until it is balanced by the restoring force of the springs.

$$F_z = M_z \cdot \frac{\partial B}{\partial z} = K_z \Delta d$$

The displacement of the movable plate can be detected as a change in capacitance, so that

$$\frac{\Delta C}{C_0} = \frac{\Delta d}{d_0} \tag{4.1}$$

From the two equations, the main components of the capacitive sensor can be extracted. Therefore, we need:

- two metallic surfaces to create the capacitor
- one movable plate supported by springs above a fixed plate
- the spring stiffness K_z has to be small along the z direction, to have a sizeable displacement in presence of small forces
- another important aspect when measuring anisotropic magnetic samples is the existence of torque effects. In order to prevent changes of the capacitance due to this effect, the stiffness of the springs in the x and y directions have to be much larger than in the z direction ($K_z/K_{xy} << 1$)

With our magnetometer, we aim to measure magnetization with a sensitivity of at least 10^{-8} A.m^2 (10^{-5} emu). From the above equations, we can observe that the sensitivity of the measurement can be increased in two ways: either by changing the field gradient or by reducing the initial distance between the two electrodes of the capacitor. For this reason, we decided to built a nanofabricated capacitive sensor with a gap as small as possible (see figure 4.1 right).

4.1 Microelectromechanical system: design

For the nanofabricated capacitive sensor, we started from a microelectromechanical system (MEMS), already existent in the laboratory (see figure 4.2). It was developed and built at the Néel Institute (formerly CRTBT) by the group of F. Ayela to measure the thermal conductivity of materials at the nanoscale level. Below, I will briefly present the MEMS, but an extended study about the technology process on how to fabricate such devices can be found in the thesis of E. Lennon [6].

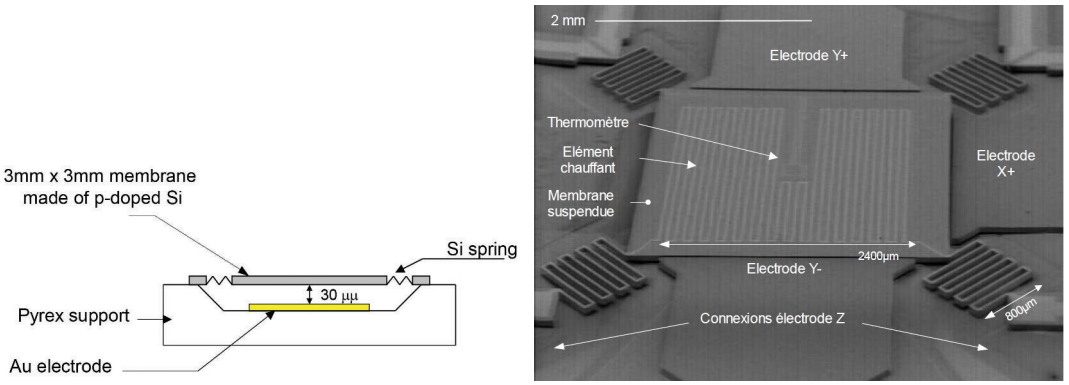

FIGURE 4.2: Nanofabricated MEMS: F. Ayela's design. (from reference [6])

A schematic design of the MEMS can be seen in figure 4.1 right. The main components are:

- A 25 x 30 mm Pyrex support
- A 2.4 mm square gold electrode deposited on the Pyrex support.
- Faced to the gold electrode, a 3 mm square membrane is suspended by four silicon springs to the Pyrex support. The membrane is made out of doped silicon in order to be conductive
- A gap between the electrodes of 30 μm with an associated capacitance of $\sim 2\ 10^{-12}$ F.

The silicon membrane was designed to perform measurements in the x and y directions as well as in the z direction. Below we show how the spring stiffness can be estimated.

4.1.1 Spring stiffness: horizontal case

Figure 4.3 left shows the schematic view of the deviation expected from the springs in the horizontal case. Because of their design, the elongation is much smaller than the dimension of the springs. In this case, the elongation of the spring can be seen as the elongation of n springs of length, l_t, and the transversal deflection as for a beam of equivalent length, l_0.

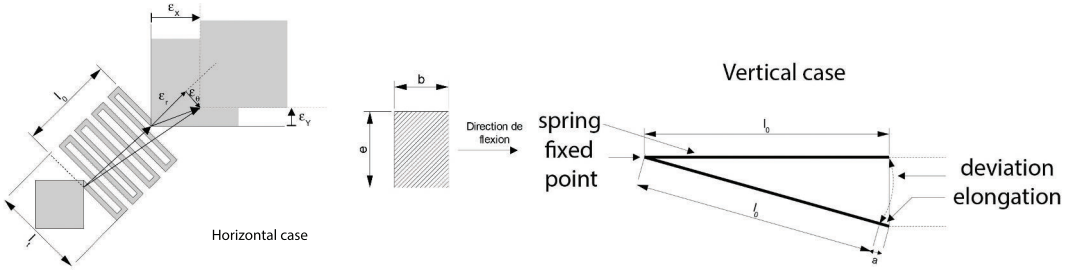

FIGURE 4.3: Schematic view of the horizontal (left) and vertical (right) deviation of the springs.

The force, F_r, induced by the elongation, ϵ_r, on each equivalent spring is

$$F_r = \frac{3EI\epsilon_r}{nl_t^3} \tag{4.2}$$

The force, F_ϑ, induced by the transversal deflection, ϵ_ϑ is

$$F_\vartheta = \frac{3EI\epsilon_\vartheta}{l_0^3} \tag{4.3}$$

where E is the Young's modulus of silicon (2.10^{11} N.m ^{2}) and I is the quadratic moment of a beam of length b and height e

$$I_{X,Y} = \frac{eb^3}{12} \tag{4.4}$$

Supposing an homogeneous elongation (45^0) in the x and y directions, the projection over each axis is given by

$$\begin{cases} F_{X,Y} = \frac{1}{\sqrt{2}}(F_r + F_\vartheta) = \frac{3}{2}EI_{X,Y}\left(\frac{1}{nl_t^3} + \frac{1}{l_0^3}\right)\epsilon_x \\ \epsilon_x^2 = \epsilon_r^2 + \epsilon_\vartheta^2 \end{cases} \tag{4.5}$$

In consequence, the total stiffness of the springs in the horizontal case corresponds to

$$K_{X,Y\text{tot}} = 4K_{X,Y} = E\frac{eb^3}{2}\left(\frac{1}{nl_t^3} + \frac{1}{l_0^3}\right) \tag{4.6}$$

4.1.2 Spring stiffness: vertical case

In the vertical case, presented schematically in figure 4.3 right, the elongation, a, is negligible compared to the total length of the springs. As a consequence, the

deviation along z axis can be understood as the elongation of n springs of length, l_t, with a total length, l_0. The resulting stiffness is given by

$$K_{Z\text{tot}} = 4K_Z = E\frac{e^3 b}{2}\left(\frac{1}{nl_t^3 + l_0^3}\right) \tag{4.7}$$

For this design, Lennon demonstrated that a linear response of the springs is expected for a displacement up to $d_0/3$, where d_0 is the initial gap between the electrodes. For displacements larger than this value, the electrostatic force between the electrodes can not be balanced anymore, thus a collapse of the movable plate is expected.

4.2 Capacitive sensor: MEMS design

As mentioned above, we started to perform measurements on MEMS developed by Lennon et al. In its design, the stiffness values for the membrane are:
$K_{X,Y} = 617\ N/m$ and $K_Z = 105\ N/m$.

We are interested in performing measurements in the z direction so we checked if these parameters are suitable for our magnetic measurements. We are going to measure samples in the mg mass range. We first estimate the displacement induced by the mass of the sample.

$$\begin{cases} \text{for 1 mg} \rightarrow F \sim 10^{-5}\ \text{N} \\ K_Z \sim 100\ \text{N/m} \end{cases} \tag{4.8}$$

This results into an initial displacement of the electrodes (because of the sample mass) of $\Delta d = F/K_Z = 0.1\ \mu$m, thus no problem from the electrostatic force point of view is expected.

We expect that our capacitive detection will be able to measure capacitance variations $\Delta C/C_0 = 10^{-6}$. Thus, using equation 4.1, and with an initial gap of 30 μm, this corresponds to a displacement and a force of

$$\begin{cases} \Delta d/d_0 = \dfrac{10^{-6}}{30 \times 10^{-6}} \quad \Rightarrow \quad \Delta d \sim 3.10^{-11}\ \text{m} \\ F_Z = K_Z \Delta d \quad \Rightarrow \quad F_Z \sim 3.10^{-9}\ \text{N} \end{cases} \tag{4.9}$$

The Faraday force is proportional to magnetization, M, and to the field gradient: $\vec{F} = \vec{M} \cdot \nabla \vec{B}$. Therefore, considering that we are able to measure a Faraday force of 10^{-9} N, and to obtain the desired sensitivity of 10^{-8} A.m^2 (10^{-5} emu), a field gradient of 1 T/m is required. In conclusion, the above described design of the MEMS in the direction z, is suitable for the magnetic measurements we want to perform. If needed, an increase of the field gradient can produce higher sensitivities.

Lennon's design of the MEMS sensor (25 x 30 mm^2) is too large for our magnetometer, and thus a new design was required. Before, we performed thermal cycles on the existing sensors to see if they are suitable for low temperatures (Lennon et al performed measurements at room temperature). We encountered no problem at measuring the capacitance and no mechanical problems were observed.
An important aspect in our requirements is the condition $K_Z/K_{XY} << 1$. To satisfy it, we reduced the thickness e of the membrane (see equations 4.6 and 4.7), to values between 20-30 μm. Nevertheless, these membranes were shown to break easilty when manipulating them.
For these reasons, a new design of the geometry of the membrane was needed.

The development of the new membranes was conducted by S. Dufresnes (Nanofab - Néel Institute) with the help of O. Dasset (during his IUT internship). I was not involved in the design and the technological process of the membranes, but I supervised the characterization of the different membranes and together we obtained the characteristics of the final MEMS. The new requirements for our MEMS are:

- A Pyrex support of 25 x 25 mm
- An initial capacitance of 2 pF
- Suppress the extra electrodes previously used for lateral measurements
- A movable plate of ~ 60 μm thickness
- A stiffness $K_z \sim 66$ N/m, to reach the required sensitivity $\Delta M = 10^{-8}$ A.m^2, with $C_0 = 2$pF, $\Delta C = 10^{-6}$ pF, $d_0 = 30$ μm and a field gradient of 1 T/m
- $K_Z/K_{XY} << 1$

To achieve these requirements, we choose to keep the same spring geometry, but to vary the spring dimensions and numbers of arms. Table 4.1 shows the calculation

of the spring stiffness for several geometries.
We can see that for the 6^{th} case, the value for K_Z is smaller than the maximum value we had fixed (66 N/m), which should increase our sensitivity. In addition, the ratio between K_Z and K_{XY} is around 1% which is the best obtained ratio K_Z/K_{XY}. Therefore, this case offers a good compromise between the desired value of the K_Z value and the important factor, $K_Z/K_{XY} << 1$.

No	e (μm)	b (μm)	l_0 (μm)	l_t (μm)	n	K_{XY} (N.m ^{1})	K_Z (N.m ^{1})	K_Z/K_{XY}	Δd (μm)
1	30	40	840	840	8	364	20	0.06	0.49
2	60	40	840	840	8	729	162	0.22	0.06
3	60	53	840	840	10	1658	176	0.11	0.06
4	60	41	840	840	12	756	115	0.15	0.09
5	60	109	1990	2000	14	1055	20	0.02	0.51
6	**60**	**130**	**1990**	**2000**	**12**	**1810**	**27**	**0.01**	**0.37**
7	60	81	1990	2000	18	427	12	0.03	0.87

TABLE 4.1: Calculation of the spring stiffness. Δd corresponds to the displacement induced by a 10 mg sample placed on the membrane.

The new geometry of the springs has the following characteristics

- $n = 12$
- $e = 60$ μm
- $b = 130$ μm
- $l_0 = 1990$ μm
- $l_t = 2000$ μm

Unfortunately, when starting the fabrication process of the MEMS, S. Dufresnes and O. Dasset encountered problems. New materials (pyrex and doped silicon) had to be bought for developing these new membranes. But we could not find the exactly same materials as before. It resulted in many problems during the process: for example, the sealing between pyrex and silicon or the silicon etching did not work anymore. After numerous attempts, it was decided to start with a completely new nanofabrication process, in order to suppress the sealing step, and the highly doped silicon which were causing many problems. S. Dufresnes

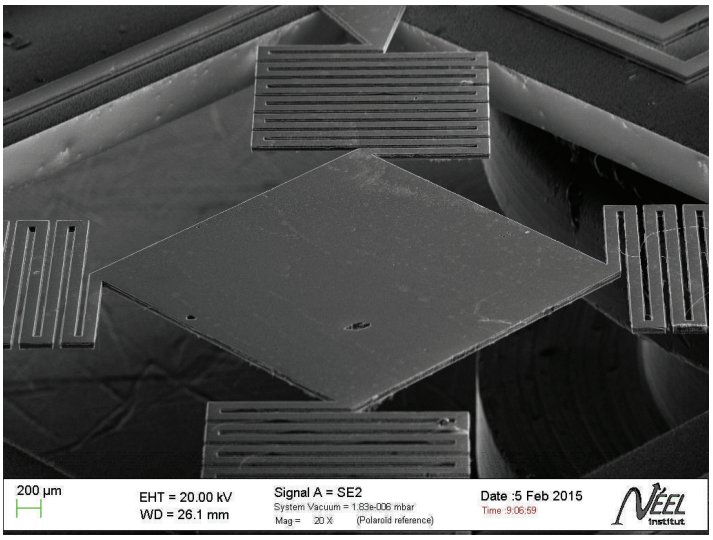

FIGURE 4.4: Nanofabricated MEMS: S. Dufresnes design.

developed this process: a metallic layer is now deposited on the "normal" silicon membrane, which is finally stuck on the pyrex support with GE varnish (see figure 4.4). The difficulty of this new process is to maintain a small enough distance between the membrane and the pyrex. New membranes are now available and ready to be tested.

4.3 Plastic capacitive sensor

Because of the problems in the MEMS fabrication process, I had no sensor to perform the magnetometer tests and I start to develop a new capacitive sensor. My goal was to have a functional sensor with which I could perform tests at low temperature and under high magnetic fields in order to validate the measurement. For this reason, I was looking for capacitive sensors easy to built. I took inspiration from the work of Slobinsky [2] for this design. I liked their idea of being able to change the gap between the two electrodes, and thus to vary the initial capacitance. Thanks to this feature, a wider range of mass samples can be measured.

Our requirements for the capacitive sensor and the sample holder is a diameter of 30 mm and a capacitor in the few pF range. Because we perform measurements at high magnetic fields, we want an insulating material for the sample holder to reduce the heating due to eddy currents.

Figure 4.5 shows the sample holder developed by me and built by A. Gerardin at Néel Institute (with the collaboration of M. Gibert for the 3D printing).

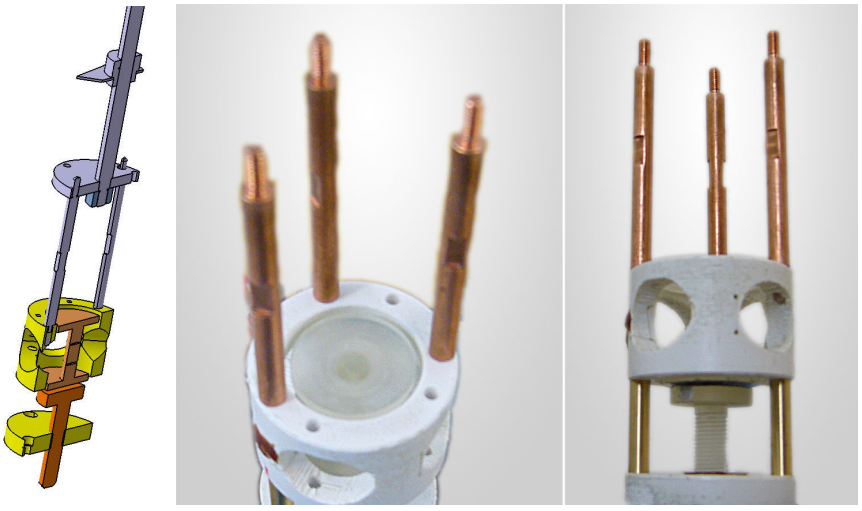

FIGURE 4.5: The "plastic sample holder": schematic view (left) and the capacitive sensor (right).

It can be separated into two parts.
The outer shell (yellow part in the schematic view), designed to support the two electrodes of the capacitive sensor, has a diameter of 30 mm. It is made out of two parts built with a 3D printer separated by three 1.5 cm copper rods.
The capacitive sensor is made out of two electrodes.
Two pairs of crossed wires, strung from x and y direction of the outer shell, are supporting the movable plate. They are made of a 0.14 mm diameter nylon wire.
The movable plate is made of two 15 mm cylindrical plates separated by a rod. On the upper plate we place the magnetic sample, while the lower part is the electrode of the capacitor. The crossed wires are drilled into the rod, two on the upper part and two on the lower part. This design permits the movable plate to move only on the z direction.
The "fixed" electrode can be screwed in the lower part of the outer shell. By screwing the "fixed" plate, we can change the gap between the two electrodes, thus the initial capacitor value.
The total set-up is about 4.5 cm height. The plastic sample holder is connected through three 5 cm copper rods (gray rods on the schematic view) to a 30 mm diameter copper plate on which are placed the thermometer and the reference capacitance needed for the capacitive measurement. A 22 cm copper rod (central gray rod on the schematic view) connects this plate to the mixing chamber.

At first, the two electrodes were made out of copper. We wanted to have a metallic surface for the capacitor and it would have been easier to thermalize a copper surface. However, the tests performed with this design proved not to be reproducible. We think that it was due to different charge distribution in the large metallic material for different measurements.

For this reason, we changed the material of the two electrodes to stycast, an insulating material (see figure 4.5). The two electrodes are painted with silver paste in order to obtain a conductive surface. To connect the electrodes to the measuring system, a 0.1 mm diameter copper wire is glued with silver paste on each electrode. These wires go to the outer shell, where they are soldered on a kapton relay, on which they are connected to low capacitance coaxial wires.

Tests to determine the stiffness of the springs have been conducted at room temperature. Several compounds of different masses have been placed on the movable plate. The unloaded and loaded capacitor were measured with a commercial capacitance bridge Andeen-Hagerling (AH) 2550A.

$$\begin{cases} \dfrac{\Delta C}{C_0} = \dfrac{\Delta d}{d_0} \\ mg = K_Z \Delta d \end{cases} \tag{4.10}$$

Using equation (4.10), we calculated a stiffness of ~ 110 N/m. The stiffness at low temperatures will be different than what we obtained at room temperature, but this measurement nevertheless allow to characterize the system. We have started the tests at 300 K with a capacitor of $\sim$ 4,164 pF, which is consistent with an initial gap between the electrodes of ~ 0.38 mm. A value of 4.22 pF was found for a 33 mg sample, which is consistent with a gap of 0.369 mm. Using equation 4.9, for a field gradient of 1 T/m, we achieved a sensitivity of 10^{-6} A.m^2 (10^{-3} emu).

As a perspective, this design can be further improved (test different wire diameters or material to find the optimal characteristics, or to improve the metallized surface, etc...), but for the time being, it provided a functional capacitive sensor to make progress on the electronic detection of the magnetometer.

Détection capacitive

Dans ce chapitre, je présente la chaîne de mesure que j'ai développée pour réaliser des mesures de capacité avec la sensibilité requise $\Delta C/C = 10^{-6}$ sur une capacité initiale de quelques picofarads.

Je montre tout d'abord les tests que nous avons effectués avec un pont de capacités commercial Andeen Hagerling, qui ont montré des soucis de stabilité, ne nous permettant pas de faire les mesures avec la sensibilité escomptée.

J'introduis ensuite le principe du pont de capacités que nous avons utilisés: les éléments nécessaires à sa réalisation: un générateur de signal ac, une détection synchrone, un diviseur inductif, un amplificateur et une capacité de référence à froid, située au plus près de la capacité à mesurer. Je présente deux types de montages que nous avons testés, en maintenant l'électronique de mesure à température ambiante. La sensibilité que nous avons obtenue n'étant pas satisfaisante, nous avons décidé de déporter une partie de l'amplification à basse température, afin de réduire le bruit accumulé par le fait de transporter un signal de bas niveau sur une longue distance (depuis la basse température à la température ambiante).

L'électronique à froid a été conçue au laboratoire pour satisfaire nos exigences de sensibilité. Elle est fixée sur la bride 4K du réfrigérateur du dilution à l'intérieur du calorimètre. Elle est notamment composée d'un transistor FET qui ne fonctionne qu'au-dessus de 100 K et qu'il est donc nécessaire de chauffer. Nous avons réalisé de nombreux tests de ce dispositif à température ambiante puis à basse température. Nous avons notamment relevé plusieurs instabilités associées à différents effets: notamment, problèmes de chauffage du FET, de connexions, et existence de boucles de masse dans le système.

Après avoir réglé ces problèmes nous avons effectué des tests de mesure de la force de Faraday avec le porte-échantillon en plastique présenté dans le chapitre

précédent. Nous avons pu montrer que le porte-échantillon lui-même ne donnait pas de signal magnétique mesurable. Nous avons ensuite testé la mesure avec un échantillon de $GeCo_2O_4$, qui présente des anomalies d'aimantation sous fort champ magnétique. Un fort signal était observé, mais que nous ne pouvions a priori pas associer à la variation d'aimantation. Nos mesures n'étant pas concluantes, nous avons testé un autre échantillon dont l'aimantation sature à quelques teslas, $Gd_3Ga_5O_{12}$. Là encore, au lieu de saturer, nous observions un fort signal sous champ magnétique, qui n'était pas corrélé à l'application d'un gradient de champ. Après avoir envisagé de nombreuses causes pour ce résultat, nous avons réalisé que l'échantillon n'était pas situé au centre de la bobine. Le fait qu'il soit soumis au gradient de champ induit par la bobine elle-même (qui augmente avec le champ appliqué) explique ces résultats. Malheureusement, la partie basse de la canne de mesure devant être déconstruite pour refaire un nouveau réfrigérateur à dilution, nous n'avons pu poursuivre ces tests.

Chapter 5

Capacitive detection

Our Faraday magnetometer uses a capacitive detection. This means that, when a field gradient is applied, the resulting Faraday force is measured through a change in a capacitance. For a magnetization sensitivity of 10^{-8} A.m^2 and for a field gradient of 1 T/m, we need to be able to measure a change in capacitance of $\sim 10^{-6}$ pF. Another important aspect is the stability of the measurement. We want to perform measurement in applied magnetic fields up to 16 T. Usually we work with a ramp of ~ 0.15 T/min, thus for a continuous ramp up to 16 T, we need ~ 1.5 hours. For a reliable measurement, we need a stability of roughly 3 hours.

5.1 Commercial capacitive bridge: Andeen-Hagerling 2550A

The first test of the capacitive detection was performed on a microelectromechanical system (MEMS) made of a silicon membrane, provided by the group of F. Ayela (LEGI, formerly CRTBT Grenoble). We measured the capacitance of the MEMS membrane using a commercial capacitance bridge Andeen-Hagerling (AH) 2550A. It has a sensibility of 10^{-7} pF [7] and it was proved to be reliable for the measurements of the groups of Sakakibara and Mackenzie. Figure 5.1 shows a schematic view of the capacitance bridge, calorimeter and the wires we used for this measurement. The AH 2550A capacitance bridge has an internal capacitor reference

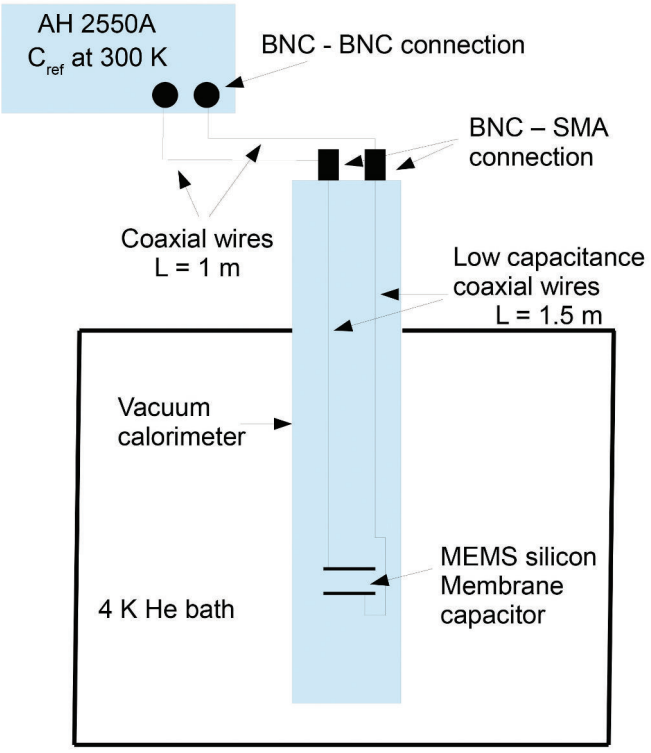

FIGURE 5.1: Schematic view of the capacitance measurement using a commercial capacitance bridge, AH 2550A.

at room temperature. The silicon membrane was placed in a vacuum calorimeter with a thermometer at a distance of $\sim$ 5 cm from it. Low capacitance wires ($C \sim 30$ pF/m), of $\sim$ 1.5 m long, were used at the interior of the calorimeter and normal coaxial wires to connect the calorimeter to the AH 2550A. The connection at the calorimeter level were made using BNC-SMA connectors and BNC-BNC connectors at the capacitance bridge level. I developed a labview software to read the capacitance and loss values of the AH 2550A capacitance bridge.

Figure 5.2 shows the measurements of the silicon membrane at 300 and 4 K. A good resolution is obtained in both 300 and 4 K measurements. However, a drift of the capacitance (10^{-2} pF at 4 K), and jumps are observed in the measurements. The reasons for this behavior can be two fold. The capacitance noise the wires are carrying from the capacitive sensor up to the capacitance bridge might impact the results of such small capacitor values ($\sim$ 2 pF), especially since long wires are connecting the reference capacitance (at room temperature) to the measured capacitance (at low temperature). In addition, the reference capacitance is subject

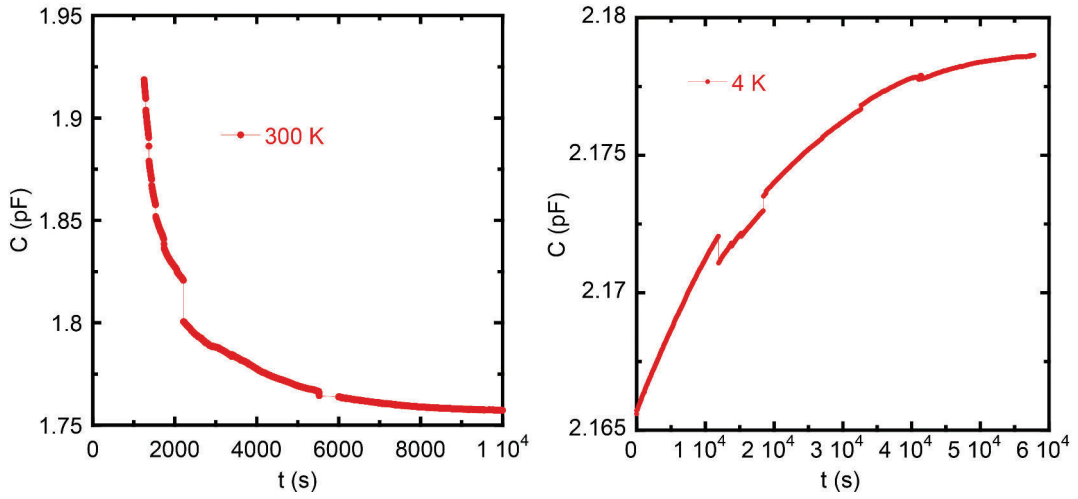

FIGURE 5.2: Capacitance measurement of the MEMS silicon membrane using commercial capacitance bridge, AH 2550A.

to the room temperature variations which might induce a drift in its capacitance value.

For these reasons, we decided to implement a home made capacitance bridge design. In this design, described below, the reference capacitance is placed at the proximity of the measured capacitance, thus increasing the sensitivity of the measurement.

5.2 Capacitance bridge: home made design

5.2.1 Principle of the home made capacitance bridge

Figure 5.3 shows a schematic view of our home made capacitor bridge design, developed at Néel Institute. It is composed of a seven decade inductive voltage divider ($\Delta L/L = 10^{-7}$) in parallel to the reference and measured capacitances. The reference and measured capacitances are placed close to each other, to ensure they have the same environment. We used a commercial capacitor of ~ 10 pF as the reference capacitance.

A 1 kHz signal is supplied through the inductive voltage divider. The bridge is equilibrated by adjusting the value N of the inductive voltage divider, so that the potential of the common point between the two capacitances is zero. The output

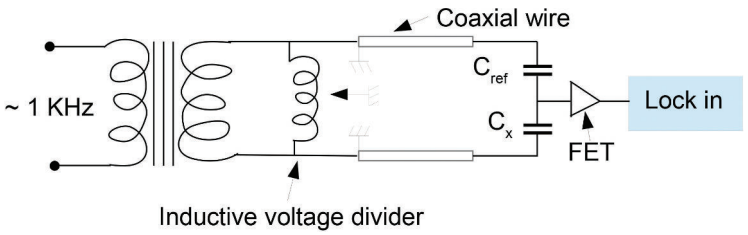

FIGURE 5.3: Schematic view of the capacitance measurement using the home made capacitance bridge design.

signal is then amplified by a field-effect transistor (FET - at 300 K), before being analyzed by lock-in detection. The design of the field-effect transistor allowed us to opt for different amplifier gains: 1X to 10000X.

Two different designs were tested (see figure 5.4). The difference between them relies in the way we connect the inductive divider to the two capacitances.

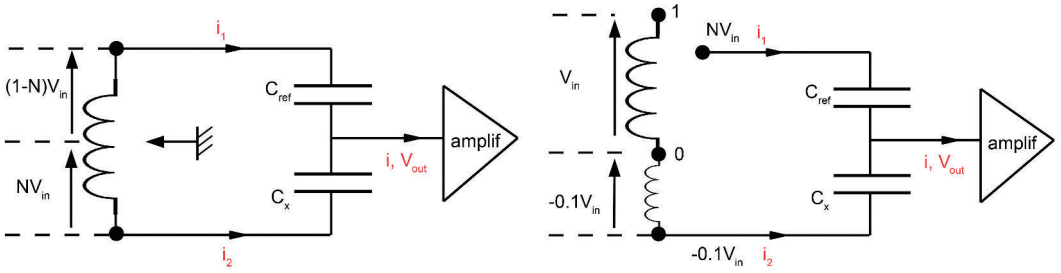

FIGURE 5.4: Home made capacitance bridge

In the first example (figure 5.4 left), a fraction, NV_{in}, of the input voltage V_{in} is driven through the measured capacitance and the rest of the voltage through the reference capacitor. Therefore, at the equilibrium,

$$\frac{C_{ref}}{C_x} = \frac{N}{1 \quad N} \tag{5.1}$$

where C_x is the measured capacitance and C_{ref} is the reference capacitance. In this design, we should expect that it is better to choose a reference capacitor with C_{ref} close to the measured capacitance C_x. This would result in a ratio, $N = 1/2$, and a half available range in each direction to equilibrate the capacitance bridge if it is imbalanced. However, the experience proved that a ratio $C_{ref}/C_x \sim 3$ is best suited for the available range on the inductive voltage divider, as well as for the output voltage values driven through the FET.

For small changes of C_{ref}/C_x, the output voltage, V_{out}, is given by

$$V_{out} = G \cdot V_{in} \left(\frac{C_{ref}}{(C_{ref} + C_x)} \quad N \right) \left(\frac{C_{ref} + C_x}{C_{ref} + C_x + C_{wires} + C_{FET}} \right) \tag{5.2}$$

where G is the gain of the field-effect transistor.
A large value capacitance (few hundreds of pF) is placed between the FET and the common point between the two capacitors. For this reason, the capacitance of the wires and that of the FET can be ignored, thus the second term in the above equation disappears, leading to

$$V_{out} = G \cdot V_{in} \left(\frac{C_{ref}}{(C_{ref} + C_x)} \quad N \right) \tag{5.3}$$

.

In the second case (figure 5.4 right), 10% of the input voltage is driven through the reference capacitor. With the use of the inductive voltage divider, a fraction $N \cdot V_{in}$ of opposite sign is driven through the reference capacitor in order to equilibrate the bridge. Neglecting the wire capacitance (for the same reason as above), the measured capacitance is given when the bridge is balanced by

$$C_x = 10 \cdot N \cdot C_{ref} \tag{5.4}$$

For small changes of C_{ref}/C_x, the output voltage, V_{out}, is given by

$$V_{out} = G \cdot V_{in} \left(N \cdot C_{ref} \quad \frac{C_x}{10} \right) \tag{5.5}$$

5.2.2 Electronic protocol for sensitivity tests

With two capacitors of fixed values, we are not able to test the electronic detection by using the Faraday force. Instead, an electronic protocol was developed in order to simulate a change in the capacitance. When the Faraday force will be exerted on the magnetic sample, a change in the measured capacitance occurs. This change will imbalance the capacitance bridge, which will result in a change in the output voltage.

Our solution is to change the ratio N of the inductive voltage divider. In the first circuit (figure 5.4 left), the voltage on both capacitors will change, and the

capacitance bridge is imbalanced. In the second case (figure 5.4 right), the voltage on the measured capacitance remains the same, however, the bridge is imbalanced by the potential voltage change on the reference capacitor.

As mentioned above, a large capacitor value is placed at the input of the field-effect transistor, so that the capacitance of the wires can be neglected. The maximum value for the input voltage is ~ 3 V. Following equation (5.3), for a measured and reference capacitances of a few pF, a change of N of the order of 10^{-6}, results in a 10^{-6} change of the output voltage. This is consistent with a shift of the capacitance of 10^{-6} pF.
In the second case, a 10^{-6} change of the ratio, N, is consistent with a 10^{-5} shift in the capacitance.

5.2.3 Tests of the home made capacitance bridge

Unfortunately, with the first design, we encountered stability problems and the measurements were not reproducible. Using the protocol described above, we obtained very noisy measurements and could only reach a sensitivity of 10^{-2}. We thus present below only the results with the second circuit.

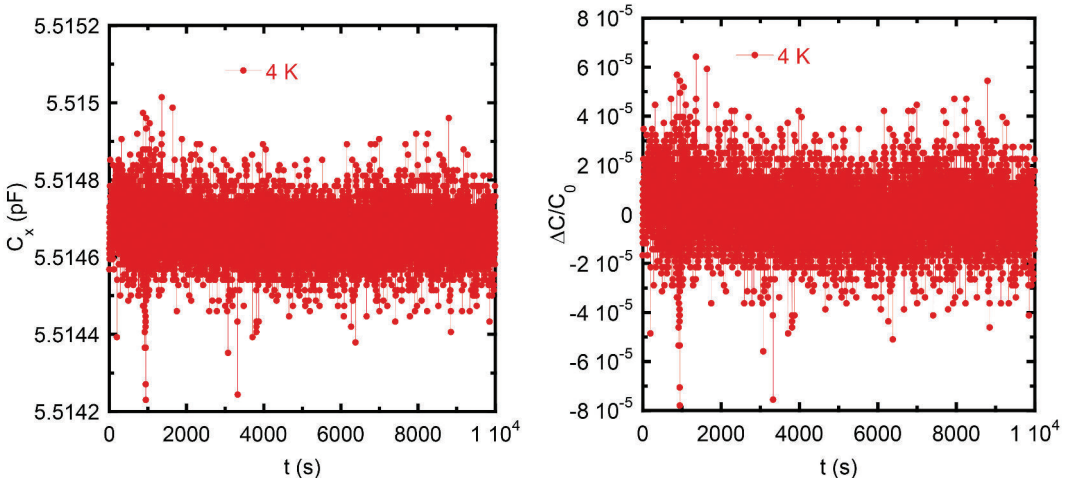

FIGURE 5.5: C_x as a function of time using the home made capacitance bridge

As mentioned above, the microelectromechanical system provided by the group of Ayela were fragile, therefore the few samples we had broke during the first tests. S. Dufresnes and O. Dasset were in charge of the design and building the new capacitive sensor, while I focused mainly on testing and improving the sensitivity

of the measurement. During the time they focused on creating new MEMS, I used commercial capacitors to test the electronic detection. I used several capacitors between 2 and 30 pF for the measured and reference capacitances.

Figure 5.5 shows the results performed at 4 K with a reference capacitor of 10.2 pF and a measured capacitance whose value is given to 5.2 pF. From our data and using equation (5.4), we calculate the value of the capacitor and the measured capacitance as a function of time is shown in figure 5.5 left. In this case, we used an input voltage of 0.8 V and a 3000X gain of the FET. The capacitor was measured in advance at 300 K with the commercial capacitance bridge, AH 2550A. The 5.5 pF value obtained using the equation (5.4) is in agreement with the 5.3 pF value obtained using AH 2550A. The difference between the measurements is due to the wire capacitance, as well as the temperature dependence of the capacitor (measurement at 300K - AH 2550A, 4 K with the home made bridge).

From figure 5.5, we can observe that the measurement is stable over the desired time range ($\sim$ 3 hours). However, the noise of the measurement is $\sim 10^{-3}$ pF. In the left picture, we plotted $\Delta C/C_0$, where C_0 was taken as the average value of the capacitance. When varying the inductive ratio N, we could achieve a sensitivity of 10^{-4}, still below the expected value ($\Delta C/C_0 = 10^{-6}$).

In order to further improve the sensitivity of the measurement, we placed an amplifier stage in the low temperature part of the dilution. Indeed, when we equilibrate the capacitance bridge to find the value of the measured capacitance, the output signal is very small (< 2 mV). As the FET is at room temperature, the wires capacitance and the potential noise trapped in the wires of $\sim$ 1.5 m length reduce the sensitivity of the measurement. By placing a cold amplifier stage as close as possible of the common point between the two capacitors, we theoretically increase the sensitivity of the measurement for these two reasons. The capacitance of the wires become negligible and by amplifying the signal, we reduce the influence of the noise through parasite capacitance.

5.3 Cold amplifier stage

By placing a cold amplifier stage at low temperatures, we decided to slightly change the components with the aim to increase the sensitivity of the measurement. Therefore, the new design is schematically presented in figure 5.6.

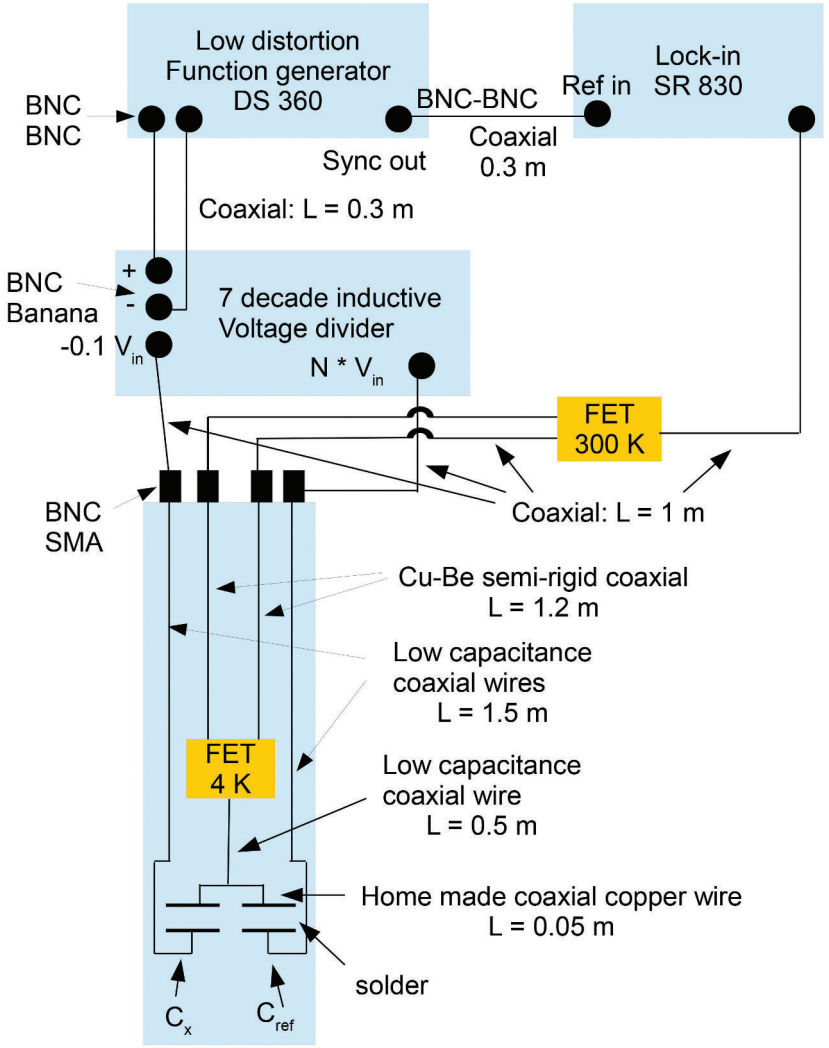

FIGURE 5.6: Schematic view of the home made bridge with a cold amplifier stage.

A low distortion function generator, Stanford Research DS 360, provides an alternative signal with frequencies between 10 mHz and 200 kHz. The signal is then driven through $\sim$ 0.3 m long coaxial wires to the seven decade inductive voltage divider. 1 m long coaxial wires (100 pF/m) connects the voltage divider to the calorimeter, from where the signal is driven through 1.5 m long low capacitance coaxial wires (47 pF/m) to the reference and measured capacitors.

We opted for low capacitance coaxial wires from several reasons: i) obviously, the main reason is the low capacitance value; ii) braiding ground shield to provide a better flexibility in the small available space and to reduce the heat effect due to thermal conductivity iii) stainless steel ground shield and conduction wire not to be perturbed by the applied magnetic field.

The connection between the two capacitors is made with a home made coaxial wire. It is made of a 0.1 mm diameter copper wire shielded by a copper-nickel capillary. The copper-nickel capillary is filled with Apiezon N grease in order to reduce the possible vibrations of the copper wire. The output voltage is then driven through a 0.5 m long low capacitance coaxial wire to the cold amplifier stage (FET). The FET was developed at Néel Institute by the electronic departement (J.L. Mocellin, O. Exshaw).
Figure 5.7 shows a schematic view of the cold and room amplifier stages. The connection between the cold and room temperature amplifier stages are made through two Cu-Be semi-rigid coaxial wires (96 pF/m). Normal capacitive wires are enough at this stage, because the signal is already amplified by the cold amplifier stage. The output voltage is then driven to the lock-in amplifier, SR 830, by a 1m long coaxial wire.

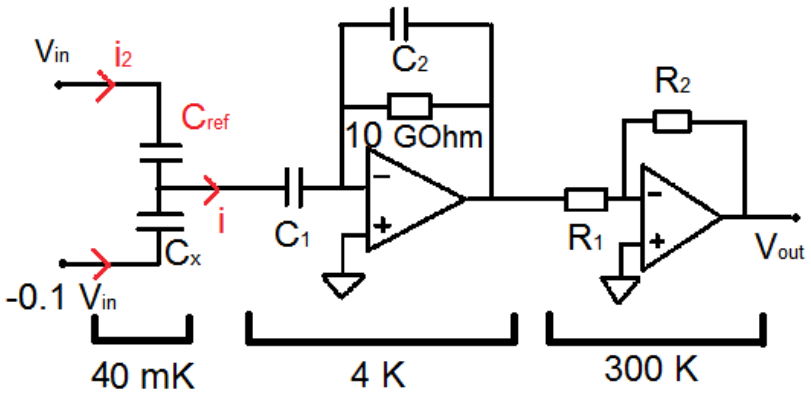

FIGURE 5.7: Schematic view of the cold and room temperature amplifier stages (developed at Néel Institute by J.L. Mocellin).

Capacitive measurements at very low temperatures are extremely sensitive. A careful shielding of the circuit from external noises is required. In addition, it is extremely important that the electrical ground is the same on the entire electrical circuit and to minimize at maximum its length. For example, if large enough ground loops are created, a parasite current will be created under applying the magnetic field.

The cold amplifier was first tested by the electronics department at room temperature. Figure 5.8 up, shows the simulation of the device using the Orcad pin spice software. Each sinusoid is the response of the device for a change of 10^{6} pF in the value of the capacitance. A change of 10^{6} pF corresponds to a change in the

output voltage of ~ 4 mV, with ~ 15 mV for a $5{\cdot}10^{-6}$ pF shift. In the lower part of the figure, a response of the device as a function of frequency can be observed. It is optimal for a frequency range between 400 Hz and 1 kHz.

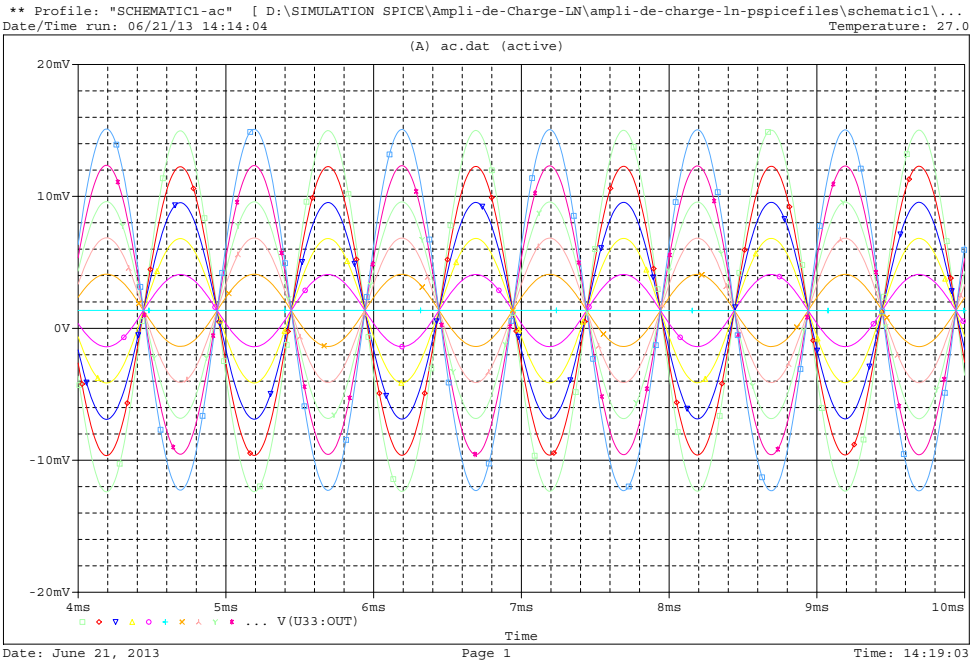

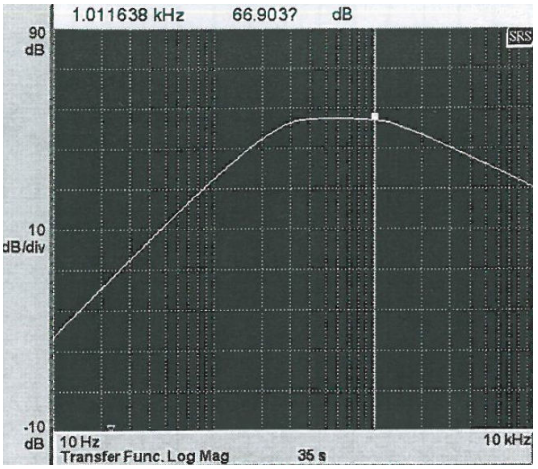

FIGURE 5.8: Test of the cold and room temperature amplifiers performed by the electronic department of Néel Institute.

By using a cold amplifier stage, new problems had to be resolved. The field-effect transistor works down to ~ 100 K. In order to make it working when fixed on the 4 K flange of our can, a heat resistance was placed on the FET. By supplying the resistance with a current, we heat the FET above 100 K by the Joule effect, and measurements can be performed. However, the FET is placed at very low

temperatures in a vacuum, thus several precautions had to be implemented not to heat the dilution refrigerator by radiation. For this reason, we wrapped the heat resistance and the FET in caf4, in order to reduce this effect. Several tests were performed in order to find the optimal resistance; with large enough surface to homogeneously heat the FET, the value of the resistance not to supply too large current values, etc. The final resistance is made on a 1x3 mm chip with a value of 1 kΩ, and is supplied with $\sim$ 2 mA current.

Using all these wires, an impact on the operation of the dilution refrigerator was observed. I rechecked the thermalization of the wires. As mentioned in section 2.3, all the wires were first thermalized on the 4 K flange. New points to thermalize the wires were added at the still, heat exchangers and sample holder level. Unfortunately, by working in a closed space with low diameter wires, a lot of time was lost due to rewiring the magnetometer due to broken wires.

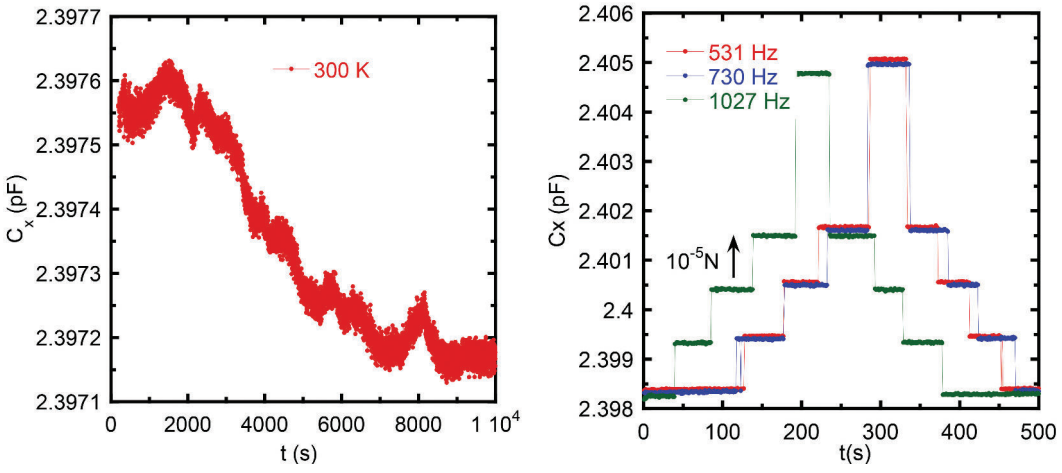

FIGURE 5.9: Test of the cold and room temperature amplifier stages at 300 K. Left: time dependence. Right: C_x as a function of the ratio, N, of the inductive voltage divider.

The cold and room temperature amplifier stages were provided by the electronic department in two closed and noise shielded boxes. I took advantage of these noise free environments and performed tests at 300 K, using two commercial capacitors. Figure 5.9 shows a 10^{-4} pF drift of the measurement. However, a 10^{-5} change of the ratio, N, of the inductive voltage divider can easily be measured. Therefore, we confirmed the electronic detection and proceed further to measurements on the Faraday magnetometer.

Figure 5.10 left shows the measurement with the cold amplifier using a commercial capacitor of 2.2 pF and a reference capacitor of 10.2 pF. The measurement was performed at room temperature. It is stable for our desired time range, however, a drift in the measurement is observed at longer times. This effect might come from the temperature dependence of the electronic components.

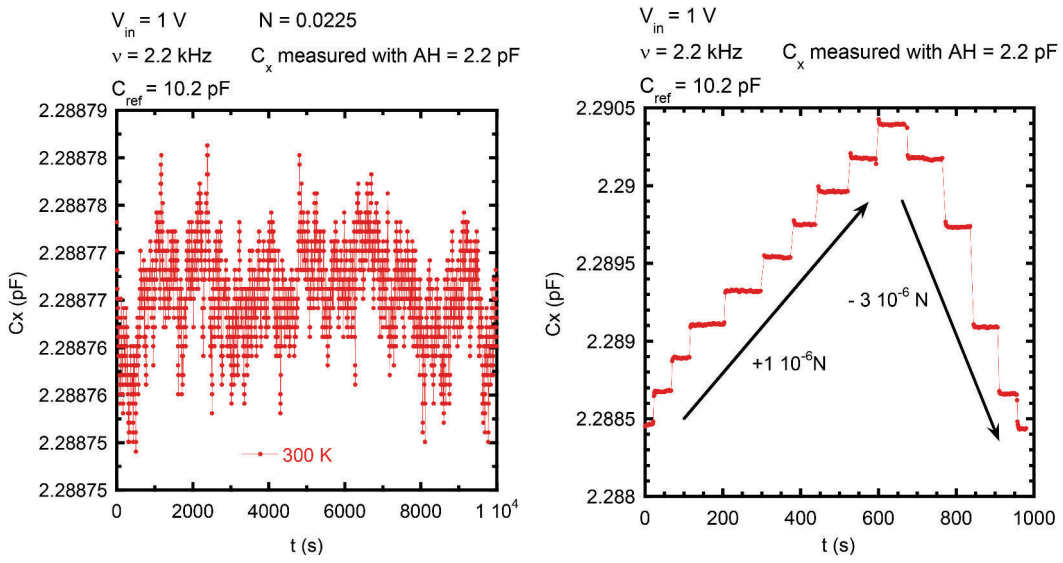

FIGURE 5.10: Capacitance measurement using home made capacitance bridge with a cold amplifier.

Figure 5.10 right shows the results for a 10^{-6} change of the ratio, N. From equation (5.4), we can observe that a 10^{-6} change of the ratio N, corresponds to a 10^{-5} pF shift in the capacitance. Therefore, at room temperature, with a commercial capacitor we have achieved a sensitivity, $\Delta C/C_0$ of $\sim 10^{-5}$ pF.

Meanwhile, the plastic sample holder was built by A. Gerardin, so I further focused on testing the electronic detection using the new developed sample holder.

5.4 Preliminary tests of the capacitive detection

5.4.1 Zero field measurements

The first tests were performed on the sample holder I had designed with a capacitive sensor made out of copper.

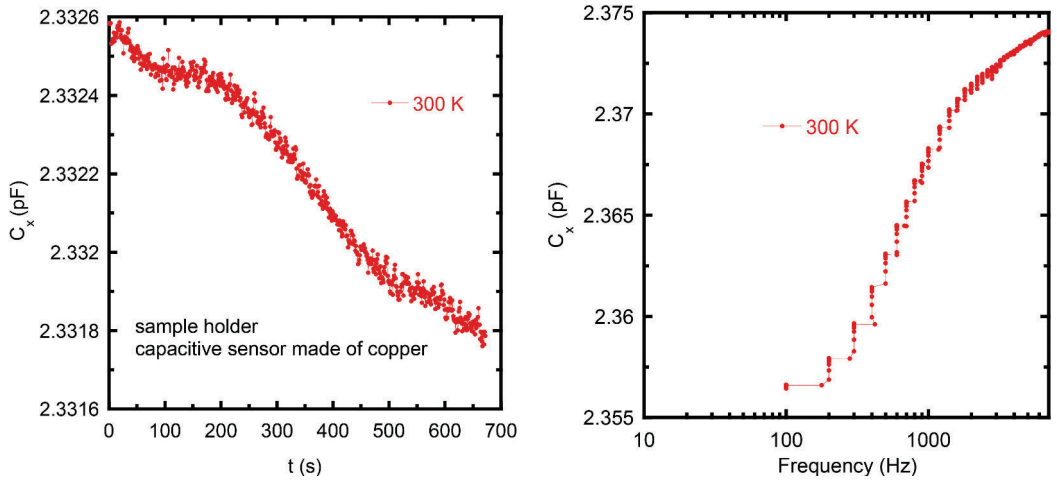

FIGURE 5.11: Measurement of the plastic sample holder with capacitive sensor made of copper.

Figure 5.11 shows the results performed at room temperature. The gap between the electrodes was chosen to obtain a capacitor value of $\sim$ 2 pF. It was first measured with the AH 2550A capacitance bridge and then with the electronic detection we had developed, with the FET amplifier in place in the calorimeter. The capacitive sensor was also positioned in the closed calorimeter, under vacuum, to ensure an isolated environment.

The value found with the home made capacitance bridge, $C_x = 2.33$ pF, is in a good agreement with the measurement performed with the AH 2550A bridge. This value gives, considering our two circular electrodes of 15 mm diameter, a distance between electrodes of about 0.66 mm, which is consistent with the distance we could estimate by the naked eye. However, an instable behavior can be observed as a function of time. The output voltage is stable during some periods of time, but for a duration of about one hour, a shift in the capacitance is observed. The results as a function of frequency display a sharp increase up to 1 kHz. For frequencies larger than 1 kHz, the increasing trend is maintained (see figure 5.11 right), which does not match with the expected behavior (see figure 5.8).

Faced with this odd behavior, several tests at room temperature were performed. Unfortunately, the obtained results were not reproducible (see figure 5.12). The differences between the measurements were attributed to the fact that the capacitive sensor was made of bulk copper ($\sim$ 2 cm width for each electrode). With such

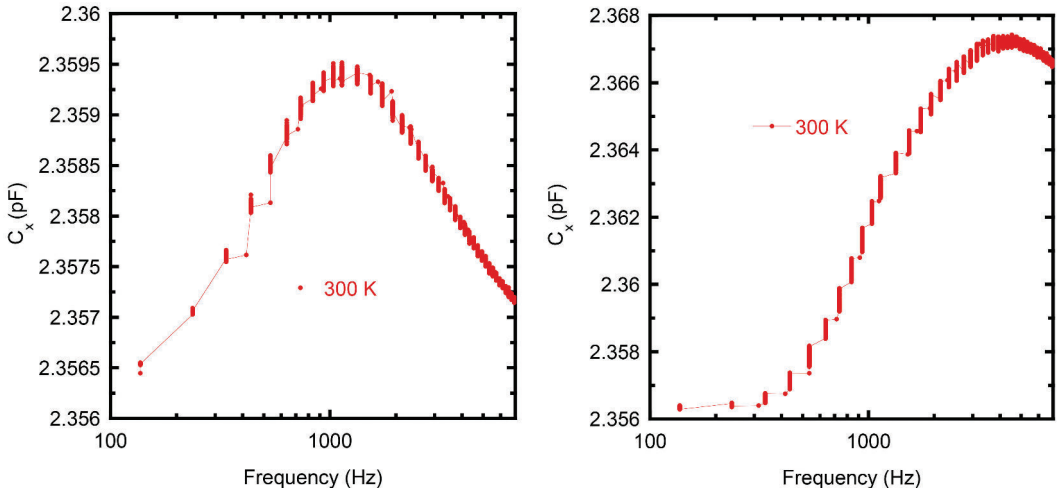

FIGURE 5.12: C_x as a function of frequency at 300 K for the plastic sample holder with capacitive sensor made of copper.

large metallic surfaces, the charge distribution can be different for each measurement, and the eletrode can pick up any spurious signal, thus leading to a different behavior as a function of frequency.

For this reason, we decided to change the capacitive sensor, and built it with an insulating material. The electrodes were realized by recovering the surfaces with silver paste, thus creating metallic surfaces. A copper wire was glued with silver paste on each electrode. On the other side, these wires were connected to the low capacitance coaxial wires on the outer shell of the sample holder by soldering them on a kapton relay.

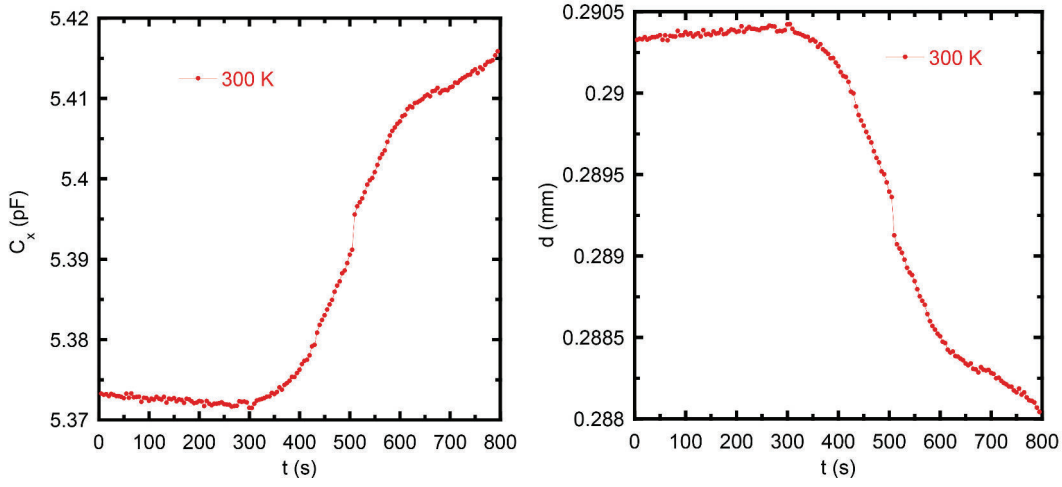

FIGURE 5.13: C_x as a function of time at 300 K for the plastic sample holder with capacitive sensor made of insulating material.

The measurements at 300 K for the sample holder with this "insulating" capacitive sensor are shown in figure 5.13. A relative stable measurement is observed for 5 minutes, but then a sharp increase is seen in the measurement. The corresponding distance shift is about 0.02 mm, as shown in the right figure. This distance shift between the electrodes might come from any external perturbation, i.e. vibrations, electromagnetic perturbations, since this room temperature assembly was not especially protected. Therefore, we decided to perform measurements at low temperature, where the magnetometer is expected to be less sensitive to external perturbations, thanks to the cryostat protection.

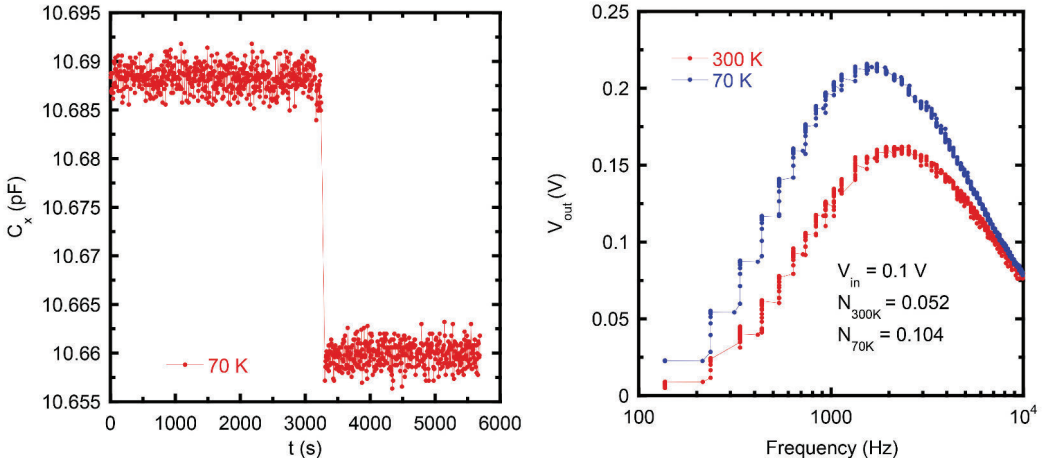

FIGURE 5.14: C_x as a function of time at 77 K for the plastic sample holder with capacitive sensor made of insulating material.

Figure 5.14 left shows the capacitance dependence as a function of time at 77 K. The measurement is stable in time for roughly one hour, then a jump is observed before regaining the previous stability. We attributed this jump in the measurement to a perturbation (a vibration which caused a movement of the two electrodes). From this effect, we concluded that the measurement is fairly stable at low temperature. However, the device seems to be susceptible to vibrations which can disturb the measurement.

Figure 5.14 right shows the frequency dependence of the output voltage at 300 and 77 K. I have plotted the output voltage instead of the capacitance to better observe the similitude between the two measurements. As mentioned above, we are using a lock-in amplifier to perform the data acquisition. By cooling down the capacitive sensor, the stiffness of the nylon springs are changing with temperature. This results in a saturated output voltage. The bridge was then equilibrated

with a new inductive voltage divider ration, $N = 0.104$ instead of 0.052 at room temperature. As the capacitor value depends on the ratio, N, the 77 K curve displays a larger frequency dependence compared to the room temperature one. These values are consistent with a capacitor of 5.31 pF and 10.624 for the 300 K and 77 K respectively. The change in the capacitance is consistent with a change of the gap between the electrodes from 0.29 mm at 300 K to 0.14 mm at 77 K.

At this point, the measurements were promising. The characteristics of the sample holder were not fully analyzed before building it, since it was developed quite fast to test the electronic detection of the magnetometer while we were waiting for the development of the new MEMS silicon membrane. However, its properties were shown to be satisfactory, which made us to reconsider it as a complementary sensor for samples with larger magnetic moments which do not require a high sensitivity. Therefore, we further focused on testing the device at low temperatures. Unfortunately, the 10 GΩ resistance of the low temperature FET broke. It was a chip resistor with solder terminals, and due to thermal dilation, it broke. A 10 GΩ resistor with wires was bought, but a 2 month delay was needed before this specific resistance could be acquired.

Approximatively two months later, we relaunched the low temperature measurements with the insulating capacitive sensor. Unfortunately, the measurements were not reproducible. Large variation in the output voltage were observed and the device was susceptible to any vibration (see figure 5.15).

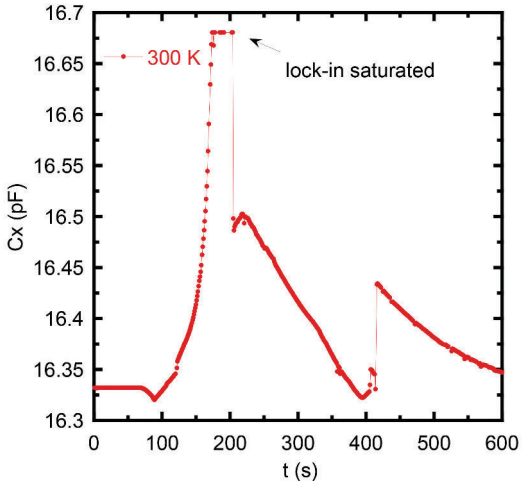

FIGURE 5.15: Large variation in the capacitance value as a function of time.

I started to think at the possible causes of such behavior. The first problem can be the existence of unwanted capacitances which disrupt the sensitive measurement. I rewired the entire magnetometer, paying attention to any soldering. Another important aspect is the ground of the measurement. In order to thermalize the wires which go down the dilution fridge, their ground were connected to the calorimeter at the 4 K flange level and on multiple points down to the lowest temperature as mentioned above. Unfortunately, this creates ground loops which disrupt the capacitive measurement. A compromise between the thermalization of the wires and the stability of the measurement was thus taken into account.
A better measurement stability was obtained. However, problems due to vibrations were still present. A cause for this effect can be the design of the fiberglass rod that separates the still from the mixing chamber. It is screwed with two bolts at each end and it seems that this system degraded in time, generating vibration of the entire lower part of the dilution. Unfortunately, only a limited improvement was possible, as the access to these bolts is limited by the heat exchangers.

5.4.2 Measurements under applied magnetic field

I started to perform capacitive measurements under applied field with the capacitive sensor described above. I remind the reader that a sensitivity, $\Delta C/C_0$ of 10^{-5} was obtained. However, vibrations seem to be the cause for perturbation in the capacitive measurement. Another important aspect is that these measurements were not performed in a persistent mode (described in chapter 3), but the ramp of the magnetic field was performed in a continuous mode.
Measurements of the empty sample holder (without any magnetic sample) did not show a signal as a function of magnetic field.

Tests with $GeCo_2O_4$

The first magnetic sample I measured was a single crystal of the spinel compound: $GeCo_2O_4$. This compound has an interesting magnetization behavior as a function of applied magnetic field. It does not saturate up to 10 T [8] (see figure 5.16) and it has a metamagnetic like transition around 5 T, depending on the direction of the applied magnetic field. A second transition around 11 T was observed in the [111] direction. This continuous magnetization increase on the entire applied magnetic

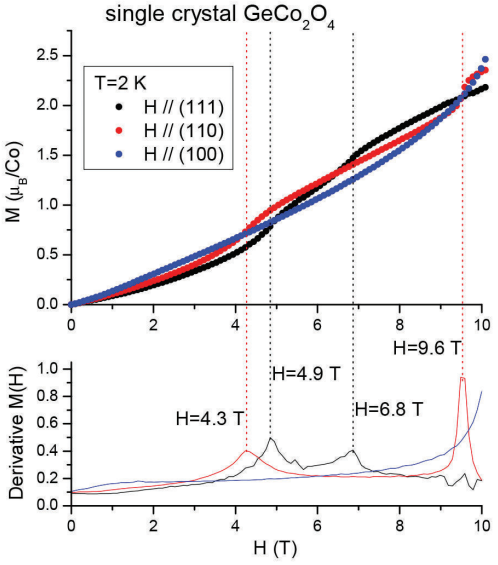

FIGURE 5.16: Magnetization measurements as a function of applied magnetic field for $GeCo_2O_4$. (from reference [8])

field range provided by our magnetometer, as well as the existence of anomalies in the magnetization measurement, make this compound an excellent test for our experimental set-up.

The single crystal of $GeCo_2O_4$ was glued on the capacitive sensor with the use of Apiezon N grease. No preferential direction was chosen for the applied magnetic field compared to the lattice axis of $GeCo_2O_4$, as the first tests were meant to confirm the electronic detection under applied magnetic field.

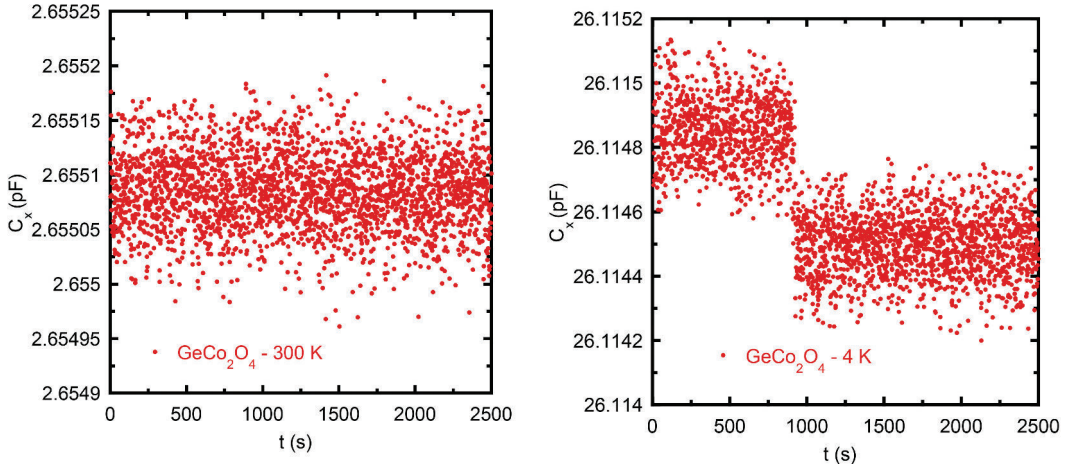

FIGURE 5.17: Capacitance measurement of single crystal $GeCo_2O_4$ using the plastic sample holder with the insulating material capacitive sensor.

Figure 5.17 shows the measurement of $GeCo_2O_4$ at 4 and 300 K, using the plastic sample holder with the insulating material capacitive sensor. The initial gap between the electrodes was chosen so that the capacitance at 300 K is $\sim$ 2 pF. These measurements were performed in the absence of the applied magnetic field.

An increase of the capacitance of a factor of 10 is observed at 4 K, which means that the distance between the two electrodes is ten times smaller than at room temperature. This effect cannot, a priori, come from the nylon wire contraction. However, as we can see in figure 4.5, the sample holder is made of different materials (both insulating and metallic), with different thermal dilatation coefficients. The three rods that separate the upper part from the lower part of the outer shell are made of copper while the outer shell is made of a plastic material, which is expected to have a larger thermal contraction. These different behaviors might change the sensor geometry at low temperature, thus affecting the measured capacitance.
The calculated distance for the capacitance value is $\sim$ 65 μm, twice larger than the expected value for the nanofabricated MEMS. It is acceptable for our measurements therefore we continued performing measurements under applied magnetic field.

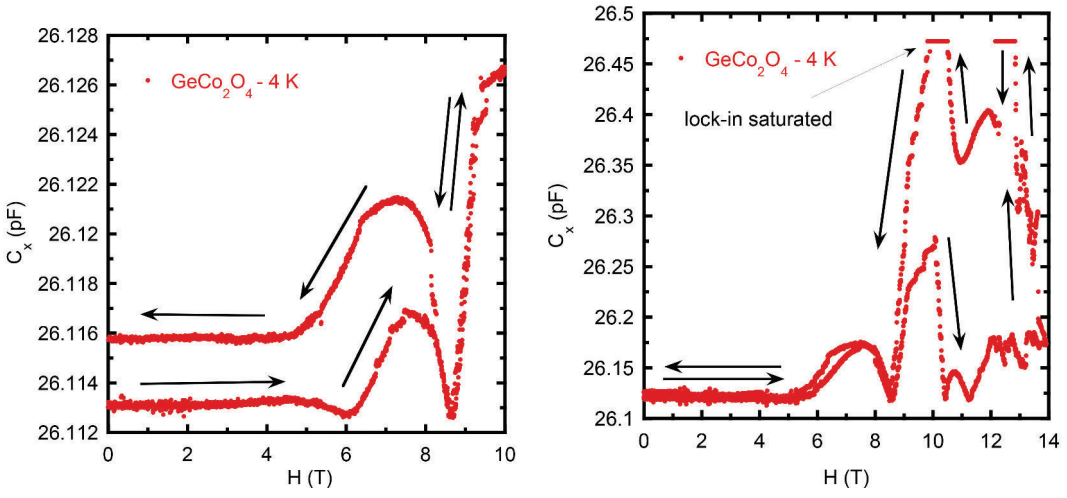

FIGURE 5.18: Capacitance measurement as a function of applied magnetic field for the single crystal, $GeCo_2O_4$, using the plastic sample holder with the insulating material capacitive sensor. left: field gradient of 0.75 T/m. right: field gradient of 1.1 T/m.

Figure 5.18 shows two measurements performed on $GeCo_2O_4$ as a function of the applied magnetic field at 4 K. The two measurements were performed with two

different field gradients. The left plot is performed with a field gradient of ~ 0.75 T/m, while the second is performed with a field gradient of ~ 1.1 T/m.

First, we can observe that the measurement is not reproducible. Even if we have different magnetic field gradients, the same shape of the curve is expected. Second, the behavior of the capacitive sensor is not the one expected. In an ideal measurement, an increase of the capacitance is expected, with the presence of a first anomaly between 4 and 6 T, and a second one around 11 T.

In our measurements, for a magnetic field gradient of 0.75 T/m, the capacitance remains unchanged until ~ 5 T, and then a sharp increase is observed. A large peak around ~ 7 T is observed. An hysteresis between the up and down magnetic field ramps is associated to this peak in the first measurement, that we did not observe anymore in the second measurement with a 1.1 T/m field gradient. Because the difference persists in the absence of the applied magnetic field in the first measurement (we could not recover the initial capacitance value), we attributed this hysteresis to a plastic deformation of the nylon wires. This could be due to the existing vibrations in the set-up: they induced a distance shift between the two electrodes of the capacitive sensor when the field was increased, and this shift persisted when decreasing the field. A possible improvement (outside of a better robustness of the dilution refrigerator) is to test different tensions of the nylon wires to find the optimal value between the sensitivity and the stability of the measurement. We bought a force meter to test this hypothesis but no measurements were performed yet.

For the 0.75 T/m measurement, an increase of the capacitance is observed for applied magnetic fields larger than 8.5 T, with no hysteretic behavior between the up and down ramps.
For a magnetic field gradient of 1.1 T/m and applied magnetic fields larger than 8.5 T, the capacitance becomes instable. An increase of the capacitance value is observed up to 10 T (the field value where we stopped the previous measurement) and then the device becomes instable. An erratic behavior can be seen and a saturation of the lock-in amplifier is observed around 14 T. When ramping down the magnetic field, the odd behavior persists down to ~ 9 T, when we recover the values for the up ramp.

Several field dependence cycles were conducted for different initial capacitance values. Unfortunately, the measurements were not reproducible at all, but anomalies

in the expected field range were always observed. Since this system has anisotropic properties, we suspected that non trivial torque effects could affect our measurements. We thus chose to perform further tests with an isotropic sample, which has a simpler magnetic behavior at 4 K: $Gd_3Ga_5O_{12}$.

Tests with $Gd_3Ga_5O_{12}$

I have studied a second magnetic sample, $Gd_3Ga_5O_{12}$ (GGG), during my PhD and a complete low temperature magnetic description can be found in chapter 4. At 4 K, it has a sharp increase of magnetization up to $\sim$ 3 T and then starts to saturate around 5-6 T. Therefore, a capacitance change is expected up to 3 T, with a change of slope between 3 and 7 T when the magnetic signal of the sample is saturated.

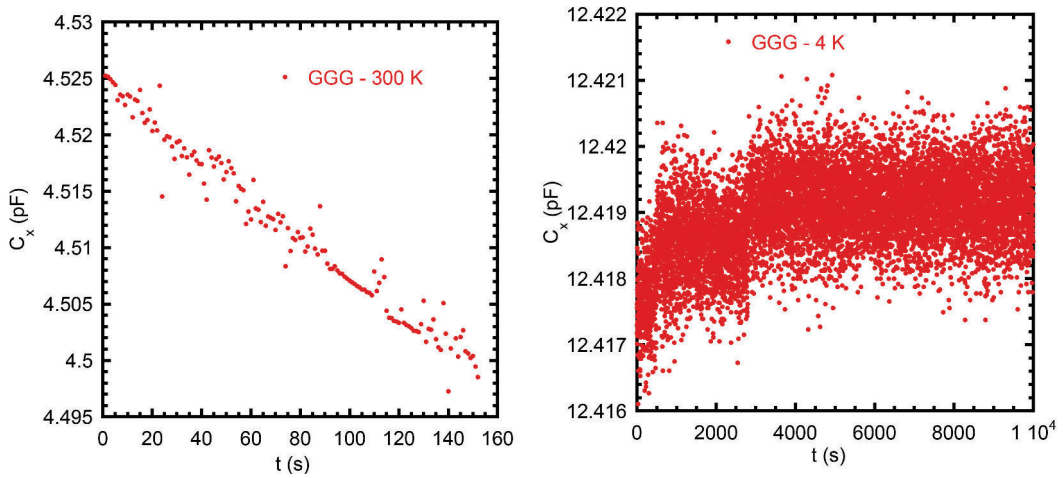

FIGURE 5.19: Capacitance measurement of single crystal $Gd_3Ga_5O_{12}$ using the plastic sample holder with the insulating material capacitive sensor.

Figure 5.19 shows the measurement as a function of time on a GGG single crystal using the plastic sample holder with the insulating material capacitive sensor. A capacitance shift is observed at 300 K, while a more stable measurement is seen at 4 K.

Figure 5.20 shows the measurement of GGG under applied magnetic field. Both measurement are performed with the same field gradient of 1.1 T/m, but the sign of the field gradient was changed between the two measurements. First, compared to $GeCo_2O_4$, the same shape of the curve is observed in both measurements and they are relatively similar for the up and down ramp. However, the noise is important

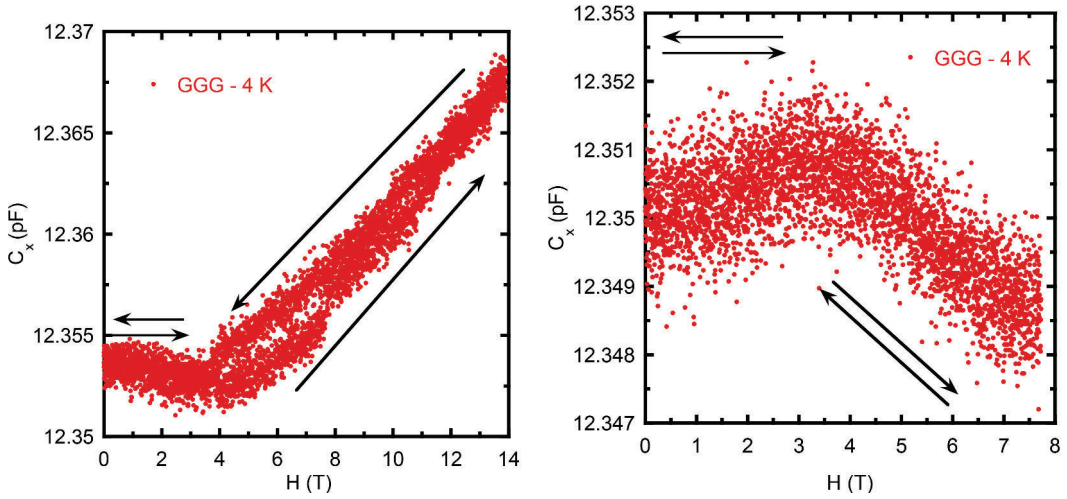

FIGURE 5.20: Capacitance measurement as a function of applied magnetic field for the single crystal, $Gd_3Ga_5O_{12}$, using the plastic sample holder with the insulating material capacitive sensor.

(10 ^{2} pF for the second measurement) and a difference in the amplitude is observed for the same field values. In addition, a hysteretic behavior can be seen between 4 and 6 T in the first measurement, while no such effect is found in the later.

A continuous increase of the capacitance is observed up to 14 T. The magnetization of GGG is saturated for applied fields larger than 6 T, therefore this signal cannot be attributed to a magnetization increase. From the equation of the Faraday force, $F_z = M_z \cdot \frac{\partial B}{\partial z}$, we can observe that it is proportional to the magnetization of the sample, as well as the field gradient. If an increase of the capacitance value is seen for applied magnetic fields larger than 6 T, this suggests that this increase is coming from the field gradient influence.

The position of the field gradient coils was checked again and no problems were found. A second test of the main coil homogeneity was performed. Unfortunately, we discovered a shift from the homogeneous point of about 4 cm. In these conditions, our sample is placed in the field gradient of the main coil, which is proportional to the applied field value. Looking at the curve shape of the capacitance field dependence of GGG, we can estimate that the seen signal is almost entirely coming from the field gradient of the main coil. If the signal of the magnetic sample was in the same value range as the one originating from the field gradient, an increase of the capacitance would have been observed up to 6 T (originating from magnetic sample and the field gradient influence) and then a change of slope and

a continuous increase of the signal (originating from the field gradient influence). However, this does not elucidate the odd behavior found in $GeCo_2O_4$.

Prospectives

With a lot of problems on the actual device, and the thesis almost at the end, a meeting with both cryogenic and electronic departments took place. Given the problems encountered during the measurements and taking advantage of their expertise, a new design of the low temperature part of the dilution refrigerator and the cold amplifier stage were developed.

An important aspect is the existence of three carbon rods between the still and mixing chamber. A better robustness of the device was achieved. This robustness is expected to improve the stability of the capacitive measurement as the set-up will be less sensitive to vibrations. The necessity of a heating resistance on the field-effect transistor disturbs the optimal operation of the dilution refrigerator. For this reason, a thermal shield was developed around the cold amplifier stage. It is made out of a copper cylinder thermalized on the 4 K flange and a super insulating shell to further reduce the heating effect of the environment due to radiation (see figure 5.21).

FIGURE 5.21: Old (left) and new (right) design of the cold amplifier stage.

In conclusion, the capacitive detection of the Faraday magnetometer was tested through three different methods. A 10^{-8} A.m^2 sensitivity is the aim for this measurement, but unfortunately it was not obtained so far. So far, the best sensitivity was $\Delta C/C_0 \sim 10^{-5}$, which corresponds to a sensitivity of 10^{-7} A.m^2 for a field gradient of 1 T/m. Different problems encountered during the three years of my thesis stopped us to have an operating magnetometer. However, I am confident that we are not far from making it work. New improvements on the design of the set-up are being made at this moment. With the work provided in this thesis, the person who will continue my work will have all the elements to make this magnetometer operate quickly.

Chapter 6

Conclusions

The necessity for magnetization measurements at very low temperatures and high applied magnetic fields with a high sensitivity is behind the project of my PhD. To this purpose, I have developed a Faraday force magnetometer which will operate at very low temperatures (40 mK) and high applied magnetic fields (16 T) with a high sensitivity (10 ^{5} emu). In this part, I presented our attempts to obtain these characteristics, with a design suitable for a large variety of magnetic samples. It involved the optimization of a dilution refrigerator, the development of a capacitive sensor, and the implementation of a high sensitivity capacitive detection.

The ^{3}He-^{4}He dilution fridge needed to reach very low temperatures was built at the Néel Institute. It has a standard design, with the use of a 1 K pot, a still, and a ^{3}He-^{4}He mixing chamber. The still and mixing chamber are made of copper and have a diameter of 45 mm. They are placed in a stainless steel vacuum calorimeter. We could determine the optimal working conditions for this dilution refrigerator: the circulation of a 36 L volume of ^{3}He-^{4}He mixture (25% ^{3}He), with a still working at 850 mK, leads to a base temperature of about 45 mK with a 500 mbar injection pressure, a 0.14 mbar aspiration pressure. The cooling power of this dilution refrigerator is: 20 μW at 100 mK with $\sim$ 5 μW losses, which is consistent with what is expected from its geometry.

We also developed field gradient coils, made of two copper coils with a 0.16 mm diameter wire, wound in opposite directions. They can generate a field gradient of 3.7 T/m/A.

Two sample holders were developed for this magnetometer. They are made on a movable electrode, on which will be placed the sample faced to a fixed electrode, so that a change of capacity can be measured when the Faraday force is exerted. A nanofabricated microelectromechanical system (MEMS membrane) based on a doped silicon membrane suspended above a gold electrode was presented. Initial tests were performed on MEMS with a geometry developed in the group of F. Ayela (LEGI) to check their low temperature robustness, and the possibility to measure their capacitance at very low temperature. These tests were satisfactory, and approve the principle of such MEMS. We thus modified their design to be suitable for our requirements: small size, robustness, high sensitivity along z, and rigidity along the x and y directions. To fulfill these conditions, we calculated a new geometry:
- a Pyrex support of 25 x 25 mm
- a movable plate of ~ 60 μm thickness
- springs with $n = 12$ arms of thickness $e = 60$ μm, and width $b = 130$ μm. The total lentgh of the spring is $l_0 = 1990$ μm with a width of $l_t = 2000$ μm.
The obtained initial capacitance is 2 pF, with spring stiffness of $K_Z \sim 27$ N/m with $K_{XY} \sim 1800$ N/m, which results in K_Z/K_{XY} of $\sim 1\%$.
Unfortunately, problems during the membrane process were encountered which required the development of a new nanofabrication process. The new membranes are now available, but no measurements were performed yet.

I developed a second sample holder, made of insulating material. It consists of two parts, the outer shell (30 mm diameter) made with a 3D printer and a capacitive sensor (15 mm diameter) made of insulating material, stycast. The capacitive sensor consists of a movable plate, suspended by two pairs of crossed nylon wires (0.1 mm diameter) from the outer shell, and a "fixed" plate that can be screwed. By screwing the fixed plate, the gap between the two electrodes is changed and a control over the initial capacitance value is obtained. The two electrodes are painted with silver paste in order to be conductive.

Both sample holders are connected to the mixing chamber through a 25 cm long copper rod. Tests of the dilution refrigerator with the sample holders were performed. Unfortunately, starting from this point, problems in the operation of the dilution refrigerator were observed. The base temperature was degrading daily and the system became unstable. Several unsuccessful tests were performed to find the origin of this effect. We decided to change the low temperature part of

the dilution refrigerator. Taking advantage of this, we redesigned it to ensure a better stability to vibrations.

A cold amplifier stage was developed with the aim of increasing the sensitivity of the measurement: it consists of a FET amplifier placed on the 4 K flange, and a room temperature amplifier, connected to the lock-in amplifier which performs the measurement.
First tests were performed at 300 K, before implementing this set-up in the dilution fridge. Measurements in the absence of the applied magnetic field, resulted in a sensitivity, $\Delta C/C_0 = 10^{-5}$. Then the first magnetic measurements were conducted. The measurements I performed on two magnetic samples showed unstable and irreproducible results. One of the reason for this behavior has been identified: the sample position was shifted of ~ 4 cm from the magnetic field center of the main coil. For this reason, the sample was in the field gradient of the main coil, which is proportional to the applied magnetic field. Therefore, when the magnetic field is swept, the Faraday force is varying not only due to the magnetization of the sample, but also due to a change of the field gradient. A second problem we encountered is the existence of mechanical vibrations due to the geometry of the lower part of the dilution refrigerator. The new design is more robust and an improvement of the electronic measurement is expected.

Although the magnetometer is still not operational, we have identified the reasons for most of the problems we have encountered during my PhD thesis. We could thus design the new dilution fridge taking into account these problems. Special care has been taken to avoid mechanical vibrations. In addition, the design at the 4 K flange level has been especially developed for the cold FET amplifier. The FET amplifier itself has also been redesigned to obtain more accurate electric contacts at low temperature. Shields have been added to prevent from radiation on the cold part of the dilution fridge. I could not have enough time to test all these components, but they are available right now so that I am confident that the magnetometer will operate within a short delay.

Part II

Frustrated systems

Introduction aux systèmes frustrés

Dans cette introduction, je présente brièvement les différents états magnétiques usuels, et le cas du magnétisme frustré, pour lequel un ordre magnétique standard ne peut s'établir malgré des interactions magnétiques fortes.

Chapter 1

Introduction

The most primitive magnetic phenomena, like the attraction of iron to loadstone, were no doubt observed before history recorded it. The first scientific discussion on magnetism is attributed to Thales of Miletus (625-545 BC) who said loadstone attracts iron [9], but the first recorded use of loadstone as a compass was made a few centuries later, 1088 AD, in the work of the chinese scientist Shen Kuo [10]. Nowadays, we live in a world in which almost every activity in our lives, from driving cars to medical treatment, depends on our mastery and comprehension of the forces of electricity and magnetism. The science research is focused on the discovery of different materials for technological applications, but also for fundamental research, to better understand and value the interesting and novel phenomena in such materials.

Today, magnetism of matter is understood as a cooperative phenomena arising from the spins of the unpaired electrons orbiting around the nucleus of atoms. It is basically a quantum effect related to the electron spin. Experimentally it is characterized by the response of the material to an applied external magnetic field through a pseudo vector quantity, called *magnetization*. Magnetization is the average of the magnetic moments in the material; when the system displays a linear response to the applied magnetic field, the relation between the applied field and the magnetization is given by: $\vec{M} = [\chi]\vec{H}$, where $\vec{H}$ is the applied magnetic field and $[\chi]$ is a dimensionless tensor called magnetic susceptibility. Magnetism and magnetic materials are a broad research domain right now, so I will start with a brief description of conventional magnetic behaviors expected in such systems.

Diamagnetism is a universal property which characterizes all materials with filled shells of atoms. Such systems display a small negative linear response to the external applied magnetic field.

In the case of materials with unpaired electrons in unfilled shells of atoms, there are additional magnetic behaviors. If the magnetic moments do not interact with each other, they behave as a collection of individual atomic "magnets" which tend to align to an external applied magnetic field and they remain disordered at finite temperature. Materials which exhibit such behavior are called *paramagnetic* and display a zero macroscopic magnetization in the absence of an applied magnetic field.

If the interaction between spins become relevant, adjacent magnetic moments will align in different magnetic structures. For example, in a *ferromagnet*, all the magnetic moments are parallel to each other. It has a spontaneous magnetization even in the absence of an applied magnetic field. In an *antiferromagnet*, antiparallel alignment of the magnetic moments is favored.

In most magnetic materials, thermal agitation (or temperature) is larger then the interaction between magnetic moments, preventing a magnetic ordering at ambient temperature. As a matter of fact, there are very few materials which exhibit magnetic ordering at room temperature in the absence of an applied magnetic field. The exception are the 3d and 4f transition metal compounds and alloys which provide soft and hard permanent magnetic materials, so important for technological applications. The study of different magnetic systems at low temperatures lead to the discovery of novel and unconventional magnetic states.

My work during my PhD was devoted to the experimental study of one such unconventional magnetic behavior, called *frustrated magnetism*. The frustration prevents from the stabilization into an classical ordered state, but the origin of frustration is manifold. It can arise due to disorder (spin glasses), due to the topology of the lattice and/or to a competition of interactions (spin ices, spin liquids). Before I introduce briefly the concepts of magnetic frustration and its consequences, I first describe the experimental techniques used during my PhD. I will then present the magnetic studies I have performed on geometrically frustrated systems with antiferromagnetic interactions: the hyperkagome compound $Gd_3Ga_5O_{12}$, and the frustrated molecular compounds Cu_{44} and Cu_3.

Méthodes expérimentales

Dans ce chapitre, je présente les différentes techniques expérimentales que j'ai utilisées pour mesurer les propriétés magnétiques des échantillons que j'ai étudiés.

Je présente tout d'abord le fonctionnement des magnétomètres à SQUID. Cela inclut deux types de magnétomètres: i) des magnétomètres commerciaux Quantum Design, permettant d'atteindre des températures jusque 2 K, que j'ai utilisés pour caractériser les échantillons à "haute" température. ii) des magnétomètres développés au laboratoire, équipés de réfrigérateurs à dilution miniature permettant de travailler à très basse température (60 mK), que j'ai utilisés pour faire des études fines sur les composés étudiés (aimantation et susceptibilité alternative).

J'introduis ensuite le principe des mesures de diffusion de neutrons, et en particulier de neutrons polarisés. J'ai en effet participé à de telles expériences sur le diffractomètre D7 de l'ILL pour les études sur le composé $Gd_3Ga_5O_{12}$.

Chapter 2

Experimental Methods

During my thesis I have mainly performed magnetic measurements on several low temperature magnetometers. For the temperature range 2 - 300 K I used two commercial MPMS SQUID magnetometers (Quantum Design SQUID and Quantum VSM SQUID). For the temperature range 80 mK - 5 K, I used two SQUID magnetometers developed by Carley Paulsen at the Néel Institute [11], which I will label from now on *Low temperature SQUIDs magnetometers*. I also participated to the neutron scattering measurements conducted by our collaborators Pascale Deen (ESS Lund, Sweden) and Henrik Jacobsen (PhD student). So I will first present the principle of SQUID magnetometers, and a brief description of the instruments I used during my PhD. Then I will make a short introduction into neutron scattering measurements.

2.1 SQUID Magnetometers

2.1.1 Josephson effect

The detection method of our magnetometers is based on a SQUID sensor. A Superconducting QUantum Interference Device (SQUID) is the most sensitive magnetic flux sensor currently known. It consists of two superconductors separated by thin insulating layers to form two parallel *Josephson junctions* (see figure 2.1). To understand how a SQUID works means to comprehend the Josephson junctions. In 1962, B.D. Josephson showed that if two superconductors are separated by a

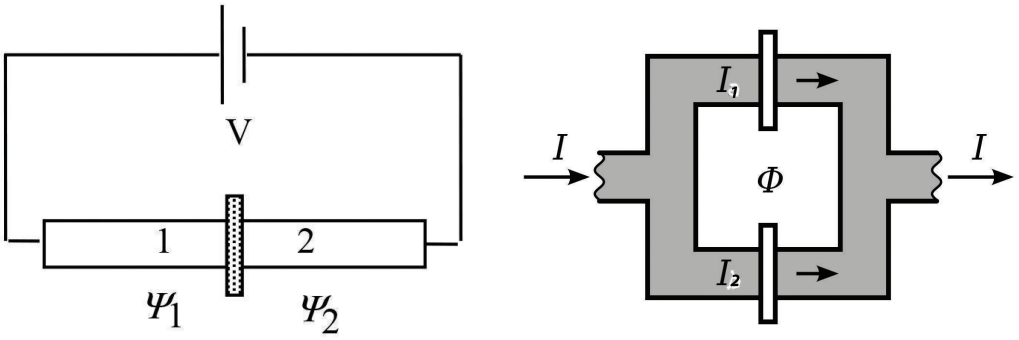

FIGURE 2.1: Left: Two superconductors separated by a thin insulator. Right: Two junctions in parallel which create the SQUID sensor.

thin enough insulating barrier, there is a possibility for Cooper pairs to tunnel. This effect later became known as *Josephson tunneling*. The wave function for each superconductor can be written as a function of the density of Cooper pairs, n_1 and n_2, and the phases of the order parameter of the two superconductors ϕ_1 and ϕ_2

$$\begin{cases} \psi_1 = \sqrt{n_1} e^{i\phi_1} \\ \psi_2 = \sqrt{n_2} e^{i\phi_2} \end{cases} \tag{2.1}$$

The dynamics is then determined by the Schrödinger equations

$$\begin{cases} i\hbar \frac{d\psi_1}{dt} = \mu_1 \psi_1 + K\psi_2 \\ i\hbar \frac{d\psi_2}{dt} = \mu_2 \psi_2 + K\psi_1 \end{cases} \tag{2.2}$$

where K is a constant that represents the coupling across the barrier and μ_1 and μ_2 are the lowest energy states for each superconductor.
The Cooper pairs will create a supercurrent $I = dn_1/dt$. If a voltage, V, is applied between the junctions, a shift (μ_2 - μ_1 = 2eV) of the energy levels will occur. Taking this into account and substituting equations (2.1) into (2.2) we get

$$\begin{cases} I = I_0 sin\Delta\phi \\ \frac{d\phi}{dt} = \frac{2eV}{\hbar} \end{cases} \tag{2.3}$$

where $\Delta\phi = \phi_1$ - ϕ_2. Equations (2.3) are valid as long as the applied current between the junctions is below the critical current I_0, and the effect is called **DC Josephson effect**.

When a DC current larger than I_0 is applied to a Josephson junction, an oscillation of frequency f occurs in the junctions. The resulting current through the junction which oscillates at the frequency f is described by

$$\begin{cases} I = I_0 sin\frac{2eV_0(t)}{h} \\ f = \frac{d(\Delta\phi(t))}{dt} = \frac{2e\Delta V}{h} \end{cases} \tag{2.4}$$

This effect is known as the **AC Josephson effect**.

2.1.2 Principle of SQUID

A SQUID sensor is schematically presented in figure 2.1 right. If a current is injected into the two Josephson junctions, the output voltage of the SQUID can be measured. If the two junctions have the phase difference $\Delta\phi_1$, respectively $\Delta\phi_2$, the total current drawn through the SQUID will be

$$I_{tot} = I_0 sin\Delta\phi_1 + I_0 sin\Delta\phi_2 \tag{2.5}$$

The phase differences $\Delta\phi_1$ and $\Delta\phi_2$ depend on the total flux, Φ, induced in the loop by the external magnetic field. By summing the phase contributions from the flux and junction in the loop we get

$$\Phi = \oint \overrightarrow{A}(\overrightarrow{l})d\overrightarrow{l} \tag{2.6}$$

$$\frac{2\pi\Phi}{\Phi_0} + \Delta\phi_1 \quad \Delta\phi_2 = 0 \tag{2.7}$$

where $\overrightarrow{A}$ is the magnetic vector field of the path l on the SQUID sensor. By combining (2.5) and (2.7) we get the expression for the total current through the SQUID

$$I_{tot} = 2I_0 \left|\cos\left(\frac{\pi\Phi}{\Phi_0}\right)\right| \tag{2.8}$$

We observe that the total current is maximal if the total flux is a multiple of the quantum flux, Φ_0. The characteristic curve of a DC SQUID is displayed in figure 2.2. The total current is periodic as a function of the total flux induced by the external magnetic field.

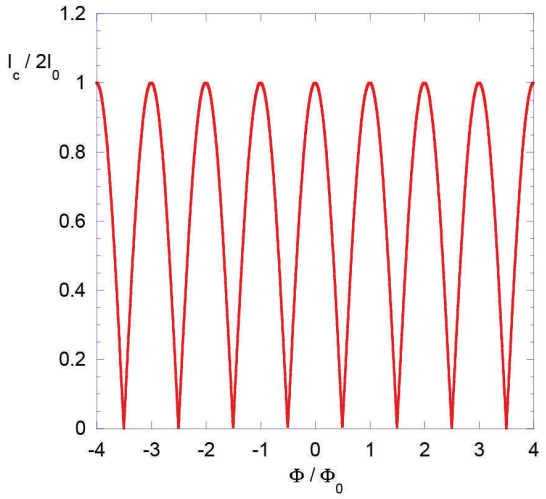

FIGURE 2.2: Critical current as a function of the total flux for a SQUID loop

2.1.3 SQUID feedback technique

In this section I present a brief description of the way SQUID sensors are implemented in magnetometers. Figure 2.3 presents a schematic view of the feedback

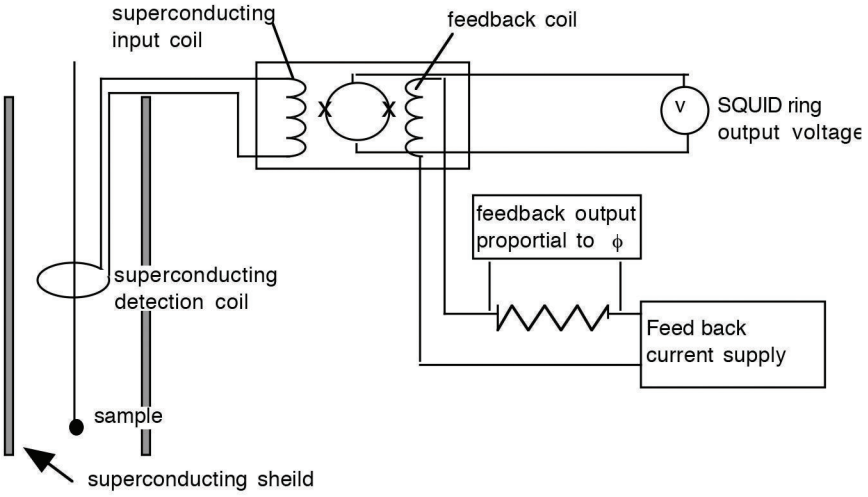

FIGURE 2.3: Feedback technique using a SQUID sensor. (from reference [11])

technique, used for the usual SQUID magnetometers. The SQUID sensor is treated as a "black box" with the following characteristics:

- At the input of the SQUID sensor a small superconducting coil is coupled inductively with it.

- The output of the SQUID is a voltage proportional to the critical current of figure 2.2.
- A second feedback coil is coupled inductively with the SQUID sensor.
- The SQUID sensor is well shielded from stray magnetic fields.

If we start the measurement with the sample far away from the detection coil, no output voltage is measured (point 1 in figure 2.4). When the sample approaches the

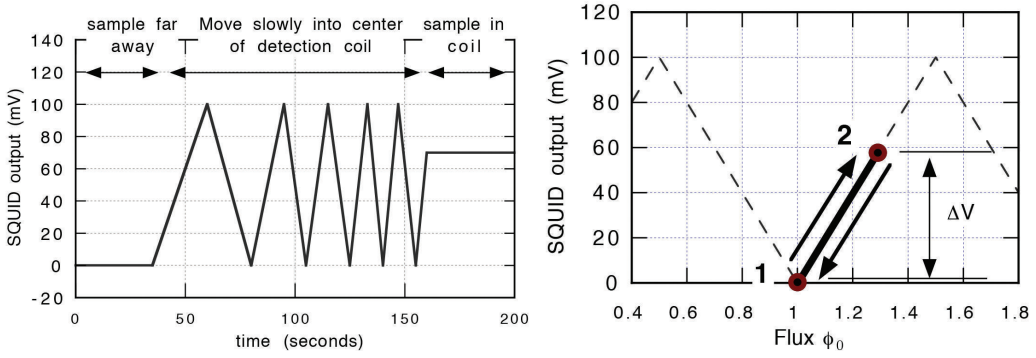

FIGURE 2.4: SQUID output using feedback technique. (from reference [11])

superconducting detection coils, the SQUID sensor measures the flux change and an output ramp voltage is detected up to point 2 where we stop the measurement. At point 2, a small current is sent back to the feedback coil such as the voltage, V, is brought back to zero. In this way, the flux from the feedback coil cancels that from the input coil. Then, we continue to move the sample towards the center of the detection coil, increasing the feedback current, until the sample is in the center, and the SQUID output voltages remains zero. The voltage across the feedback resistor is proportional to the flux in the SQUID sensor which in turn (thanks to a calibration with a known sample) is proportional to the magnetic moment of the sample.

2.1.4 MPMS SQUID magnetometers

The magnetic measurements at *high temperatures* were performed on two commercial SQUID magnetometers: the MPMS and MPMS VSM Quantum Design apparatus. In both magnetometers, a SQUID sensor is used, but the magnetization of the sample is not measured directly, but through a superconducting coil

which is coupled inductively with the sensor, as explained above. Because the SQUID is extremely sensitive to magnetic fluctuations, the first requirement is to isolate the sensor from all the magnetic sources. Usually, the SQUID is placed outside of the main coil into a superconducting magnetic shield.

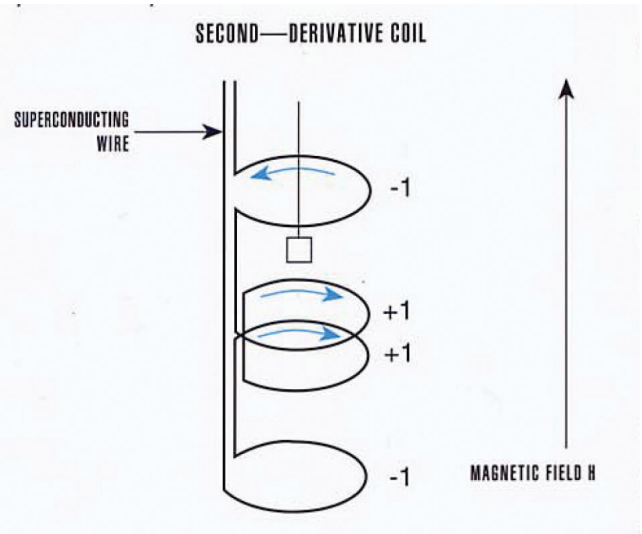

FIGURE 2.5: Detection coils (from reference [12])

Figure 2.5 displays the detection coils (designed as a second order gradiometer) we usually find in commercial SQUID magnetometers. They are positioned at the center of the superconducting magnet in such way that the magnetic field created by the sample couples inductively when it moves through them. The gradiometer coils are used to lower the noise of the measurement caused by the background and fluctuations in the large magnetic field created by the superconducting magnet.
A superconducting coil is used to apply external magnetic fields up to 5 T for a temperature range between 2 and 400 K. The design of the detection coils with the use of a SQUID sensor permits to achieve a sensitivity in the range of 10^{-9} emu. A more detailed review on MPMS magnetometers can be found in the book of McElfresh [12].

2.1.5 Very low temperature SQUID magnetometers

The very low temperature magnetic measurements were performed on two home made SQUID magnetometers [11]. They are equipped with DC squid sensors, and

they permit to obtain absolute values of magnetization and susceptibility for a temperature range between 60 mK and 5 K, with a sensitivity in the range of 10^{-7} - 10^{-9} emu, depending on the measurement.

- The high magnetic field SQUID magnetometer: it can perform magnetization and AC susceptibility measurements in magnetic fields up to 8 T.
- The low magnetic field SQUID magnetometer: it is suitable for magnetic measurements in low applied DC magnetic fields ($10^{-3} < H_{DC} < 2000$ Oe). Its great stability allows AC susceptibility measurements down to very low frequency (1 mHz, $H_{AC} < 5$ Oe) and magnetization relaxation measurements up to several days.

I describe below the design of the high magnetic field magnetometer, but the design is the same for both magnetometers (see figure 2.6). The sensor is inductively coupled (first order gradiometer) with a DC SQUID which is shielded by a NbTi-tube and placed outside the field created by the main coil. The output of the SQUID is measured through a Keithley-multimeter (magnetization) or a lock-in amplifier (AC susceptibility), and recorded by the control computer.

The magnetometers uses two coils. For low fields, due to flux trapping in the superconducting coil, a Hall gauge is used to measure the value of the field. A superconducting DC coil allows measurements up to 8 T and a small AC coil is used for the AC susceptibility measurements. The signal of the AC coil is induced by the lock-in amplifier from an outside reference source. The use of the lock-in amplifier provides access to AC magnetic susceptibility given by

$$\chi_{AC} = \chi' \quad i\chi'' \tag{2.9}$$

where χ' is the in phase part and χ'' is the part in quadratic phase with the AC field. In addition, a DC magnetic field can be applied granting us full χ_{AC} measurements: dependence on the temperature, on the amplitude of the DC and AC magnetic fields and on the frequency of the AC magnetic field. The frequency range is between 1 mHz and 3 kHz.

A NbTi superconducting shield is placed between the detection and main coils to stabilize the field and for noise protection. The sensitivity of the SQUID sensor can be reduced by a set of inductive shunts placed between the gradiometer and

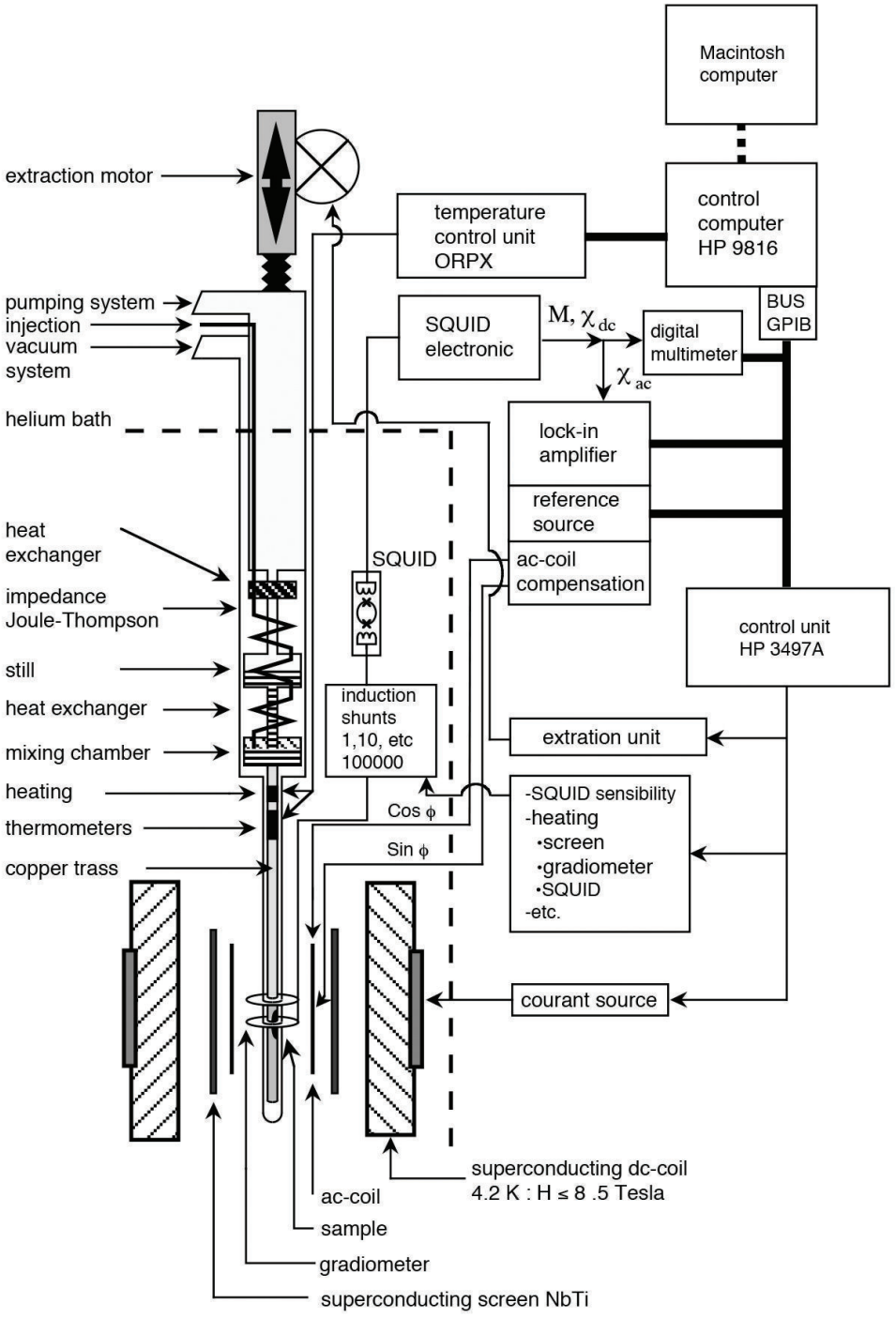

FIGURE 2.6: Scheme of the high field very low temperature SQUID magnetometer developed by C. Paulsen (from reference [11])

the SQUID. This shunt system reduces the signal by a factor of 10 to 10^6 for a sensitivity of the order of 10^{-7} - 10^{-9} emu.

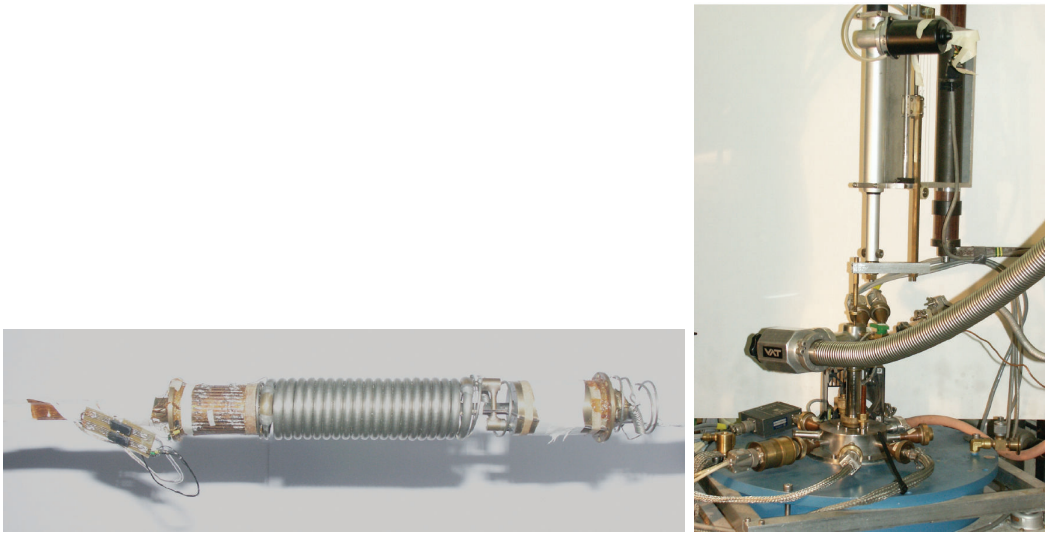

FIGURE 2.7: Left: Miniature dilution fridge. Right: The extraction method. (refer to the text for more details)

Both magnetometers use a miniature dilution fridge (see figure 2.7 left. For more details about dilution fridges see section 2.1). In these dilution fridges, the 1 K pot is replaced by a compressor which injects the ^{3}He-^{4}He mixture through two Joule-Thomson impedances. This design permits the use of a can of only 30 mm wide and has the advantage of being cooled down very fast (around 3 hours). The sample holder is made of two copper bars screwed into the mixing chamber. The sample is placed between the two copper bars and thermalized with the use of Apiezon N grease. The thermometer is placed around 10 cm above the sample.
The can is moved through the detection coils using an extraction engine which allows vertical movement up to 4 cm without heating the mixing chamber or the sample (see figure 2.7 right). The sample can be moved between two positions of maximal induction of the detection coils. Being able to position precisely the can into the anti-Helmholtz detection coils and measuring the variation of the flux, permits to obtain absolute values of the magnetization or susceptibility.

2.2 Neutron scattering

The neutron is an elementary particle predicted by E. Rutherford in 1920 and discovered by J. Chadwick in 1932 [13]. Its first use in neutron diffraction experiments was in 1946 by C. G. Shull and E. O. Wollan, who thus proved the antiferromagnetism predicted by L. Néel. Inelastic neutron experiments were first performed in 1955 by B. N. Brockhouse to probe phonon excitations. Since then, neutron experiments have become a very powerful technique in condensed matter due to:

- Neutron's energy, $E = h^2/2m\lambda^2$ (where h is the Plank constant and m is the neutron mass), which can be lowered after production by collision in heavy water in the range of excitations of condensed matter ($\sim$ 0.1 100 meV). Its wavelength λ is then of the same order of magnitude as the interatomic distances in most of the materials ($\sim$ 1 30 Å), what makes it ideally suited for probing the static and dynamical correlations at these spatial scales.
- Neutron's spin $S = 1/2$, which means that it can interact with unpaired electrons in magnetic materials. It provides in that respect an invaluable tool for exploring the distribution in orientation and amplitude of magnetic moments, static (magnetic structure) and dynamic (magnetic excitations).

2.2.1 Cross section

In a neutron scattering experiment, an incident neutron with wavelength $\overrightarrow{k_i}$, energy E_i and spin σ_i is sent towards the sample. According to its interaction with this target, it will emerge with wavelength $\overrightarrow{k_f}$, energy E_f and spin σ_f (see figure 2.8). The amount of momentum transfered to the sample by the neutron during its collision, the *momentum transfer*, is $\hbar\overrightarrow{Q} = \hbar(\overrightarrow{k_i} \quad \overrightarrow{k_f})$, where $\hbar = h/2\pi$ and $\overrightarrow{Q} = \overrightarrow{k_i} \quad \overrightarrow{k_f}$ is known as the *scattering vector*. The amount of energy transferred to the sample is $\hbar\omega = E_i \quad E_f = \hbar^2 k_i^2/2m \quad \hbar^2 k_f^2/2m$. The flux of neutrons detected within an infinitesimal solid angle $d\Omega$ along the unit vector $\vec{k}_f/k_f$ at a kinetic energy within an infinitesimal range dE_f around E_f normalised by the flux (hk_i/m) of the incoming neutrons defines the cross-section $d^2\sigma = (\partial^2\sigma/\partial\Omega\partial E_f)\ d\Omega\ dE_f$.

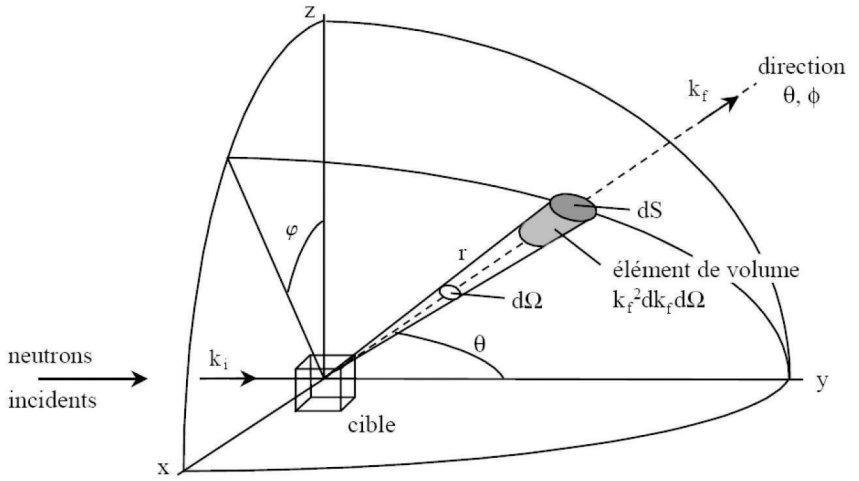

FIGURE 2.8: Schematic view of a neutron scattering. (from reference [14])

The partial differential cross-section is obtained from the Fermi's golden rule as

$$\left(\frac{\partial^2\sigma}{\partial\Omega\partial E_f}\right) = \frac{k_f}{k_i}\sum_{\lambda_i,\sigma_i,\lambda_f,\sigma_f} p_{\lambda_i}\ p_{\sigma_i}\ |f(\vec{k}_i\sigma_i,\vec{k}_f\sigma_f)|^2\ \delta(\hbar\omega + E_{\lambda_i} \quad E_{\lambda_f}) \qquad (2.10)$$

with average over the initial states $|\lambda_i>$ of the sample and the spin states $|\sigma_i>$ of the incoming neutrons and summation over all the final states $|\lambda_f>$ of the sample and the spin states $|\sigma_f>$ of the outgoing neutrons. The statistical weight p_{λ_i} depends on the sample. The statistical weight p_{σ_i} depends on the incoming neutron beam polarisation $\vec{P}_i : \sum_i |\ \sigma_i > p_{\sigma_i} < \sigma_i\ | = \frac{1}{2}(\mathbf{1}+\vec{P}_i\cdot\vec{\sigma})$, where the components of $\vec{\sigma}$ are the Pauli operators. If instead of the summation over all the spin states $|\sigma_f>$ of the outgoing neutrons one computes an average over their statistical ensemble then one obtains a cross section $\vec{P}_f(\partial^2\sigma/\partial\Omega\partial E_f)$, where $\vec{P}_f$ is the outgoing neutron beam polarisation, which can be experimentally measured as well. $f(\vec{k}_i\sigma_i,\vec{k}_f\sigma_f) = \frac{m}{2\pi\hbar^2} < \vec{k}_f\sigma_f\lambda_f\ |\mathrm{V}(\vec{r})|\ \vec{k}_i\sigma_i\lambda_i > = \frac{m}{2\pi\hbar^2} < \sigma_f\lambda_f\ |\mathcal{V}(\vec{Q})|\ \sigma_i\lambda_i >$ stands for the scattering amplitude, where $\mathrm{V}(\vec{r})$ is the interaction potential of the neutron with the sample and where $\mathcal{V}(\vec{Q}) = \int d\vec{r}\ \mathrm{V}(\vec{r})e^{i(\vec{Q})\cdot\vec{r}}$ is the Fourier transform of $\mathrm{V}(\vec{r})$.

The dominating contributions to $\mathrm{V}(\vec{r})$ are:

- The neutron-nuclei interaction potential, which, out of resonance is given by $\mathrm{V}_N(\vec{r}) = \frac{2\pi\hbar^2}{m}(b\ \mathbf{1} + B\ \vec{I}\cdot\vec{\sigma})\ \delta(\vec{r} \quad \vec{R})$ for a nucleon at position $\vec{R}$ with spin $\vec{I}$.

- The interaction potential of the neutron spin with the electron spin and orbital current densities $\vec{j}$ in the sample: $\mathrm{V}_M(\vec{r}) = g_n \frac{|e|\hbar}{2m}\ \vec{\sigma}\cdot\vec{B}(\vec{r})$, where $g_n = 1.91348$, $\frac{|e|\hbar}{2m} = 5.05095\ 10^{-27} JT^{-1}$ and $\vec{B}(\vec{r}) = (\frac{\mu_0}{4\pi})\int \frac{\vec{j}(\vec{s})\times(\vec{r}-\vec{s})}{|\vec{r}-\vec{s}|^3}\ d\vec{s}$.

which leads to

$$\mathcal{V}(\vec{Q},t) = \frac{2\pi\hbar^2}{m}\left\{\mathrm{N}(\vec{Q},t) + \vec{\mathrm{T}}(\vec{Q},t)\cdot\vec{\sigma} + \vec{\mathrm{M}}_\perp(\vec{Q},t)\cdot\vec{\sigma}\right\}$$

$\mathrm{N}(\vec{Q},t) = \sum_{\nu n} b_{\nu n}\ e^{i\vec{Q}.\vec{R}^o_{\nu n}(t)}$ and $\vec{\mathrm{T}}(\vec{Q},t) = \sum_{\nu n} B_{\nu n}\vec{I}_{\nu n}(t)\ e^{i\vec{Q}.\vec{R}_{\nu n}(t)}$ stand for the scattering from the nuclei and $\vec{\mathrm{M}}_\perp(\vec{Q},t)$ for the scattering from the unpaired electrons. The symbol $\perp$ means that only the component perpendicular to the scattering vector $\vec{Q}$ of the sample magnetisation distribution $\vec{\mathrm{M}}(\vec{Q},t)$ contributes to the scattering. $\vec{\mathrm{M}}_\perp(\vec{Q},t) = \sum_\nu f_\nu(\vec{Q})\sum_n \frac{1}{\vec{Q}^2}(\vec{Q}\times\vec{m}_{\nu n}(t)\times\vec{Q})\ e^{i\vec{Q}\cdot\vec{R}_{\nu n}(t)}$ for a collection of magnetic moments $\vec{m}_{\nu n}$, with $f_\nu(\vec{Q})$ designating a magnetic form factor characterising the spin and orbital current distribution about the position $\vec{R}_{\nu n}(t)$. In a crystal $\vec{R}_{\nu n}(t) = \vec{u}_\nu(t) + \vec{r}_\nu + \vec{R}_n$ where $\vec{u}_\nu(t)$ stands for the scatterer position at time t about a mean position $\vec{r}_\nu$ in the n-th unit cell at the position $\vec{R}_n$.

Injecting the interaction potential $\mathcal{V}(\vec{Q},t)$ into the equation (2.10), averaging over the incoming neutron spin states σ_i and summing over the outgoing neutron spin states σ_f, the partial differential cross-section can be finally written in the form [15, 16]

$$\begin{aligned}\partial^2\sigma/\partial\Omega\partial E_f =& < \mathrm{N}^\dagger(\vec{Q},0)\mathrm{N}(\vec{Q},t) >_\omega + < \vec{\mathrm{T}}^\dagger(\vec{Q},0)\cdot\vec{\mathrm{T}}(\vec{Q},t) >_\omega \\ &+ < \vec{\mathrm{M}}^\dagger_\perp(\vec{Q},0)\cdot\vec{\mathrm{M}}_\perp(\vec{Q},t) >_\omega + i\vec{P}_i\cdot < \vec{\mathrm{M}}^\dagger_\perp(\vec{Q},0)\times\vec{\mathrm{M}}_\perp(\vec{Q},t) >_\omega \\ &+ \vec{P}_i\cdot(< \mathrm{N}^\dagger(\vec{Q},0)\vec{\mathrm{M}}_\perp(\vec{Q},t) >_\omega + < \vec{\mathrm{M}}^\dagger_\perp(\vec{Q},0)\mathrm{N}(\vec{Q},t) >_\omega)\end{aligned} \tag{2.11}$$

using the compact notation $< \cdots >_\omega = (k_f/k_i)(1/(2\pi\hbar^2))\int_\infty^\infty < \cdots >_S\ e^{i\omega t}dt$ where $< \cdots >_S = \sum_\lambda p_\lambda \langle\lambda|\cdots|\lambda\rangle$ symbolizes the statistical average over the sample states. Although more tedious the polarisation of the outgoing neutron beam

can similarly be computed as [15, 16]

$$\begin{aligned}\vec{P}_f\ \partial^2\sigma/\partial\Omega\partial E_f = \vec{P}_i < \mathrm{N}^\dagger(\vec{Q},0)\mathrm{N}(\vec{Q},t) >_\omega \\ + < \vec{\mathrm{T}}^\dagger(\vec{Q},0)\cdot(\vec{P}_i\cdot\vec{\mathrm{T}}(\vec{Q},t)) >_\omega + < (\vec{P}_i\cdot\vec{\mathrm{T}}^\dagger(\vec{Q},0))\cdot\vec{\mathrm{T}}(\vec{Q},t) >_\omega \\ + \vec{P}_i\cdot < \vec{\mathrm{T}}^\dagger(\vec{Q},0)\cdot\vec{\mathrm{T}}(\vec{Q},t) >_\omega \\ + < \vec{\mathrm{M}}_\perp^\dagger(\vec{Q},0)\cdot(\vec{P}_i\cdot\vec{\mathrm{M}}_\perp(\vec{Q},t)) >_\omega + < (\vec{P}_i\cdot\vec{\mathrm{M}}_\perp^\dagger(\vec{Q},0))\cdot\vec{\mathrm{M}}_\perp(\vec{Q},t) >_\omega \\ + \vec{P}_i\cdot < \vec{\mathrm{M}}_\perp^\dagger(\vec{Q},0)\cdot\vec{\mathrm{M}}_\perp(\vec{Q},t) >_\omega \\ + i\vec{P}_i\wedge(< \vec{\mathrm{M}}_\perp^\dagger(\vec{Q},0)\cdot\vec{\mathrm{M}}_\perp(\vec{Q},t) >_\omega) \quad i < \vec{\mathrm{M}}_\perp^\dagger(\vec{Q},0)\times\vec{\mathrm{M}}_\perp(\vec{Q},t) >_\omega \\ + < \mathrm{N}^\dagger(\vec{Q},0)\vec{\mathrm{M}}_\perp(\vec{Q},t) >_\omega + < \vec{\mathrm{M}}_\perp^\dagger(\vec{Q},0)\mathrm{N}(\vec{Q},t) >_\omega\end{aligned} \tag{2.12}$$

It would be out of matter in this thesis to describe the variety of the signals which can experimentally contribute to the cross sections. I shall only qualitatively recall some general types of scattering. At zero energy transfer ($\hbar\omega = 0$) one has *elastic scattering*, which characterizes the infinite time correlation function. Among these one discerns the static correlations inherent to the crystal and magnetic structures that gives rise to intense peaks at specific points of the reciprocal space, that is *neutron diffraction*. As a matter of fact, these intense peaks correspond to the *coherent scattering* that arise from the interference of the neutron waves scattered from the average state of periodic arrangements of nuclei or of magnetic moments. Nuclei isotope distribution and nuclear random spin orientations out of this average are uncorrelated and give rise to *incoherent scattering*. This contributes to an isotropic background in the elastic scattering. Uncorrelated fluctuations of magnetic moments produce paramagnetic scattering that contributes to a signal that extends in the reciprocal space as the square of the magnetic form factors $f_\nu(\vec{Q})$. Another category of static correlations detected in elastic scattering are those associated to extended structural inhomogeneities and to short range magnetic order that give rise to scattering signals extended in reciprocal space, that is *diffuse scattering*. It is emphasized here that experimentally elastic scattering are measured within the energy resolution of the diffractometer and is thus integrated over that energy window, which partly involves dynamical correlations. Usual however the signal associated to these ones is much smaller than the static signals under interest. Note also that integration over all the energy transfer $\hbar\omega$ selects the equal time correlation functions. When dynamical correlations in the ground state have a short life time they produce a signal whose width is larger

than the instrument resolution, which is detected as a *quasielastic scattering*. In case of finite energy transfer ($\hbar\omega \neq 0$) beyond energy resolution one has *inelastic scattering*. When the dynamics are spatially correlated, typically as in the case of the collective excitations such as the phonons, the magnons, $\cdots$, the interference of the neutron waves again operate to produce *coherent scattering* with large signals.

In the following I describe the experimental method that was used to probe and identify the static magnetic correlations in the hypekagomé compound $Gd_3Ga_5O_{12}$.

2.2.2 Uniaxial polarisation analysis method

In a normal neutron scattering experiment, access to all contributions, nuclear or magnetic, is granted. Using an incoming polarized neutron beam, that is a beam made of neutrons with all spins in a same state σ_i parallel to a given direction, and analysis in polarization the outgoing neutron beam, that is measuring the statistical amount of neutrons in a spin state σ_f parallel to another given direction, specific scattering can be experimentally isolated, for instance nuclear coherent scattering, spin incoherent scattering, scattering from electronic magnetism, $\cdots$. In order to implement the suitable methodology and deal with the data the general formula of the cross section and of the outgoing polarization displayed in the equations (2.11) and (2.12) must be considered. The uniaxial polarization analysis method we concretely used was first proposed by Moon, Riste and Koelher [17]. It consists in collecting the scattering from a powder sample for a wide range of scattering vectors in the horizontal plane, by polarizing the incoming neutrons along (+) or oppositely ( ) to the vertical z-axis and analyzing the outgoing neutron polarization along (+) the same z-axis or oppositely to it ( ). It is then more transparent to consider the scattering amplitudes:

$$\begin{aligned} &< \sigma_f = \pm \,|\mathcal{V}(\vec{Q},t)|\, \sigma_i = \pm > \propto \mathrm{N}(Q,t) \pm \mathrm{T}^z(\vec{Q},t) \pm \mathrm{M}^z_\perp(\vec{Q},t) \\ &< \sigma_f = \pm \,|\mathcal{V}(\vec{Q},t)|\, \sigma_i = \mp > \propto \{\mathrm{T}^x(\vec{Q},t) \pm i\mathrm{T}^y(\vec{Q},t)\} + \{\mathrm{M}^x(\vec{Q},t) \pm i\mathrm{M}^y(\vec{Q},t)\} \end{aligned} \tag{2.13}$$

which tells that the non-spin-flip scattering, that is without spin reversal ($\pm\pm$), is sensitive to the nuclear scattering and those components of the nuclear spins and of the electronic magnetism which are parallel to the neutron spin whereas the spin-flip scattering, that is with spin reversal ($\pm\mp$), is sensitive only to those

components of the nuclear spin and of the electronic magnetism that are perpendicular to the neutron spin. The method isolates nuclear coherent scattering in the non-spin-flip channel and, owing to the average effect over the crystallite orientations in a powder sample, magnetic coherent scattering in the spin-flip channel. In principle there should also exist incoherent scattering from isotope distributions in the non-spin-flip channel and incoherent scattering from nuclear spin random orientations in the two channels, spin-flip as well as non-spin-flip. It turned out that these contributions were negligible. Owing to the strong absorption of cold and thermal neutrons by natural Gd, the sample of chemical formula $Gd_3Ga_5O_{12}$ was prepared at 99.98% purity with non absorbing isotope ^{160}Gd whose nuclear spin is zero ($I = 0$). Natural oxygen is composed of the ^{16}O isotope at 99.762% of natural abundance, whose nuclear spin is also zero ($I = 0$), and only a tiny amount of the isotopes ^{17}O with nuclear spin $I = 5/2$ and ^{18}O with nuclear spin $I = 0$. The only relevant contribution might have been expected from the use of natural Ga, which consists in a roughly 1/2 1/2 mixture of ^{69}Ga and ^{71}Ga isotopes each with nuclear spin $I = 3/2$, but the values of their spin-dependent scattering lengths ($b_+ = 6.3(2)$ fm and b $= 10.5(4)$ fm for ^{69}Ga and $b_+ = 5.5(6)$ fm and b $= 7.8(1)$ fm for ^{69}Ga) lead to weak contributions to the incoherent scattering. I shall finally emphasize that the method of uniaxial polarization analysis is well suited for the study of magnetism under strong magnetic field. Any other polarization setup where the neutron polarization would not be aligned along the strong applied magnetic field would lead to a depolarization of the neutron beams.

2.2.3 D7 diffractometer

D7 is a diffuse scattering spectrometer which uses polarized neutrons and allows to perform tri-axial XYZ polarization analysis. It is mainly used for the study of nuclear and magnetic short range ordered materials. We used it only in the uniaxial Z polarization analysis setup since we wanted to investigate the magnetization distribution in a $^{160}Gd_3Ga_5O_{12}$ powder sample under strong magnetic field. A monochromatic neutron beam is polarized to the z direction by a polarizer formed of a successive magnetic and non magnetic super mirrors (see figure 2.9). Then, a π *spin flipper* stage allows to flip the spins from $\uparrow$ to $\downarrow$ state. A small magnetic field (around 1 mT) maintains the polarization of the beam to the z axis. In the uniaxial Z polarization stetting a cryomagnet can be positioned around the sample to apply a magnetic field. In the tri-axial XYZ polarization analysis under zero

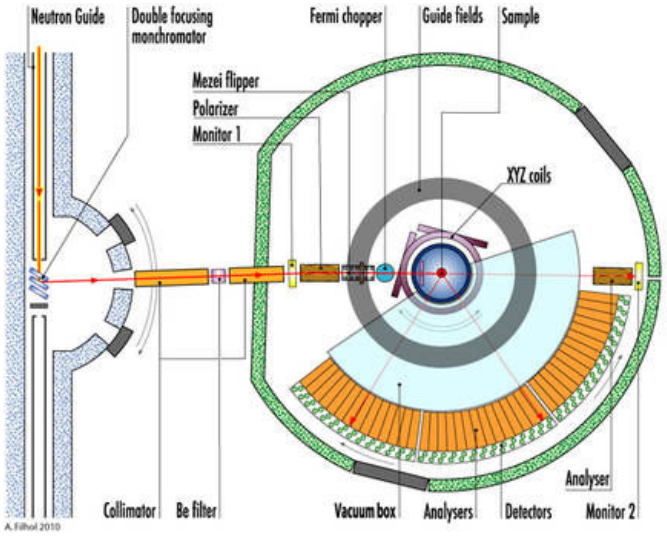

FIGURE 2.9: D7 polarized neutron spectrometer

magnetic field three orthogonal Helmholtz coils permits $\pi/2$ rotations from the z axis to the x and y axis. The magnetic field value is small enough not to alter the magnetization of the material. This design, allows the possibility to measure the spin flip and non spin flip cross sections for each of the three axes obtaining a complete mapping of the magnetic response. The scattered neutrons are collected with the use of a multi-detector which permits the polarization analysis of the scattered neutrons.

Frustration magnétique

Dans ce chapitre, j'introduis le concept de frustration magnétique, qui est l'objet des études que j'ai menées.

Je présente tout d'abord le cas de l'état verre de spins, induit par le désordre associé à une compétition d'interactions.

Je rentre ensuite plus en détail sur le cas de la frustration géométrique, induite par la topologie du réseau, qui est le cas qui nous intéresse plus particulièrement. J'introduis les réseaux frustrés à base de triangles et de tétraèdres, et la notion de liquide de spins, qui correspond à un état magnétique corrélé, mais dans lequel aucun ordre à longue portée ne s'établit.

J'aborde ensuite le cas des réseaux bidimensionnels triangulaires (triangles connectés par leurs côtés) et kagomé (triangles connectés par leurs sommets), et leurs propriétés dans le cas classique, en insistant sur le rôle de l'anisotropie du spin, et dans le cas quantique.

Enfin, je présente plus particulièrement le phénomène des plateaux d'aimantation prédits et observés dans les systèmes frustrés, comme signatures d'états magnétiques originaux. Cet effet est d'autant plus important pour nous qu'il peut être sondé avec le magnétomètre à force de Faraday présenté dans la première partie.

Chapter 3

Magnetic Frustration

3.1 Magnetic Frustration

Magnetic frustration is a subject of great interest since it induces the stabilization of unconventional magnetic states, different from the usual ferromagnetic and antiferromagnetic ordered states.

Although magnetic frustrated systems have been studied for a long time, the term *frustration* was first introduced in physics by Toulouse in 1977 [18] in connection to spin glasses. He called a system as frustrated if it cannot simultaneously minimize all of its spin-spin interactions. In canonical spin-glasses, where magnetic impurities are randomly diluted in a non magnetic lattice, this frustration arises due to the competition between magnetic interactions of different sign and size.

In the absence of disorder, the competition of interactions can also lead to frustration. A simple example to describe this behavior is presented schematically in figure 3.1. In such cubic lattice, an antiferromagnetic interaction between near neighbor atoms is fully minimized on all pairs by the antiparallel arrangement of the atomic moments. However, if next to nearest neighbor interaction is antiferromagnetic as well, frustration results due to competing interactions, J_1 and J_2. This model, called J_1-J_2 model, has been extensively studied since 1980 and is now understood to present different magnetic phases according to the value of the ratio J_2/J_1. For example, on the square lattice, Chandra and Douçot showed in 1988 [19] the existence of a spin liquid at zero temperature for $J_2/J_1 \sim 0.5$.

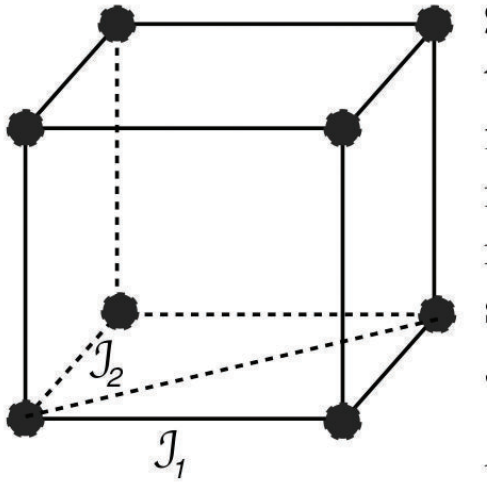

FIGURE 3.1: Frustration due to competing interactions: cubic lattice with antiferromagnetic J_1 and J_2 interactions.

However, experimentally it is difficult to find a material for which J_2/J_1 is in the appropriate ratio to induce such new behavior.

To the competing interactions described above, we can add a second case of frustrated systems, in which frustration arises from the structural arrangements of the spins. A typical example to illustrate this behavior, called *geometrical frustration*, is a triangle with Ising spins ($\uparrow$ or $\downarrow$) on its corners, which interacts via antiferromagnetic interactions (see figure 3.2). It is easy to see that if the first two spins are aligned antiparallel to each other, the third spin can point either antiparallel with the first or the second but not with both at the same time. In this case, the geometry of the lattice generates two equivalent degenerate energy states for the lowest energy, thus creating a degenerate ground state. By joining triangles to form a lattice, the degeneracy grows exponentially with the number of spins, N, leading in the thermodynamic limit, $N \to \infty$, to a macroscopic entropy and to a whole manifold of equal energy ground states.

Nowadays, we understand the physics of frustration as the physics of the macroscopic degeneracy of magnetic systems. However, macroscopic degeneracy can be found in non magnetic materials as well. Historically, the first case of macroscopic degeneracy was found out in a nonmagnetic system, the water ice. In 1933, Giauque et al. showed the existence of a residual entropy in water ice, that would persist down to the lowest temperatures [20]. The explanation for the odd behavior is presented in the work of Pauling et al. in 1935 [21]. His interpretation lies

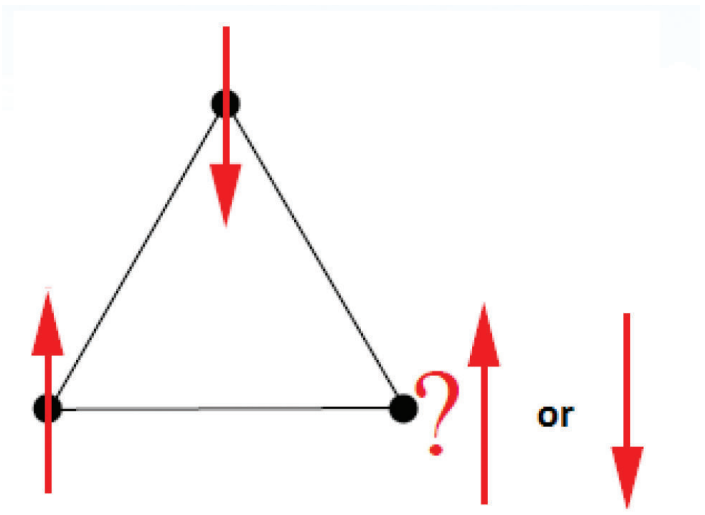

FIGURE 3.2: Principle of the geometrically magnetic frustration: Ising spins (↑ or ↓) on a triangular lattice with antiferromagnetic interactions. Once two spins align antiparallel to each other, the third one can not be simultaneously antiparallel to both spins which leads to frustration.

in the disorder of the hydrogen atoms in the crystal structure of the bonded water molecules. Specifically, for each oxygen atom, two hydrogen atoms are located

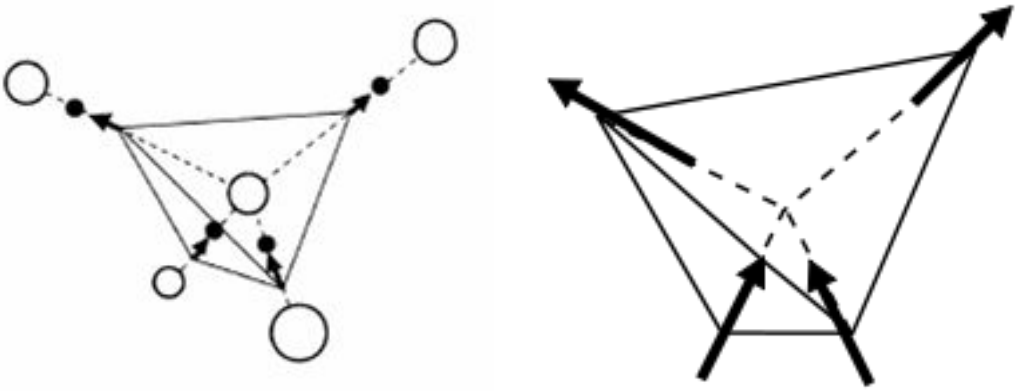

FIGURE 3.3: Left: arrangements of hydrogen (black circles) and oxygen (open circles) atoms in the tethragonal water ice structure. Right: arrangements of magnetic spins in a spin ice material.

close to and two far from it, according to the *ice rules* predicted by Bernarl-Fowler [22] (see figure 3.3 left). The macroscopic degeneracy of the ground state which arises from the ice rule leads to a residual entropy which persists down to lowest temperatures. Regardless of the non magnetic state of water ice, an analogy with the crystallographic structure and the ice rules permitted for example to explain the non zero entropy in a category of geometrically frustrated systems, called spin

ices [23]. In such compounds, the spins are arranged on the corners of a tetrahedra and they obey the *two in - two out* (ice rules) configuration (see figure 3.3 right). Therefore, they exhibit the same residual entropy properties as water ice [24].

I will first briefly present the concept of spin glasses. Then I will focus on geometric frustration, and especially on the case of the triangular and kagome lattices, which are related to the compounds I have studied.

3.2 Spin Glasses

The concept of spin-glass is often evoked in the literature, especially in frustrated magnetism, when hysteretic or frequency dependence are observed in the magnetic properties. For this reason, in this section, I present the main ingredients of a spin-glass state and some experimental features characteristic of spin-glasses. This is not an exhaustive presentation, and to go further, several great reviews exist on the subject, such as the work of Binder et al [25].

Spin glasses are magnetic systems in which the interactions between the magnetic moments are frustrated due to some frozen-in structural disorder. Thus no conventional long-range order (ferromagnetic or antiferromagnetic) can be established. However, these systems exhibit a "freezing transition" to a state with a new kind of "order" in which the spins are aligned in random directions. At temperatures below the freezing temperature, T_f, the magnetic moments are frozen into a disordered state, but they do not pick any direction. The magnetic state can then be described with the spin glass order parameter $q = [\langle S_i \rangle_T^2]$

The first examples of spin glasses are called "canonical spin-glasses. They are made of noble metals (Au, Ag, Cu, Pt) weakly diluted with transition metal ions. In canonical spin glasses, the spins interact through conduction electrons which lead to an indirect exchange interaction, $J(r)$, called RKKY interaction (Ruderman-Kittel-Kasuya-Yosida)[26–28]. This interaction oscillates strongly with distance r

$$J(r) = J_0 \frac{cos(2rk_F + \phi_0)}{(rk_F)^3} \tag{3.1}$$

where J_0 and ϕ_0 are constants, and k_F is the Fermi wave number of the noble metal. Since the distances between the spins are random, for a given spin, some of its interactions with other spins will be positive, favoring antiparallel alignment,

and some will be negative, favoring parallel alignment. Thus no spin alignment can be found that is satisfactory to all exchange bonds. From equation (3.1) and figure 3.4, we can observe that the interactions are long-range and decay with $1/r^3$. The effect of the RKKY interactions is the existence of a large number of states of low energy with the same macroscopic properties but with different microscopic configurations separated by high free-energy barriers in phase space (see figure 3.4 right). Therefore, disorder and frustration are the ingredients we are looking at in

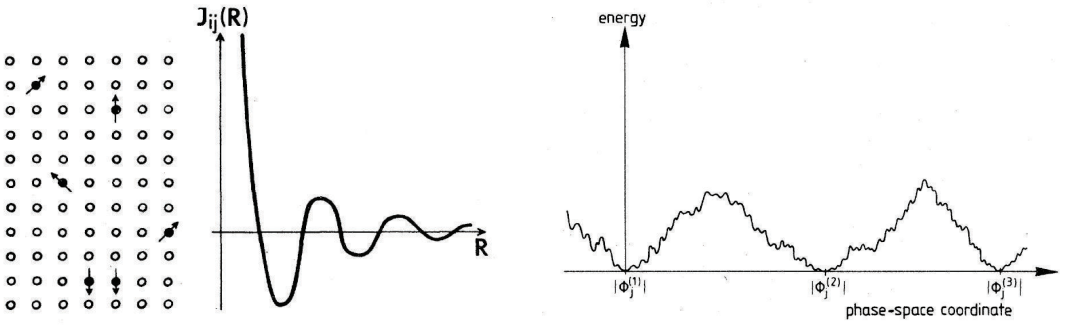

FIGURE 3.4: Left: Schematic sketch of magnetic moments randomly diluted in a metallic matrix, and the resulting RKKY exchange integral plotted as a function of distance. Right: Degenerate thermodynamic states with the same macroscopic properties but with different microscopic configurations separated by "infinite" energy barriers in the phase space. (from reference [25])

spin glass materials.

When a magnetic field is applied, the random interactions freeze the spins in random directions, while the magnetic field tends to align them parallel to the field. This leads to hysteretic behavior in the magnetization curves. In fact, strong enough magnetic fields can destroy the spin glass state.

An experimental signature of the spin glass state can be found in the frequency-dependent susceptibility. For example, V. Cannella and J. A. Mydosh observed a sharp "cusp" in the frequency-dependent susceptibility in low fields in gold-iron alloys [29], which later became one of the signatures of spin glasses. Other features are the hysteresis in zero field cooled - field cooled (ZFC-FC) processes and the non-linear behavior of the susceptibility near the freezing temperature. While hysteresis in the ZFC-FC measurements or a frequency-dependent susceptibility are the signatures of spin freezing, one needs to pay attention as the spin glass state is much more subtle than that.

As an example, there are two relations which are used to describe the frequency dependence of the χ' maximum for canonical spin glasses. The first is the Vogel-Fulcher law $\tau = \tau_0 \exp[E/(T \quad T_0)]$, where E is an energy barrier, T_0 is a phenomenological parameter, τ_0 is the intrinsic relaxation time, and τ is related to the measurement frequency: $\tau = 1/(2\pi f)$. A second approach is the dynamical scaling near the transition T_f, $\tau = \tau_0[T/(T \quad T_f)]^{z\nu}$, where z is the dynamic exponent and ν is the critical exponent associated to the correlation length. Several reviews on spin glass materials display the importance of a detailed study of the relaxation time in magnetic materials before confirming the spin glass state [25, 30]. Souletie and Tholence showed in their work [30] that the Vogel-Fulcher law is suitable phenomenologically, while the dynamical scaling is more appropriated in the case of a phase transition, and allows to describe the dynamics in the whole frequency range.

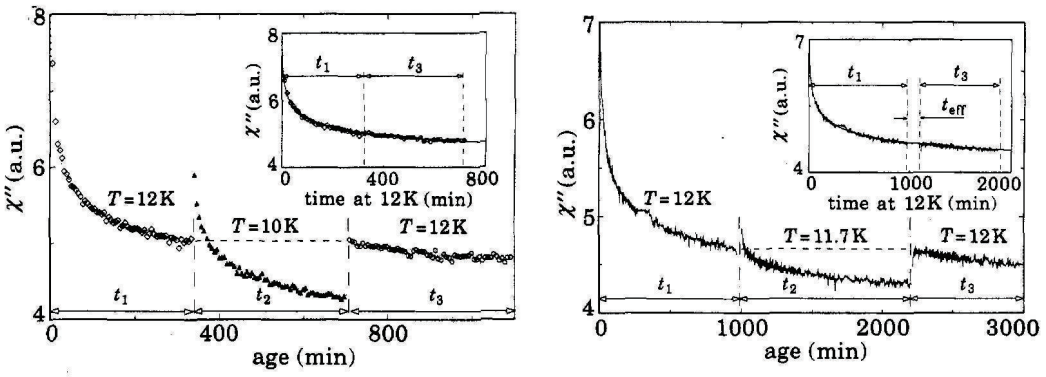

FIGURE 3.5: Rejuvenation and memory effect in $CdCr_{1.7}In_{0.3}S_4$ (from reference [31])

Another spectacular phenomena observed in spin glass materials is "*aging*", which means that the magnetic response depends on the time spent after quenching the system below the freezing temperature. Temperature cycling experiments also evidenced *rejuvenation and memory* effects (see figure 3.5). If the system is quenched and let to evolve at a temperature $T_1 < T_f$, and then it is cooled at a temperature $T_2 < T_1$, instead of a slowing-down of the relaxation, it restarts the relaxation with the same initial response, which is called the *rejuvenation* effect. If, after this experience, the temperature returns to T_1, the relaxation starts again from the point where the temperature had changed, which is called the memory effect.

Recent work in spin glass materials has focused on the nature of the glassy magnetic state in the absence of disorder [32, 33]. The main question is to know whether such systems can present a *topological spin-glass* state. Several systems have been proposed, in particular the hydronium jarosite kagome system and the pyrochlore compound $Y_2Mo_2O_7$ [34–36]. While the second one presents rejuvenation and memory effects, this is not the case of the first one. A great difficulty in this search for a topological spin-glass state is that it is hard experimentally to identify if these effects are due to site-disorder or not, i.e. induced for example by defects in the structure.

3.3 Geometric frustration

Geometric frustration occurs when the frustration arises due to topology of the system. The most known geometrically frustrated systems have lattices based on triangles or tetrahedra. The magnetic properties associated with these lattices of spins greatly depends on their connectivity, that is the way the triangles or tetrahedra are connected. If we connect them via their edges, we create triangular and face-centered cubic structures for triangles and tetrahedra respectively (figure 3.6 (a) and (c)). In the case of triangles or tetrahedra connected via their corners,

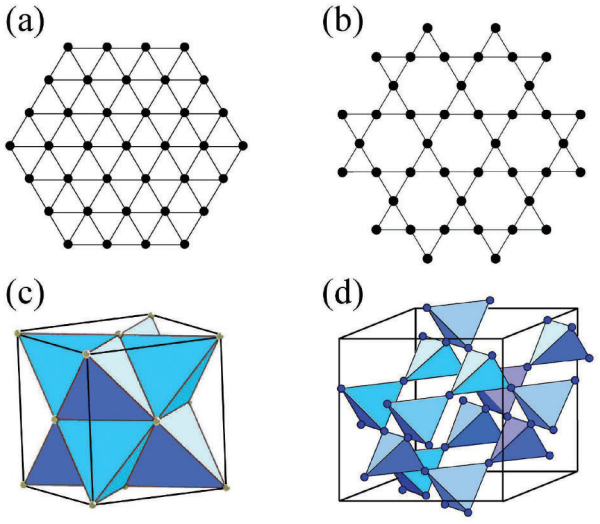

FIGURE 3.6: Geometrically frustrated lattices: a) triangular b) kagome, c) face-centered cubic d) pyrochlore

one can get the kagome and the pyrochlore lattices, respectively (see figure 3.6 (b) and (d)) which are the focus of many studies nowadays.

A signature of geometric frustration is the macroscopic degeneracy of the ground state found in these systems. It leads to the discovery of novel magnetic states like the spin liquid state. We call a *spin liquid* state a state for which no long range order is found down to 0 K, but where short-range correlations are present.
From a classical point of view, it can be understood as a disordered state, characterized by a degeneracy of low energy states. It is best understood in the case of the weather vane mode of Heisenberg spins on the kagome lattice described below (see paragraph 3.3.2).
In the case of quantum spin liquids, the ground state is a superposition of quantum states. Quantum spin liquids can be classified into two parts depending on the emergent excitations. *Topological spin liquids* have a linear superposition of all possible singlet configurations, called the Resonant Valence Bond (RVB) state, schematically presented in figure 3.7. Its ground state is two fold degenerate sepa-

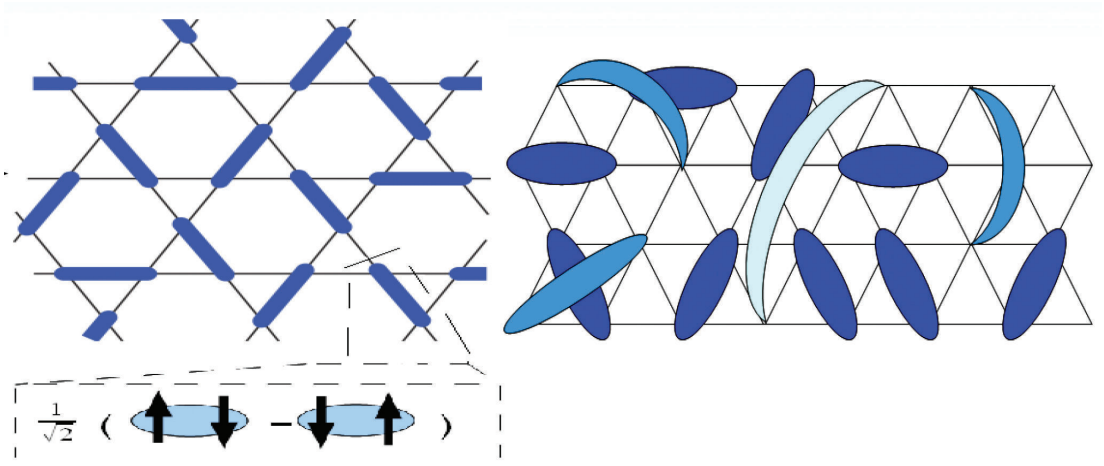

FIGURE 3.7: Schematic view of a resonance valence bond (RVB) spin liquid state.

rated from the first excited state (triplet) by a gap. *Algebraic spin liquids* display a continuum excitation spectrum, therefore no gap is present in such materials. Nowadays, researchers around the world are looking for spin liquid materials and the first question that arises is whether they are gapless or not.

The development of new techniques in material science allows nowadays to prepare materials with a whole variety of crystallographic structures. Therefore, to find novel exotic magnetic states in frustrated systems, it is important to look in which lattices the arrangements of the spins and the corresponding interactions between them can lead to a macroscopic degenerate magnetic ground state.

In the following, I will present some results on two two-dimensional triangle based lattices: the triangular lattice and the kagome lattice. In the classical picture, if the spins can orient only into a single direction, then we will consider we have *Ising spins* and if this single direction changes from site to site, we will say we have *multi-axial Ising spins*. *XY spins* have a certain plan in which they are free to rotate. *Heisenberg spins* are free to rotate in any direction of the 3D space.

3.3.1 Triangular lattice

First let's take for example the triangular lattice and the case of Ising spins. In the case of ferromagnetic interactions, the interactions are satisfied and no degeneracy is expected. As described in paragraph 3.1, antiferromagnetic interactions lead to a macroscopic degeneracy (see figure 3.8 for the 6 possible ground states of a triangle. The mapping of the triangular lattice is a combination of these states). Materials which exhibit such structure have been intensively studied since the beginning of research in the magnetic frustration field. In fact, in 1950 Wannier calculated the entropy for such a system at a value of $S \simeq 0.33$ [37]. If we allow the spin to rotate

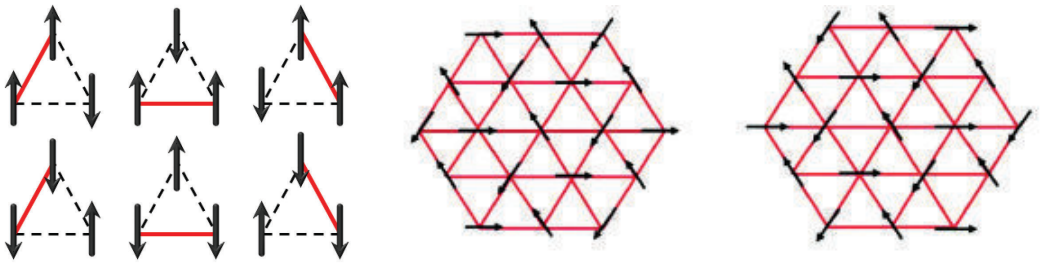

FIGURE 3.8: Influence of the spin dimensionality. Left: ground states of the antiferromagnetic uniaxial Ising spin on triangular lattice. Right: 2 possible configurations for the multiaxial AF Ising spins on triangular lattice.

in the triangular plane (XY spins), then antiferromagnetic interactions will favor a triangular configuration of the spins in any given triangle (120^0 configuration). On the triangular lattice, the initial triangle shares two spins with each of the neighbor triangles. The orientation of the third spin in each given triangle is then fixed by the interactions to form the 120^0 spin configurations. Keeping the same reasoning, the mapping of the lattice is made step by step by the choice of the first triangle. Even if there is a continuous degeneracy due to global rotations of the spins, the system has just two states of the lowest energy. They are associated

with the two 120^0 spin configurations of opposite chiralities for the initial chosen triangle, thus it shows no macroscopic degeneracy.

An interesting case is the triangular lattice with multiaxial Ising spins in a 120^0 configurations with ferromagnetic interactions. It can be shown that the problem maps exactly as the triangular lattice of uniaxial Ising spins, but with antiferromagnetic interactions. This case was already shown to be degenerated by Wannier.

If the spins are Heisenberg, ferromagnetic as well as antiferromagnetic interactions stabilize a single configuration, ferromagnetic and triangular respectively. As we can see, the nature of the spins anisotropy can lead to different macroscopic magnetic properties even if the materials have the same lattice and interactions.

We observe that depending on the degree of freedom of the spins (Ising, multiaxial Ising, XY or Heisenberg) and the interactions between the spins, macroscopic degeneracy might arise or not.

In the quantum case, the antiferromagnetic triangular lattice has been shown to order antiferromagnetically at $T = 0$.

3.3.2 Kagome lattice

In the case of the kagome lattice, triangles connected by their corners, the geometry leads to frustration for both Heisenberg and XY antiferromagnetic spins. The reason for macroscopic degeneracy is schematically presented in figure 3.9 for XY spins. As mentioned before, antiferromagnetic interactions between the spins will

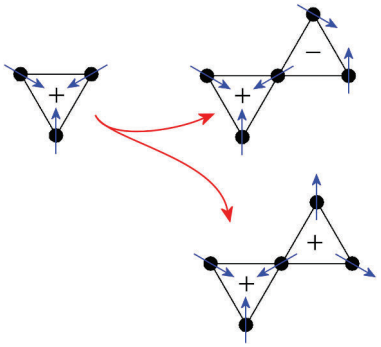

FIGURE 3.9: Influence of the spin dimensionality. Two possible configurations for the XY spins on kagome lattice.

favor a 120^0 spin configuration. Starting from a triangle, the system has two possible states for the second triangle, so that the degeneracy increases exponentially with the number of triangles. In the case of Heisenberg spins, they can move out-

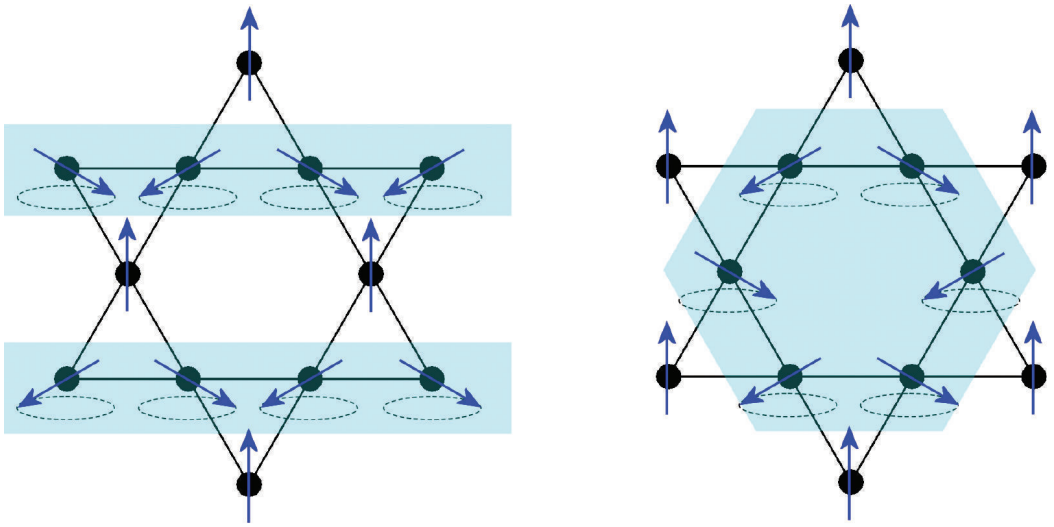

FIGURE 3.10: AF Heisenberg spins: weather vane modes for q = 0 (left) and q = $\sqrt{3}$ x $\sqrt{3}$ (right)

side of the plane but it has to remain in the 120^0 configuration which minimizes the energy on one triangle. Therefore, two spins can rotate continuously with respect to the axis of the third spin without energy cost which leads to infinite degeneracy and no long range order is expected down to 0 K.

At very low temperatures ($T < 5.10^3 J$), thermal fluctuations select states with the highest density of low energy excitations by a process called *order by disorder* [38–40]. Coplanar states are selected by this entropic process, but no long range order is achieved. Two of these coplanar states are the q = 0 and $\sqrt{3}$ x $\sqrt{3}$ states. Spins can fluctuate from these states with zero exchange energy cost through the weather vane modes shown in figure 3.10.

Experimentally, few classical kagome lattices are synthesized. A rich family is the Jarosites family, $AM_3(SO_4)_2(OH)_6$, where A is an alkaline ion and M is a transition metal. Different magnetic states have been observed: long-range order [41, 42], but in addition, a flat mode at finite energy was evidenced in the K jarosite, suggesting a lifted weather vane like mode [43]; spin-liquid correlations followed by a spin glass transition [44, 45]. These results have emphasized that any perturbation to the Heisenberg hamiltonian (Dzyaloshinskii-Moriya interactions, anisotropy, second neighbor interactions) destabilizes the spin-liquid ground state.

The quantum kagome antiferromagnet remains in a spin liquid state down to zero temperature. Nevertheless, the nature of this spin liquid, and the presence or not of a gap in the excitation spectrum, are a great subject of debate. The main difficulty is that it is not possible to solve exactly the Hamiltonian of this system. Many theoretical approaches have been used to tackle this problem: exact diagonalization on a finite number of spins, DMRG calculation, tensor networks... Exact diagonalization calculations show that a very high density of low energy singlet states exist in the kagome spectrum, but the question is do these low energy states form a continuum when the system size goes to infinity. Today, although the nature of the ground state is still debated, calculations seem to indicate a gapped spin liquid (see for example [46–48]).

There are also very few experimental realizations of materials which exhibit kagome structures with quantum spins, which makes difficult the comparison with calculations. In addition, it is expected that the ground state in the kagome materials will be strongly affected by additional terms in the Hamiltonian (second neighbor interactions, disorder...). Herbertsmithite, $ZnCu_3(OH)_6Cl_2$, is one of the most promising candidates for an ideal quantum kagome antiferromagnet. In this compound, copper spins ($s = 1/2$) are expected to lie in a kagome a b plane well separated by diamagnetic Zn^{2+}. It presents a spin-liquid state down to very low temperature, with a lack of ordering down to about $J/10^4$ [49]. Excitations form a continuum [50], and if a gap exists, it should be smaller than $J/200$ [51]. Nevertheless, it is not a perfect kagome quantum antiferromagnet system since Dzyaloshinskii-Moriya (DM) interactions as well as site disorder (exchange of Zn and Cu ions) have to be taken in consideration to explain the experimental data [52, 53].

3.4 Magnetization plateaus

A spectacular phenomenon observed in frustrated materials which exhibit triangular and kagome structures, is the presence of plateaus in the magnetization measurements as a function of the applied magnetic field (see for example reference [54]).

If we consider Heisenberg classical spins on a triangle, when a magnetic field, small compared to the antiferromagnetic interaction J, is applied, one spin on a

triangle orientates parallel to the field while the two other spins remain in the 120^0 configuration. At the critical field $H_c = 2J$, spins flip: two are parallel to the field, while the other one is antiparallel, resulting in a magnetization plateau with a magnetization value equal to one third of the saturated magnetization. At $H_{sat} = 6J$, the third spin also becomes parallel to the field, and the magnetization finally saturates. Note that in that case, the plateau is stabilized by thermal fluctuations. The existence of such plateau is also predicted for the kagome lattice, but its size is expected to be reduced.

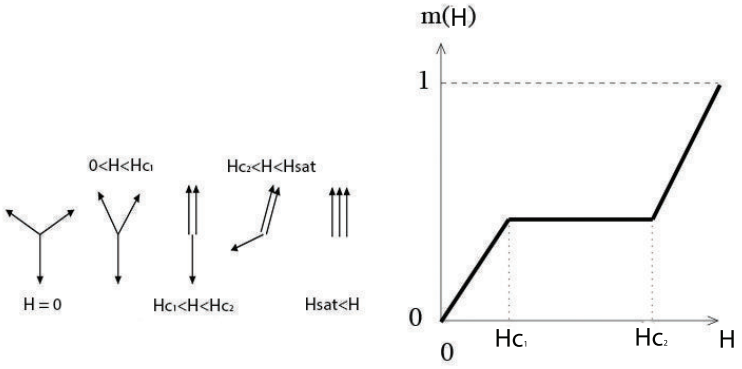

FIGURE 3.11: The orientation of the three spins as a function of applied magnetic field and the corresponding magnetization plateau (from reference [54]).

In the case of quantum spins, 1/3 magnetization plateaus are also predicted both in the triangular and the kagome antiferromagnets [40, 55]. They also correspond to "up-up-down" collinear states, and are favored by quantum fluctuations. Nevertheless, in the kagome antiferromagnet, the magnetic state on the plateau remains a spin-liquid state, rather than an ordered collinear spin configuration as in the triangular case.

It is not uncommon to find a magnetization plateau in materials which exhibit triangular lattices, as shown for example in figure 3.12 left for $RbFe(MoO_4)_2$ [56]. But there are very few observed in kagome compounds. One example is $[Cu_3(titmb)_2(OCOCH_3)_6]\cdot H_2O$, presented in figure 3.12 right [57], but it is only a transient plateau, and this compound was shown not to be a perfect kagome antiferromagnet.

In more complex cases, magnetization plateaus can occur at other values of the magnetization. In addition, the detailed study of the magnetization curves shape can also provide information on the nature of the excitations associated with the

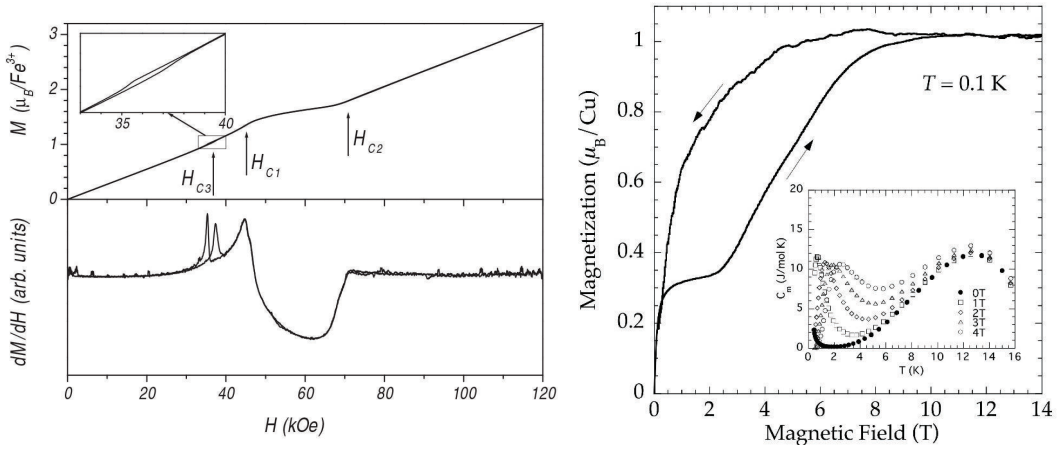

FIGURE 3.12: Left: 1/3 magnetization plateau in triangular structure material, $RbFe(MoO_4)_2$ (from reference [56]). Right: 1/3 magnetization plateau in kagome structure material, $[Cu_3(titmb)_2(OCOCH_3)_6]\cdot H_2O$ (from reference [57]).

plateau phase. Therefore, measuring precisely magnetization curves and the value of the magnetization plateaus can give access to the exotic magnetic states of such frustrated quantum systems.

During my PhD I studied several frustrated materials. In the first part I will present two classical magnetic spin materials, $Gd_3Ga_5O_{12}$ and $Gd_3Al_5O_{12}$ which present a hyperkagome structure, a 3D kagome lattice. These systems show a complex phase diagram with respect to temperature and external applied magnetic field which can be probed by means of magnetic and neutron scattering measurements.

In the second part I will present the results for two quantum molecular magnets: one with tetrahedron lattice and a second one with a triangular lattice. In these cases, the excitation spectrum of the molecules and the possible imprint of frustration in it can be looked at through Zeeman crossing.

Gadolinium Gallium Garnet

Dans ce chapitre, je présente l'étude que nous avons menée sur le système Gadolinium Gallium Garnet, formule $Gd_3Ga_5O_{12}$, dit GGG, en collaboration avec Pascale P. Deen (ESS Lund, Suède).

Je présente tout d'abord le contexte de l'étude: GGG est un composé très étudié depuis plusieurs décennies, présenté comme l'archétype du système frustré de spins classiques, et dans lequel s'établit un état liquide de spins jusque très basse température (au moins 25 mK). Les atomes des Gadolinium magnétiques sont situés sur deux réseaux hyper kagomé (= réseaux de triangles en trois dimensions connectés par leur sommets) interpénétrés. Il a été montré que plusieurs interactions doivent être prises en compte dans ce système, au-delà des interactions premiers voisins, et notamment les interactions dipolaires à longue portée. Ceci complique fortement la description théorique du système.

Expérimentalement, nous nous sommes essentiellement intéressés au diagramme de phase sous champ magnétique. Il avait en effet été montré que plusieurs phases de nature différente coexistent sous champ magnétique: ferromagnétique, antiferromagnétiques et incommensurables. Des excitations non conventionnelles ont également été rapportées.

Nous avons mené des mesures systématiques d'aimantation en fonction du champ magnétique et de la température sur deux échantillons, un monocristal et une poudre isotopique. Nous avons associé cette étude à des mesures de diffusion de neutrons polarisés sous champ magnétique sur la même poudre isotopique.

La combinaison de ces deux techniques nous a permis d'établir un diagramme de phase de GGG plus précis que ce qui avait été proposé jusqu'à présent. En particulier, nous avons pu mettre en évidence un nouvel effet, autour de 0.9 T: une anomalie dans les courbes d'aimantation en fonction du champ, associée à une

réentrance de l'irréversibilité Zero Field Cooled - Field Cooled dans les courbes d'aimantation en fonction de la température. De plus, l'ensemble des lignes du diagramme de phase semble converger vers le point 0.9 T - 300 mK, qui pourrait donc être un point spécifique pour ce système.

Chapter 4

Gadolinium Gallium Garnet

4.1 Introduction

In section 3.3 I showed that infinite degeneracy is expected in a kagome lattice with Heisenberg spins which interacts through antiferromagnetic interactions. The hyperkagome lattice is a lattice based on triangles connected via their corners, like the kagome lattice, but in three dimensions. Therefore a degeneracy is expected in such a lattice with what we think to be, Heisenberg spins. On top, secondary interactions can lead to the development of new and unexpected phases.

In the family of gallium garnets, the rare-earth elements lie on such hyperkagome lattice, but there are two interpenetrating hyperkagome lattices (see figure 4.1). Contrary to isomorphous gallium garnets based on Nd, Sm or Er, which exhibit a transition to an ordered state [58], no long range order is seen in GGG down to lowest temperatures [59] despite a Curie-Weiss temperature, $\theta \sim$ - 2 K. In comparison to the other rare earth garnets it could be that the isotropic Gd spin ($S = 7/2$, $L = 0$) could be the origin of the lack of order. The spins are considered Heisenberg due to single-ion anisotropy of less than 0.04 K [60].

Note that the quantum counterpart of GGG can be found in $Na_4Ir_3O_8$, in which Ir^{4+} ions lie on a hyperkagome lattice. While GGG appears as the realization of a Heisenberg spin-liquid, $Na_4Ir_3O_8$ is proposed to be a quantum spin-liquid due to the spin, $s = 1/2$, of the Ir ion [61–63].

GGG has been studied for a few decades now, but the complicated low temperature behavior is still not fully understood. In GGG (space group $Ia\bar{3}d$), the magnetic

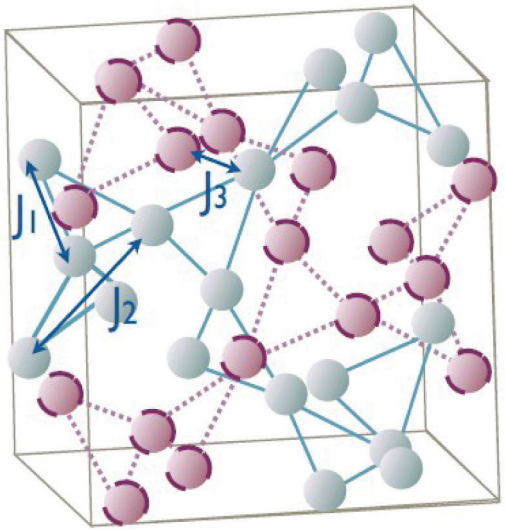

FIGURE 4.1: GGG: Gd s=7/2 isomorphic spins on two interpenetrating corner sharing triangles in a 3D lattices (hyperkagome lattice); J_1, J_2 and J_3 exchange interactions are highlighted.

moments are placed on two inter-penetrating corner sharing triangular lattices (hyperkagome lattice). First (J_1) and second (J_2) nearest neighbor interactions are present inside a given sublattice. The third (J_3) neighbor interaction couples the two sublattices. Therefore, first, second and third nearest neighbor interactions needs to be taken into account to understand the magnetic properties of GGG. The Hamiltonian for GGG can be written as

$$\mathcal{H} = \sum_{i,j} J_{i,j} \vec{S}_i \vec{S}_j + D \sum_{i,j} \left[\frac{\vec{S}_i . \vec{S}_j}{r_{i,j}^3} \quad 3 \frac{(\vec{S}_i . \vec{r}_{ij})(\vec{S}_j . \vec{r}_{ij})}{r_{ij}^5} \right] \tag{4.1}$$

with classical spins, $S_{i,j}$. The first and second term are the exchange, and the dipole-dipole interaction between the magnetic moments respectively. In 1979, Kinney and Wolf, performed Monte Carlo simulations on 8 cubic unit cells and confronted their results with specific heat measurements to extract the exchange interactions present in the system [64]. According to them, the exchange interactions are: $J_1 \sim$ - 0.1 K whereas J_2 and J_3 are $\sim J_1/100$, to compare with the dipole-dipole interaction, $D = 0.045$ K. All these ingredients, makes this system interesting for the study of 3D highly frustrated compounds.

4.2 State of the Art

Early specific heat measurements showed a broad maxima around 0.8 K [64] suggesting the existence of short range correlations. The first magnetic low temperature study was performed soon after, in 1980 by Hov et al. [59]. They observed a field induced antiferromagnetic phase below 0.4 K. Despite the expected isotropic behavior due to the singlet-orbital ground state nature of the Gd ion, a slight shift is seen between the field induced phase for the [100] and [111] crystallographic directions (see figure 4.2).

It took 15 more years to have the first detailed study on the low temperature

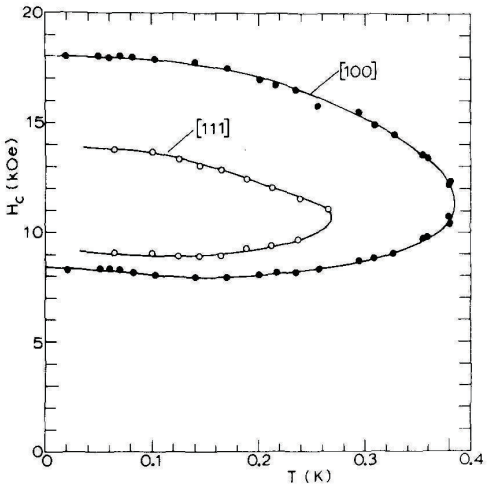

FIGURE 4.2: H-T phase diagram of GGG (H || [100] and [111] - from reference [59]).

behavior. In 1994, Schiffer et al. complemented the H-T phase diagram (see figure 4.3) and proposed that the GGG ground state is a spin glass state. [65, 66]

However, the first neutron scattering performed by Petrenko et al [67] disagreed with a spin glass ground state (see figure 4.3). At 45 mK and in the absence of magnetic field, a coexistence of short range and long range order (the correlations are not resolution limited) is observed. From their calculation, 85 % of spins are in a somehow "liquid" state. Under applied magnetic field, neutron scattering showed that the field induced antiferromagnetic phase is much more complicated than believed before. Antiferromagnetic, ferromagnetic and incommensurate magnetic peaks are present in the neutron scattering profile (see figure 4.4 left) [68]. Further muon spin relaxation measurements on GGG, showed that in terms of spin relaxation, the system remains in a partially dynamic state down to 25 mK [69], while Mossbauer measurements suggested planar spin fluctuations [70]. .

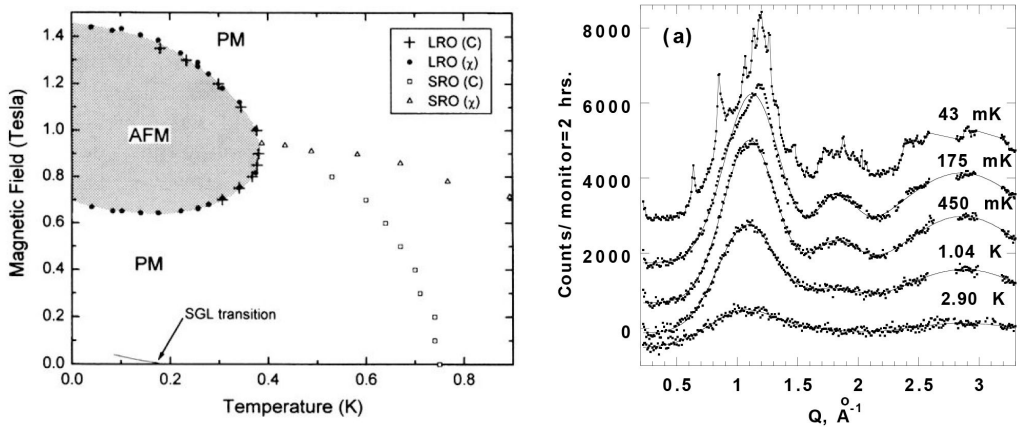

FIGURE 4.3: Left: H-T phase diagram of GGG (H || [100] from reference [1]). Right: first neutron scattering on ^{160}Gd isotope powder (from reference [67]).

In 2006, Yavors'kii et al. demonstrated that dipolar interactions play an important role in GGG [71]. Their investigation in zero magnetic field using mean-field theory showed that the system is sensitive to dipolar interactions. The spin couplings in the Hamiltonian ($H = H_e + H_{dip}$) include dipolar interactions H_{dip} of strength D, cut-off at a distance R_c. The neutron scattering results, sharp peaks on top of broad features characteristic of short-range correlations could only be reproduced by taking into account dipolar interactions with an appropriate $R_c = \infty$. Most importantly, they identified the reciprocal plane that contains the ordering wave vector, $q_{ord} \sim 2\pi/a$ [0.29, 0.29, 0].

In 2010, our collaborators P. P. Deen et al. studied the excitation in powdered GGG through inelastic neutron scattering measurements [72]. Three gapped inelastic peaks are presented in figure 4.4 right, despite an expected continuum of gapless excitations. These excitations can not be assigned to acoustic modes. The possibility of optical and soft modes was proposed. A recent detailed study in the high magnetic field region ($H > 1.8$ T [74]) showed that the spins are not fully aligned in this region, due to the dipolar interaction.

Our study complements the low temperature magnetization study by providing additional data with the applied magnetic field along the [110] crystallographic direction. The above mentioned papers showed different results between neutron scattering and magnetic measurements. For this reason, we performed magnetic measurements and neutron scattering on the same ^{160}Gd isotope GGG powder. By correlating measurements on a powder (neutron scattering and magnetic measurements) and single crystal (magnetic measurements - non-isotope enriched), an

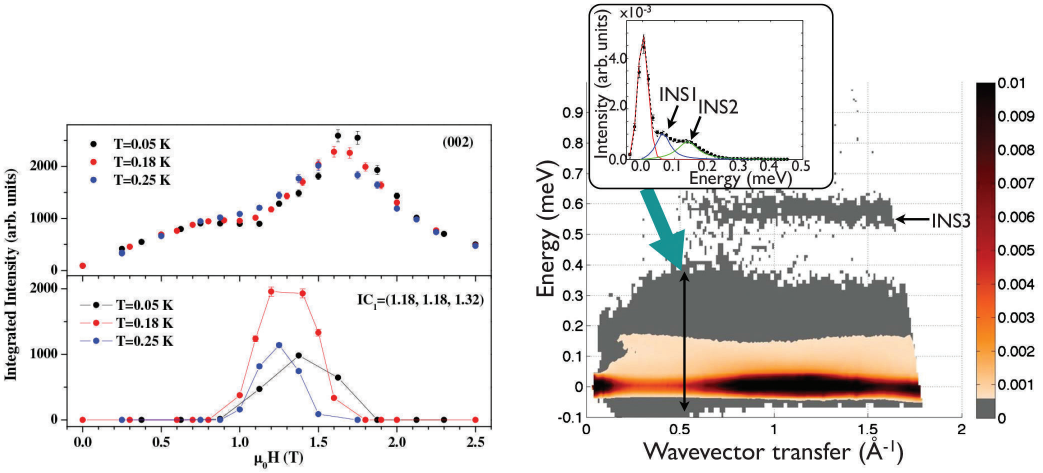

FIGURE 4.4: Left: H || $[1\bar{1}0]$ for several temperatures below 0.25 K (from reference [73]). Upper: field dependence of AF peak (002). Lower: Field dependence of incommensurate peak (1.18, 1.18, 1.32). Right: Gapped excitations in GGG (from reference [72]).

answer is provided to the reproducibility of the measurements on different samples and a refined H T phase diagram is presented [75].

4.3 Samples

Two $Gd_3Ga_5O_{12}$ samples have been measured, in collaboration with P. P. Deen (ESS Lund, Sweden):

- a single crystal of mass 8.52 mg cut from a commercial 10 × 10 × 0.4 mm substrate (Impex High Tech), measured along the [1 1 0] direction (within the plane)
- a 17.13 mg ^{160}Gd isotope powdered sample

Magnetization measurements using the two low temperature SQUID magnetometers, described in section 2.1.5, were performed down to 80 mK in applied magnetic fields up to 8 T. The measurements performed on the ^{160}Gd isotope powder are in quantitative agreement with those on the single crystal measurements (see figure 4.5). However, the features are broadened on the powder sample, certainly due to the distribution of crystallites and/or the presence of a small anisotropy ($\sim$ 0.04 K [60]).

The design of the sample gives rise to a negligible demagnetization field for the single crystal sample. However, a correction is applied for the powder sample.

4.4 Low magnetic field behavior

4.4.1 Magnetization

Magnetization was measured when cooling down the samples from 4.2 K to 0.08 K in an applied magnetic field of 0.01 T (see figure 4.5 left). Figure 4.5 right shows a monotonic decay of the inverse susceptibility ($\chi \sim M/H$ in such low field) with decreasing temperature. A linear behavior is observed down to 1.5 K. In this

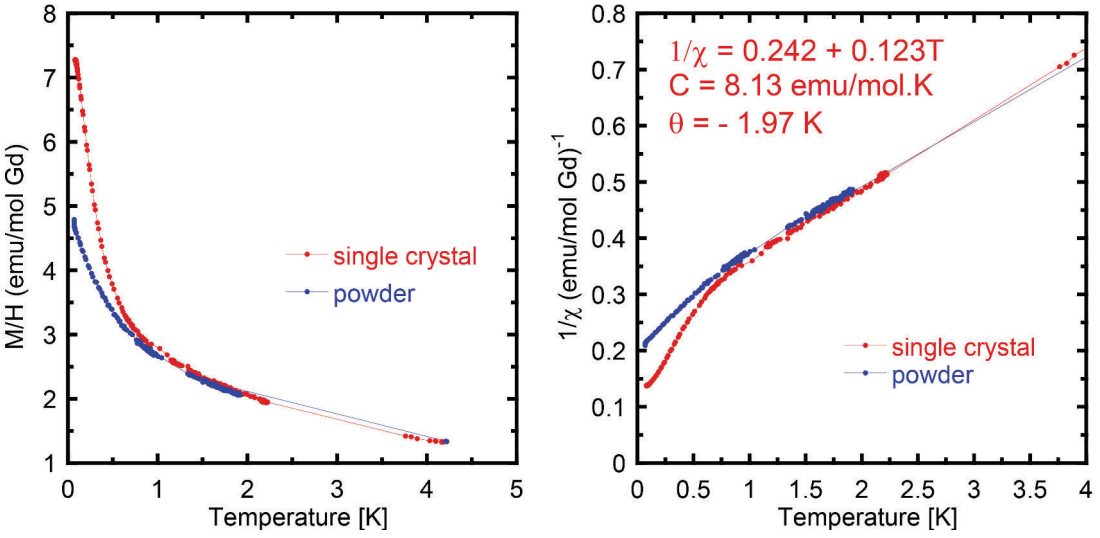

FIGURE 4.5: Left: M/H vs T at 0.01 T for a ^{160}Gd isotope GGG powder and a single crystal with H $\parallel$ to [1 1 0] for $0.08 < T < 4.2$ K. Right: $\chi^{-1} = H/M$ vs T for both samples and the Curie temperature and θ for the single crystal.

region, we can fit the inverse susceptibility to the Curie-Weiss law given by

$$\frac{1}{\chi} = \frac{T \quad \theta}{C} \tag{4.2}$$

$$\text{with} \qquad C = \frac{g^2 \mu_B^2}{3k_B} N_A \cdot S(S+1) \tag{4.3}$$

where C is the Curie constant, θ is the Curie-Weiss temperature, g is the Lande factor, μ_B is the Bohr magneton, k_B is the Boltzmann constant, N_A is the Avogadro number and S is the spin value.

A Curie constant of 8.13 emu.K/mol Gd is extracted from the fit which is consistent with the free Gd^{3+} spin moment, $S = 7/2$. The obtained Curie-Weiss temperature θ is 1.97 K in agreement with previous results [64, 65]. Below 1 K, the plot deviates from the linear behavior and becomes "less antiferromagnetic". This suggests that ferromagnetic interactions start to play a role at these temperatures.

To study the low temperature magnetization, we have performed *zero field cooled - field cooled* (ZFC-FC) temperature dependent magnetization measurements. The different steps of a ZFC-FC protocol are

- cool down the sample in zero applied magnetic field
- apply a certain magnetic field and measure the magnetization when increasing the temperature (ZFC).
- field cooled process (FC), requires the measuring of magnetization under applied magnetic field. Usually we perform measurements both when cooling down and when increasing the temperature, to check for possible hysteresis effects and problems of thermalization.

The ZFC-FC protocol is important for characterizing magnetic samples since it permits to observe magnetic transitions like spin glass, antiferromagnetic or ferromagnetic transitions, but also the presence of spin freezing in the system.

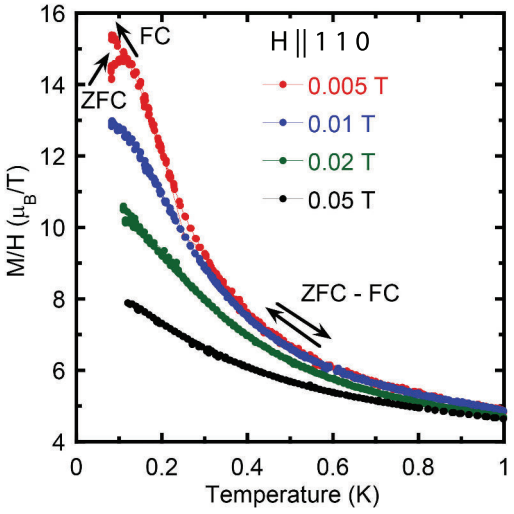

FIGURE 4.6: M/H vs. T measured with a ZFC-FC procedure for a range of applied fields $0.005 < H < 0.05$ T along the [110] direction.

Figure 4.6 shows the ZFC-FC measurements for several weak applied magnetic fields. At low fields, below 50 mT, the magnetization shows a freezing below 200 mK as previously reported [65]. To further study this spin freezing, we have performed AC susceptibility measurements.

4.4.2 AC susceptibility

AC susceptibility measurements were performed as a function of temperature for several frequencies and DC applied magnetic fields in order to have a better insight of the ground state of GGG (see figure 4.7). As we can observe, a different

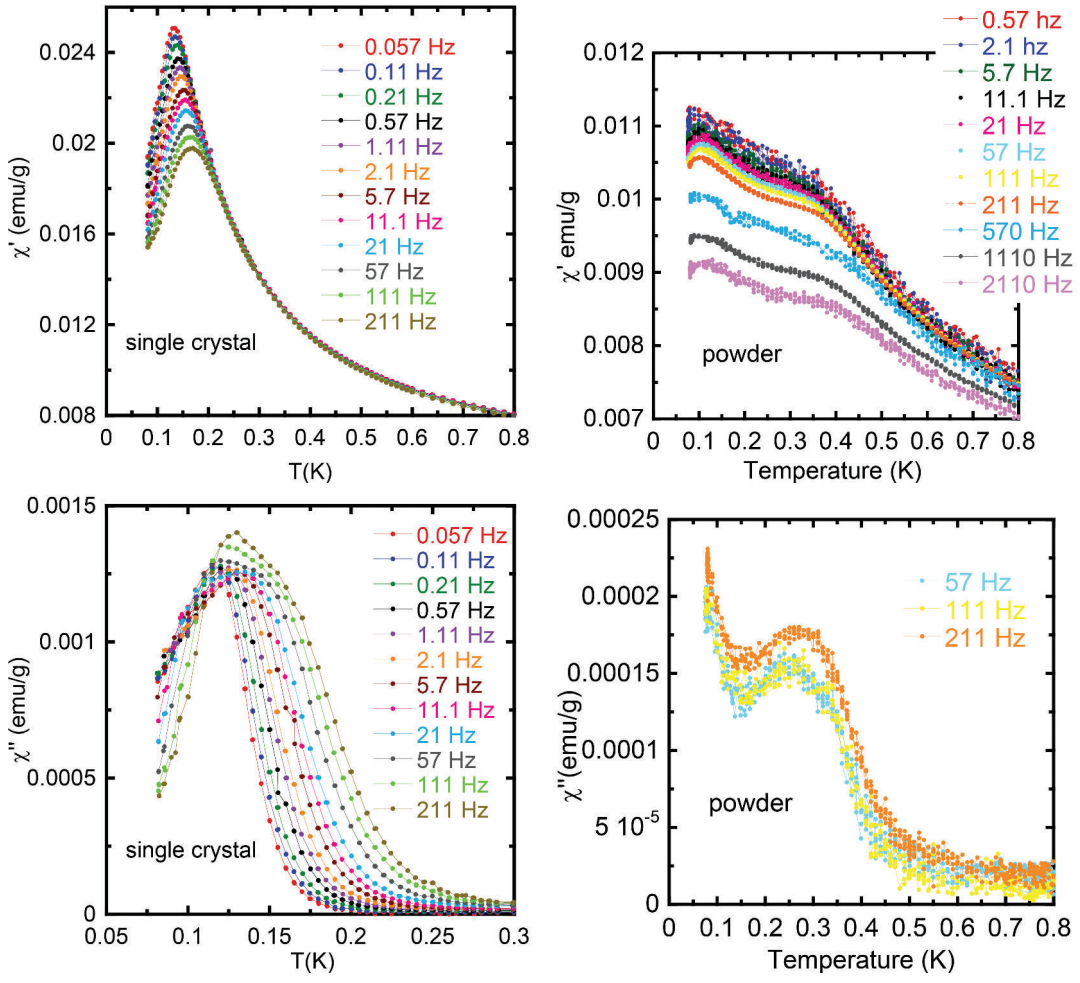

FIGURE 4.7: χ_{AC} vs T in zero DC magnetic field for the single crystal (left) and the powder (right).

behavior is seen in the powder sample compared to the single crystal. The real part of the alternative susceptibility, χ', shows a maximum below $\sim$ 200 mK in

the single crystal, while two broad maxima can be observed in the powder. The low temperature anomaly in the powder sample is in the same temperature range as the anomaly in the single crystal. A slight frequency-dependence of this maximum is observed. However, it can not be fitted with any of the law expected for canonical spin glasses (see section 3.2). The peak in χ' is accompanied by a peak in χ'' in both samples.

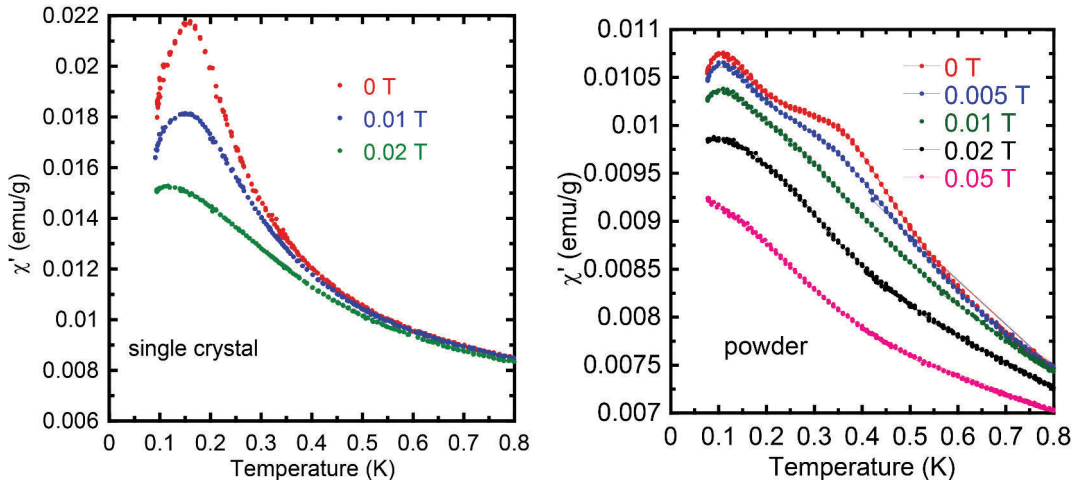

FIGURE 4.8: χ_{AC} vs T for several DC magnetic field for the single crystal (left) and the powder (right).

The application of a small applied DC magnetic field lifts the spin freezing for both samples (see figure 4.8). In the powder sample, we first observe the disappearance of the high temperature anomaly, while the low temperature anomaly remains robust up to 0.02 T, the same field for which it disappears in the single crystal.

The low temperature anomaly is in the temperature range in which Schiffer et al. suggested the possibility of a spin glass ground state. Our data show that the spin freezing depends on whether the sample is a powder or a single crystal. In addition the observed frequency dependence cannot be reproduced with a scaling dynamic law, and a fit to the Vogel Fulcher expression gives unphysical parameters (Note that such analysis was not reported in the study of Schiffer et al.). Therefore, these results seem to rule out the existence of a conventional spin glass behavior, in agreement with neutron scattering results. The spin freezing indicates the existence of long relaxation times, which might be related to different length loops of correlated spins, as proposed in the kagome lattice [76] and reported recently for GGG [77]. The sample dependence indicates that these relaxation times may be affected by the presence of defects in the system.

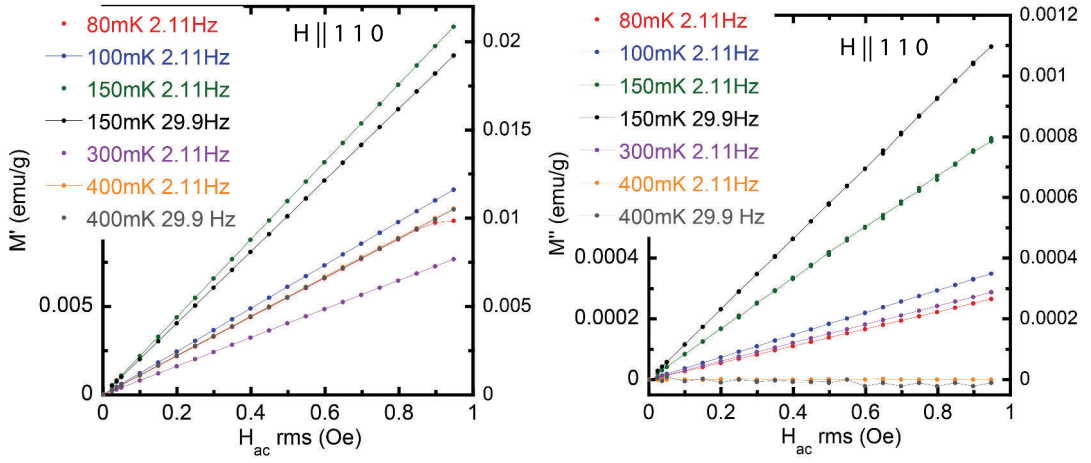

FIGURE 4.9: M_{AC} vs AC applied field for several temperatures and frequencies for the single crystal.

Ghosh et al. proposed the existence of spin protectorates in GGG from magnetization measurements as a function of alternative applied magnetic field [78]. They observed a nonlinear behavior of M′ corroborated with a peak in M″. To further explore this idea, we have tried to repeat their measurements on the single crystal, but we could not reproduce the behavior they had reported. We observed a linear response in both M′ and M″ (see figure 4.9).
The reason for the discrepancy between our measurements and Ghosh's measurements is unclear. Nevertheless, since we have measured different AC susceptibility on the powder and on the single crystal, the absence of reproducibility is not so surprising. Nevertheless, it shows that if such protectorate exists, it is very fragile.

We have thus characterized our samples in low fields. As expected they do not order down to very low temperature, but exhibit a spin freezing, different from a canonical spin glass behavior. No signature of anomalous behavior as a function of the ac applied field was observed. We now focus on the behavior of the system under applied magnetic field.

4.5 Phase Diagram

4.5.1 M vs H analysis

Isothermal magnetization measurements performed on the single-crystal and powder shows saturation around $M_{sat} = 7\ \mu_B$/Gd, as expected.
Above 2 K, a regular behavior is observed in the magnetization curve. However, in both samples, an anomaly is seen for temperatures below 1 K.

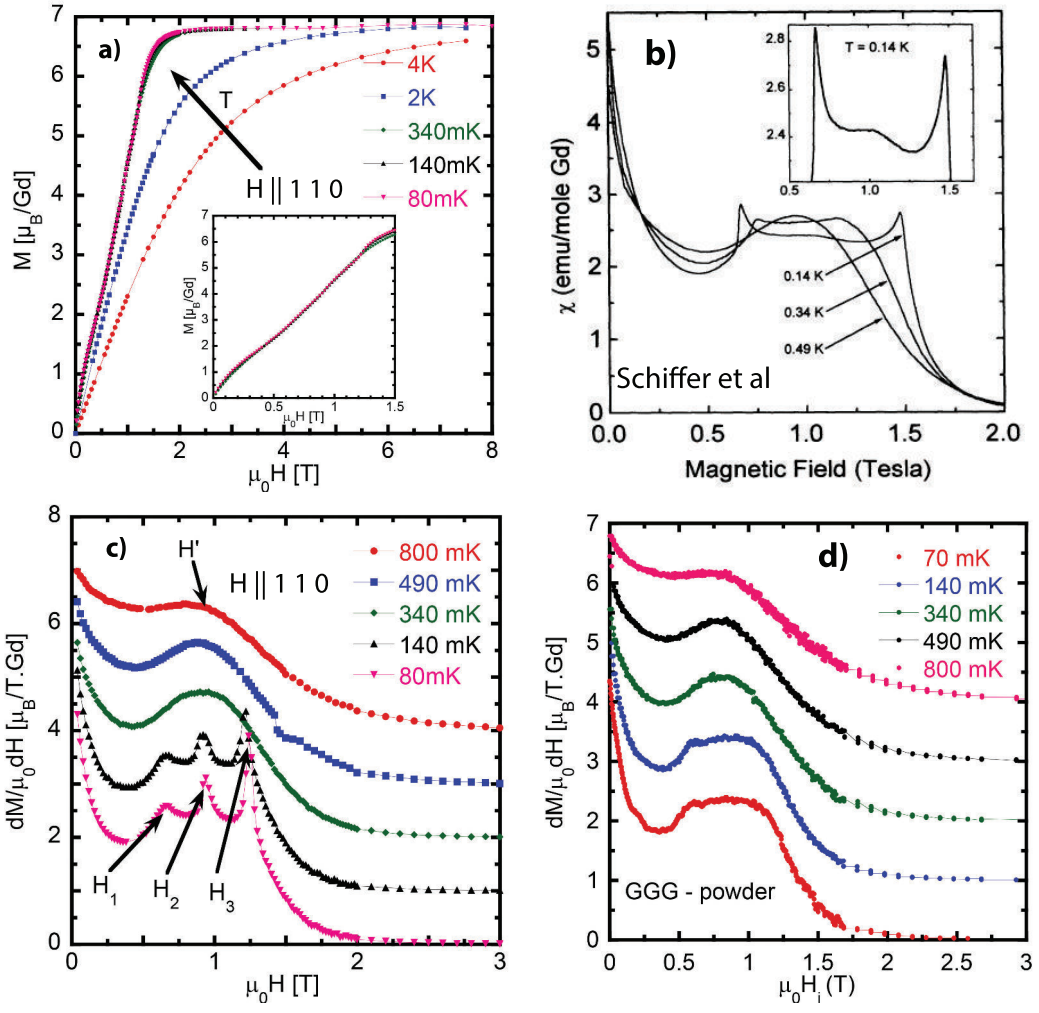

FIGURE 4.10: a) M vs H for $0 < H < 8$ T measured along [1 1 0] for several temperatures between 0.08 and 4.2 K. Inset: zoom on the anomaly between 0 and 1.5 T at low temperature. b) Schiffer's susceptibility measurements along [1 0 0]. c) dM/dH vs. H for a range of applied fields $0 < H < 3$ T measured along [110]. The curves for different temperatures are shifted by 1 μ_B for clarity. d) dM/dH vs. H for a range of applied fields $0 < H < 3$ T for the powder sample. The curves for different temperatures are shifted by 1 μ_B for clarity.

To study the evolution of the anomaly in the isothermal $M(H)$ curves, the curves are differentiated and dM/dH vs H is plotted as a function of the applied field. The magnetization is measured three times at each specific applied magnetic field. The derivative is computed over five consecutive values of the applied magnetic field. The obtained curves are plotted in figure 4.10. Similar features as the ones reported by Schiffer et al. [65] in heat capacity and susceptibility measurements are observed.

The main features we observe are:

- Below 1 K, a broad maximum develops around $\mu_0 H' = 1$ T.
- Below about 250 mK, three well-defined peaks develop (labeled H_1, H_2 and H_3) in addition to the broad feature centered around 1 T.

By correlating specific heat and susceptibility measurements, Schiffer et al assigned the broad feature to the quenching of the antiferromagnetic short range order (SRO). We did not performed specific heat measurements, but having similar features in our sample, we can as well assign H' to the development of the antiferromagnetic SRO. There is no significant change in the position or the width of this broad feature with temperature decreasing which suggests a robustness of the SRO correlations.

The sharp peaks, $\mu_0 H_1 \sim 0.65$ T and $\mu_0 H_3 \sim 1$ T seem to correspond to the boundaries of the previously observed field induced antiferromagnetic (AFM) long range order [65]. The temperature dependence of the peaks positions are in good agreement with previous measurements, but their positions are slightly different (certainly due to the small anisotropy of the Gd ion). H_1 does not depend on the temperature, while H_3 shifts to higher temperature as we decrease the temperature.

A new unseen sharp third peak is observed between $\mu_0 H_1$ and $\mu_0 H_3$, around $\mu_0 H_2 \sim 0.9$ T. This may be the signature of the existence of different magnetic arrangements in competition in this region. A feature was also observed in this field range in the work of Schiffer et al. [65], but it was much broader. It is worth noting that H_2 peak does not replace the broad SRO feature at H': to reproduce the dM/dH shape at low temperature, it is necessary to fit the curves with a Gaussian curve for the broad feature at H' and on top three Lorentzian curves for

the three peaks (H_1, H_2 and H_3). When the temperature increases, the positions of the three peaks and of the broad feature seem to converge towards a single point around $T^* \sim 0.3$ K at the magnetic field $\mu_0 H^* \sim 0.9$ T.

To observe the evolution of the anomaly in dM/dH vs H, we performed magnetization measurements as a function of temperature at constant field to try to get more insight into the fragile field induced states of GGG.

4.5.2 M vs T measurements

We have repeated the ZFC-FC protocol described for low field measurements for several applied magnetic fields up to 1.3 T, as shown in figure 4.11.

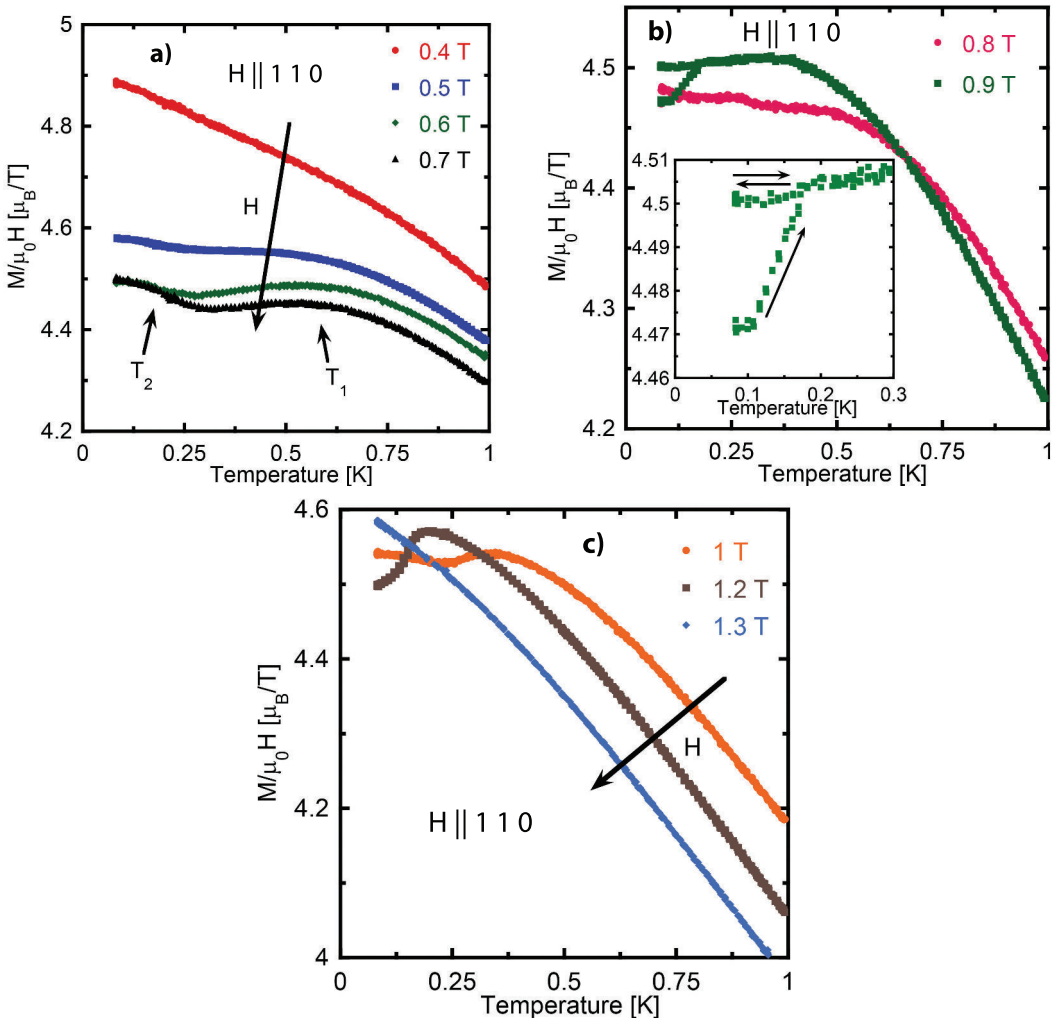

FIGURE 4.11: M/H vs. T measured with a ZFC-FC procedure for a range of applied fields $0.4 < \mu_0 H < 1.3$ T along the [110] direction.

- For $0.05 < \mu_0 H < 0.4$ T, ZFC and FC magnetizations overlay and decay monotonically with increasing temperature. No magnetic ordering is observed in this field range.
- For $0.5 < \mu_0 H < 0.7$ T, two distinct features are observed: a broad maximum around $T_1 = 0.6$ K and a change in slope around $T_2 = 0.2$ K. T_1 shifts to lower temperatures when the magnetic field is increased (Figure 4.11(a)).
- For $0.8 < \mu_0 H < 0.9$ T, the two features seem to overlap, so that no clear maximum emerges. A splitting in the ZFC-FC measurements occurs at $H^* = 0.9$ T below $T \sim 0.17$ K. This ZFC-FC hysteresis is quantitatively reproducible (it concerns 7% of the magnetization), and is present only at the specific field of 0.9 T. (Figure 4.11(b))
- For $0.9 < \mu_0 H < 1.2$ T, the curves recover the shape of the $0.5 < H < 0.7$ T region. (Figure 4.11(c))
- For $\mu_0 H > 1.3$ T, the magnetization decreases continuously with increasing temperature.

From these measurements, a very rich and complicated behavior is observed. The splitting of the ZFC-FC curves is quite common and it is followed by the lifting of the spin freezing when larger magnetic fields are applied. However, the re-entrance of the hysteresis behavior at high applied magnetic field is very surprising. It is observed in the powder sample too, and coincides with the magnetic field in which a peak is observed in the dM/dH curves, suggesting that something special occurs at this 0.9 T field.
But due to the complexity of the system, and different energy competitions, it is difficult to extract quantitative information on the stabilized magnetic states from the magnetization. For this reason, our study was performed in parallel with neutron scattering measurements. I present below these neutron scattering measurements which are in good agreement with the magnetic measurements. From a crossed analysis of these data, an updated phase diagram is proposed in the second part which opens new questions for the puzzling physics of these 3D frustrating lattices.

4.5.3 Neutron scattering measurements

Neutron scattering were performed on the ^{160}Gd isotope sample using the D7 diffuse scattering spectrometer.
The sample contains 99.98% isotope ^{160}Gd. It was covered with isopropanol (or 2 propanol) 99% deuterium that freezes the crystallites in orientation in magnetic field, without any substantial contribution to the scattering. The field-dependent data have been measured with incoming neutron energy $E_i = 3.55$ meV. Field dependent measurements were performed in magnetic fields up to 2.5 T at the lowest achieved temperature, 0.05 K. Temperature dependence measurements were performed between 0.05 and 0.8 K for 0.8 and 1.2 T. It would have been interesting to measure the sample at 0.9 T, the field value where there is an anomaly in dM/dH vs H, but the neutron scattering experiment ended before we observed the corresponding feature in isothermal magnetization measurements. However, a closer investigation of the 0.9 T - 0.3 K region is soon foreseen.
Uniaxial polarization measurements performed under applied field utilizing the protocol described in sections 2.2.2. The data have been corrected for detector and polarization analyzer efficiencies using standard samples of vanadium and amorphous silica, respectively. All data are corrected for background contributions by subtracting the scattering from an empty sample can under equivalent conditions.

Figure 4.12 displays the field dependence of neutron scattering at 0.05 K. A series of additional Bragg peaks besides an increase of intensities of nuclear Bragg peaks that accounts for ferromagnetism and in-cell antiferromagnetism are observed, in addition to the wavy background characteristic of the short-range order. These new peaks of magnetic origin cannot be indexed uniquely. Among them, one distinguishes those that can be indexed with fractional Miller indices that account for antiferromagnetic phases and those that can be indexed only with non fractional Miller indices that account for incommensurate phases. The existence of antiferromagnetic (AF), ferromagnetic (FM) and incommensurate (IC) peaks was already mentioned by Petrenko et al in their work [68], but for the first time we can also correlate them correctly with the short range correlations that they sit on top of. From these measurements we can clearly make a comparison between the observed field induced phase in magnetization measurements and the different scattering peaks. The antiferromagnetic peak at [3/2 1 1/2] develops at low fields and remains up to $\sim$ 0.65 T, which seems to delimit the SRO phase observed in

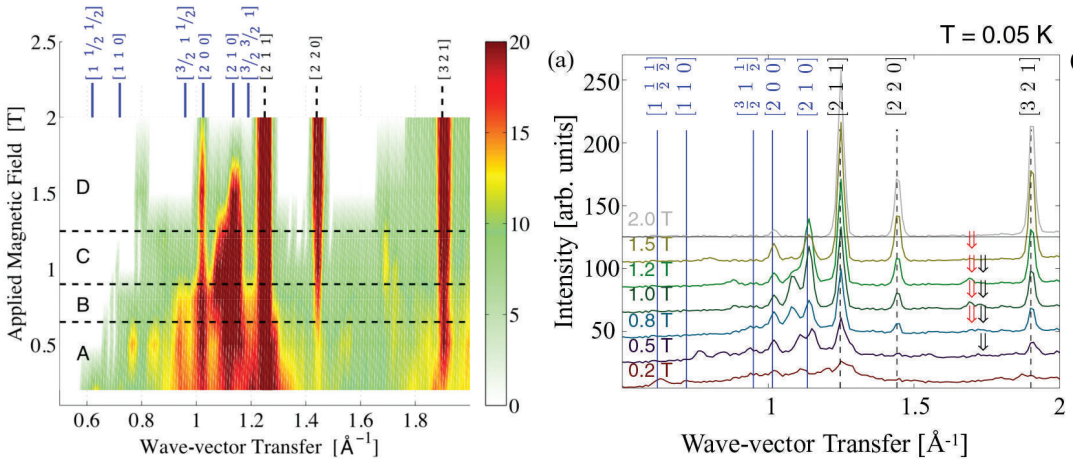

FIGURE 4.12: Field dependence neutron scattering at 0.05 K. Blue lines are the AF Bragg peaks, while dashed black lines corresponds to ferromagnetic Bragg peaks.

magnetization measurements.

Short range correlations (a broaden peak around 1.2 $\mathring{A}^{-1}$) develop at low fields,

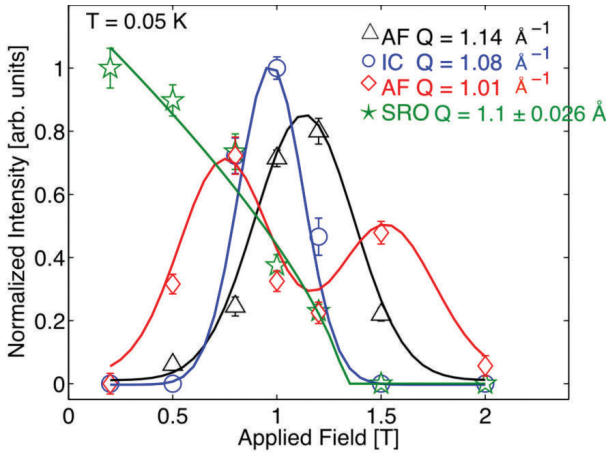

FIGURE 4.13: Field integrated intensities of AF, F, IC and short-range order

but remain robust even in the field induced phase, consistent with the SRO feature in the low temperature magnetization measurements. The incommensurate peak between [2 0 0] and [2 1 0] starts to develop in the field induced phase, seems to stabilize around the separation between the two observed regions of the field induced phase (around 1 T), to disappear for applied magnetic fields larger than 1.2 T. The [2 2 0] peak starts to develop around 0.8 T and seems to support the existence of two distinct behaviors in the field induced phase (region B and C in figure 4.12 left).

To summarize and visualize the different behaviors, in figure 4.13 we display the integrated intensities of characteristic antiferromagnetic, ferromagnetic, incommensurate peaks and short range order signal. It is interesting to see that they seem to follow the pattern observed in the magnetization measurements. The AF intensities are maximal around the field values where peaks in the field dependence of dM/dH are observed. A maximum of the incommensurate peak ($Q = 1.08$ $\mathring{A}^{-1}$) and the antiferromagnetic peak ($Q = 1.14$ $\mathring{A}^{-1}$) around 1 T are consistent with two distinct regimes in the field induced phase hypothesis.

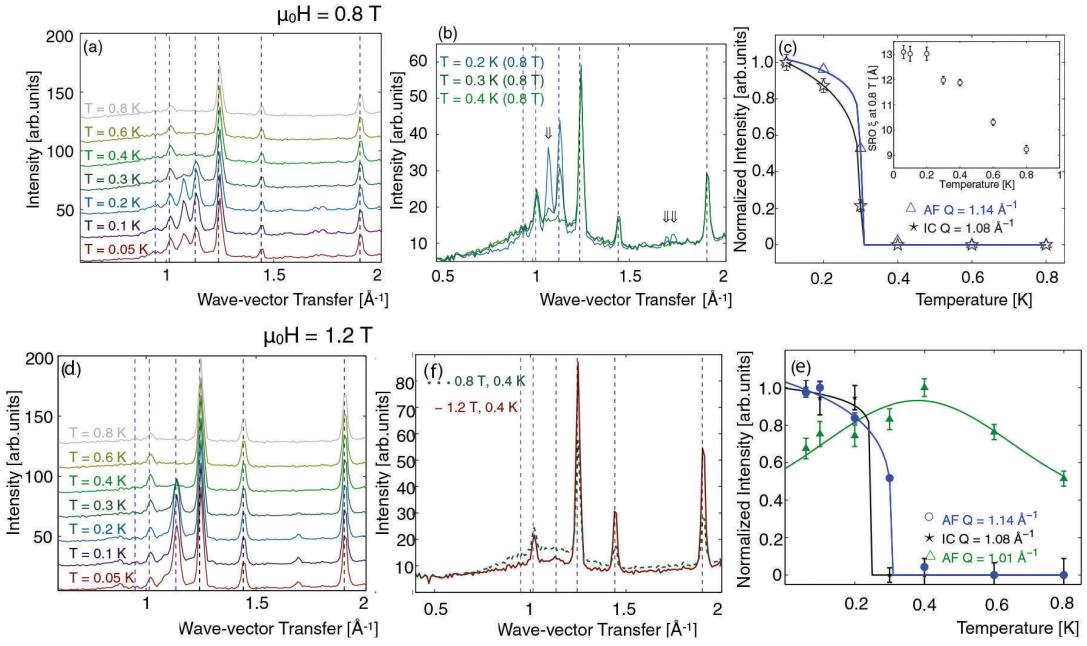

FIGURE 4.14: Temperature dependence of neutron scattering at 0.8 (a,b) and 1.2 T (d,f). Integrated intensities of the AF and IC peaks (c,e).

As mentioned above, temperature dependent scattering measurements were performed at 0.8 and 1.2 T. Figure 4.14 shows the results obtained and it highlights the transition from the high temperature regime ($T > 0.3$ K) to the low temperature one. For temperature larger than 0.3 K, both antiferromagnetic an incommensurate peaks vanish which seems to support the existence of the critical point observed in the magnetization measurements. Figure 4.14 f) display the difference between 0.8 and 1.2 T at 0.4 K. It suggests that the magnetic structure is different even in the short range order phase, with the existence of two distinct regions (labeled E and F on the phase diagram - see figure 4.15).

4.5.4 Updated phase diagram of $Gd_3Ga_5O_{12}$

By combining magnetic measurements and neutron scattering results, an updated H T phase diagram can be constructed as shown in figure 4.15. As expected, a complicated but rich behavior can be observed. A short-range ordered phase which seems to show several regimes, a field induced antiferromagnetic phase with a "critical" behavior around 1 T and a spin-freezing in the absence of applied magnetic field are the prove of exciting and emerging physics, but also of the shallow equilibrium of the ground state in these 3D frustrated systems. The study of GGG started a few decades ago, but new theoretical or experimental approaches are trying to explain the puzzling physics in this compound. However, till this date, a lot of questions remains unanswered.

Although we cannot answer to all these questions, our study has clarified the phase diagram of GGG. Below I present the main features we have obtained: The

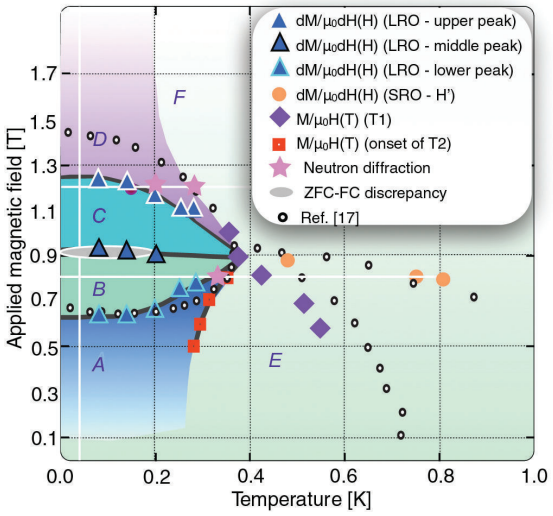

FIGURE 4.15: The updated phase diagram of $Gd_3Ga_5O_{12}$.

behavior at high temperatures, T_1 (orange circles) and H' (violet squares) can be associated with the SRO features observed in specific heat and susceptibility respectively by Schiffer et al. [65]. However, the low temperature change in slope around T_2 (red squares) indicates an evolution of the SRO state, which thus can be separated into two regions, A and E, separated at the onset of T_2. A difference between the neutron scattering profile at 0.4 K for 0.8 and 1.2 T suggests a separation of the low field and high field short range order phase (E

and F). Unfortunately, the origin for these effect remains unknown. A relevant effect of the dipolar interactions in this phase is highly suspected.

The antiferromagnetic field induced phase, separated by H_1 and H_3 (blue triangles) is in the field range values of previous works [59, 65, 68]. However, a more complicated behavior is observed as the new sharp peak in M vs H measurements at $H_2 = 0.9$ T (purple triangles) divides the AFM field induced region into two phases B and C. At the (B-C) phase boundary, a small region is reported in which the ZFC-FC discrepancy has been observed. Interestingly, this field of 0.9 T where an anomalous behavior is observed, corresponds to the field induced phases and SRO collapse. In that sense, it makes ($H = 0.9$ T, $T \sim 0.3$ K) a specific point in the phase diagram of GGG, which had not been reported up to now.

Another interesting feature is the existence of the antiferromagnetic and incommensurate peaks for H $>$ 1.4 T which persists up to at least 2 T. However, the existence of unconventional behavior is not seen in magnetization measurements in this field range, where the systems looks almost saturated. On the other hand, the zero field scattering profile can not be fitted only with nearest-neighbor spin model, but some feature might be explained when taking into account exchange interactions of loops of ten ion spins.

Faced with an interesting compound, yet not fully understood, our next step is the study of an isomorphous compound $Gd_3Al_5O_{12}$ (GAG). In this compound, Gd ions lie on the same hyperkagome lattice, but the distance between them is smaller. Therefore larger interactions between magnetic moments are expected. The idea is to probe whether these different interactions are able to destabilize the fragile ground state found in GGG.

Gadolinium Aluminium Garnet

Pour aller plus loin dans la compréhension de GGG, nous nous sommes intéressés dans ce chapitre à un composé de la même famille: Gadolinium Aluminium Garnet, formule $Gd_3Al_5O_{12}$, dit GAG, toujours en collaboration avec Pascale P. Deen (ESS Lund, Suède). Devant la complexité du diagramme de phase de GGG, l'objectif était de tester la robustesse des états stabilisés en faisant varier l'ion non magnétique. Le paramètre de maille de GAG étant plus petit que celui de GGG, on s'attend à observer des interactions renforcées.

A l'inverse de GGG, très peu d'études existent sur GAG. Nous avons donc entrepris une caractérisation magnétique complète du système. Nous avons pu confirmer que les interactions sont bien antiferromagnétiques, et effectivement plus élevées que dans le cas de GGG. Nous avons également observé un gel de l'aimantation et de la susceptibilité à très basse température analogue à celui obtenu dans GGG.

Nous avons établi un diagramme de phase champ-température similaire, avec une phase antiferromagnétique induite sous champ, pour des valeurs de champ plus élevées que GGG, comme attendu d'après l'ordre de grandeur des interactions. Le point de convergence est cette fois-ci obtenu autour de 1.3 T - 400 mK. Nous avons aussi mis en évidence l'effet anormal de réentrance de l'irréversibilité Zero Field Cooled - Field Cooled. Néanmoins, celle-ci a lieu pour des valeur de champ plus faible, et donc hors de la phase antiferromagnétique induite, ce qui remet en cause notre interprétation initiale sur GGG.

Cette étude nous a permis de montrer que le diagramme de phase complexe de GGG est robuste. Des études plus poussées de diffusion de neutrons sont maintenant nécessaires pour mieux sonder la coexistence de phases dans GAG.

Chapter 5

Gadolinium Aluminium Garnet

5.1 Motivations and State of the Art

Several papers in which Monte Carlo simulations were performed with the parameters of GGG, showed the ground state to be extremely fragile to perturbations [71, 73]. Our efforts in understanding the origin for the lack of ordering and complex H T phase diagram in GGG, continued with the study of $Gd_3Al_5O_{12}$ (GAG). The compound has the same hyperkagome structure as GGG, but with a smaller lattice parameter ($a_{GAG} = 12.172$ Å$< a_{GGG} = 12.385$ Å). By changing the distance between Gd spins, the exchange and dipolar interactions are expected to be modified and the question of the consequence on the ground state arises. In particular the anisotropic dipole exchange interaction is strengthened.

Quilliam et al. performed specific heat measurements on several garnets, including GAG, as showed in figure 5.1. A monotonic decrease is seen in GGG, however, a sharp peak is seen in GAG at 175 mK [79]. This suggests a possible transition in the system. However, the authors warned the possibility that the effect could come from sample impurity.
A brief magnetic characterization of the sample was made by Sackville Hamilton et al. in 2014 [80] for temperatures larger than 2 K. In their paper, they measure several samples with composition $Gd_3Ga_{5\ x}Al_xO_{12}$ with $0 < x < 5$. The Curie-Weiss temperature for GAG is $\theta =$ 4 K, larger then the one for GGG. They conclude that the magnitude of the antiferromagnetic interactions increases with the Al doping.

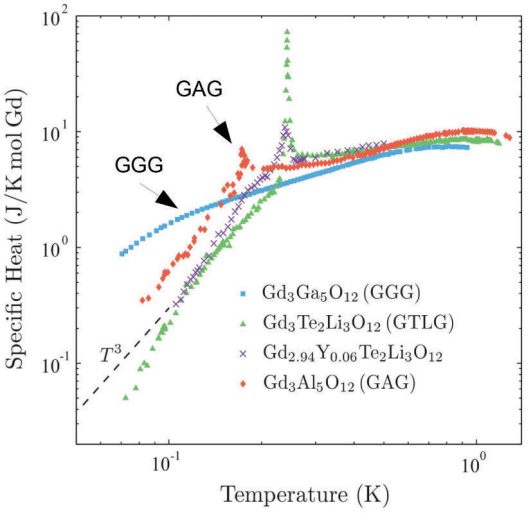

FIGURE 5.1: Specific heat measurements on several garnets. GGG and GAG are highlighted

5.2 High Temperature Magnetization

Aiming at fully characterizing this little studied system, I started to measure the sample magnetic properties from room temperature down to the lowest temperatures.

A 3 mg powder sample was measured down to 2 K and in magnetic fields up to 5 T using a commercial Quantum Design SQUID magnetometer (see figure 5.2). When cooling down the sample in a small applied magnetic field (0.01 T), a linear behavior of the inverse susceptibility as a function of temperature is observed down to 50 K (see inset figure 5.2 left). Below 50 K, the curve deviates from the paramagnetic behavior. From the fit between 50 and 300 K, and using equation (4.3), a Curie-Weiss constant of 8.7 emu.K/mol Gd and a paramagnetic Curie-Weiss temperature of - 9.8 K are extracted.

The theoretical Curie constant for free Gd spins, $S = 7/2$, is around 8 emu.K/mol. Therefore, the experimental value is about 10 % times too large. The temperature range of the fit can impact the obtained value, but in our case, no significant difference is obtained when this range is changed. As we will see below the obtained saturated magnetization is consistent with a 7/2 spin, so that this discrepancy cannot be due to a problem in the absolute values. It might originate in some anisotropy effect. Finally, it could be due to a diamagnetic component that should have been subtracted, but it was not done in the case of GGG either.

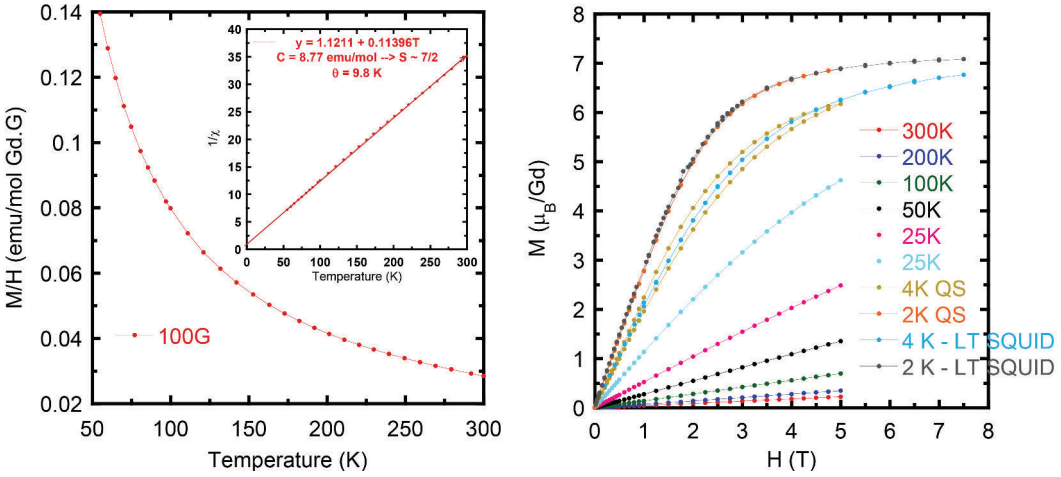

FIGURE 5.2: GAG: M vs H for several temperatures. QS stands for Quantum Design SQUID magnetometer and LT SQUID for the home made SQUID described in chapter 2.1.5. Measurements are highlighted to show the good agreement between the two experiments

The paramagnetic Curie-Weiss temperature is in agreement with the antiferromagnetic behavior observed in specific heat and previous measurements.

From isothermal magnetization measurements, a linear dependence of the magnetization is observed for temperatures larger than 25 K. No saturation is reached in this temperature and applied magnetic field range. At 4 K, the Quantum Design SQUID measurement shows a hysteresis in the magnetization measurements, while the low temperature SQUID does not. We believe the hysteresis to be an artifact due to problems in temperature calibration in this regime (the cooling is made through ^{4}He directly in contact with the sample and problems sometimes occur at the gas-liquid transition at 4.2 K) or from a heating effect because of the measurement design. These problems do not exist in our low temperature SQUID magnetometer, since the sample is carefully thermalized between two copper foils, and is in the vacuum. The fact that this measurement lies in the middle of the hysteresis as well as the superposition between the data at 2 K, confirms this interpretation. In the low temperature SQUID magnetometer measurements, the saturation of the magnetization at about 7 μ_B is reached around 7 T.

5.3 Low magnetic field behavior

A 5.7 mg powder sample is cooled down in a 5 mT applied magnetic field (see figure 5.3 left). The minimum temperature achieved is 100 mK.

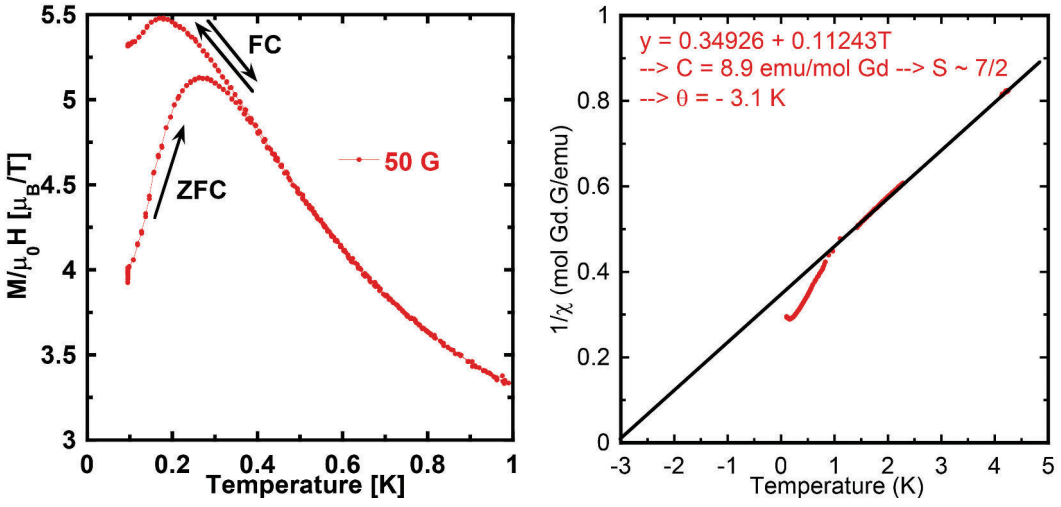

FIGURE 5.3: Left: ZFC-FC vs T at 5 mT. Right: $1/\chi$ vs T and the corresponding Curie-Weiss fit.

From the inverse susceptibility, a Curie-Weiss temperature of -3 K and a Curie constant of 8.9 emu.K/mol Gd are extracted. Note that the discrepancy with the theoretical Curie constant is similar to high temperature measurements.

Below 1 K, the curve deviates from the paramagnetic behavior. Like in GGG, it suggests that ferromagnetic interactions come into play. An irreversibility between the ZFC-FC protocol is observed for temperatures below $\sim$ 355 mK. In addition, a rounded maximum is observed below $\sim$ 200 mK. The larger value of θ and T_g than the one in GGG is consistent with a smaller lattice parameter and the existence of larger interactions in GAG.

AC susceptibility measurements were performed in zero DC magnetic field for several frequencies between 60 mHz and 110 Hz (see figure 5.4). The real part of the alternative susceptibility, χ', shows a maximum below $\sim$ 340 mK. As in GGG, a slight frequency-dependence of the maximum is observed. However, it can not be fitted with any of the law expected for canonical spin glasses (see section 3.2). The peak in χ' is accompanied by a peak in χ'' around the same temperature value, which can be understood in terms of dissipation at the freezing

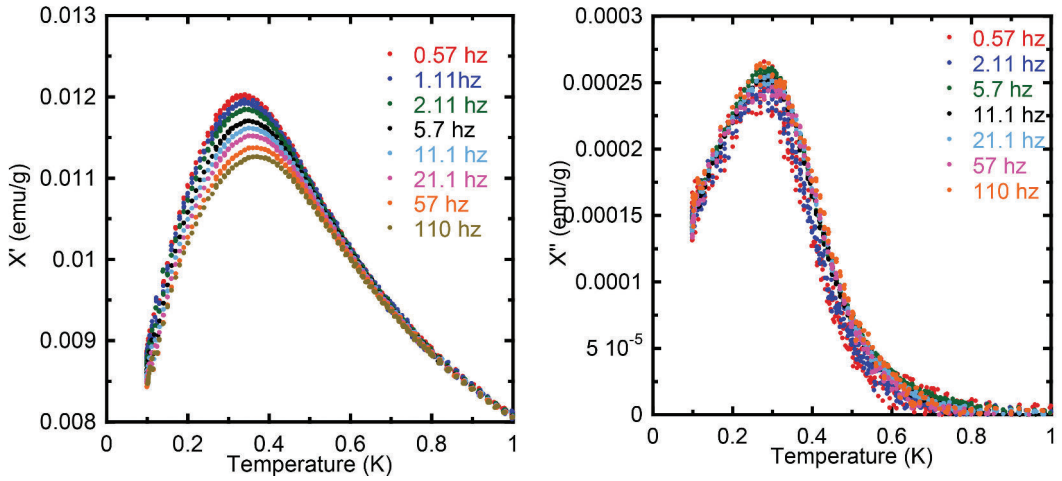

FIGURE 5.4: χ_{AC} vs T in zero DC magnetic field.

"transition". Again, the results are consistent with the picture of larger antiferromagnetic interactions in GAG compared to GGG, but which seem not to affect the ground state.

In conclusion, no clear transition is seen in GAG, but antiferromagnetic correlations develop at low temperatures associated with a spin freezing below ~ 350 mK.

5.4 Phase Diagram

5.4.1 M vs H measurements

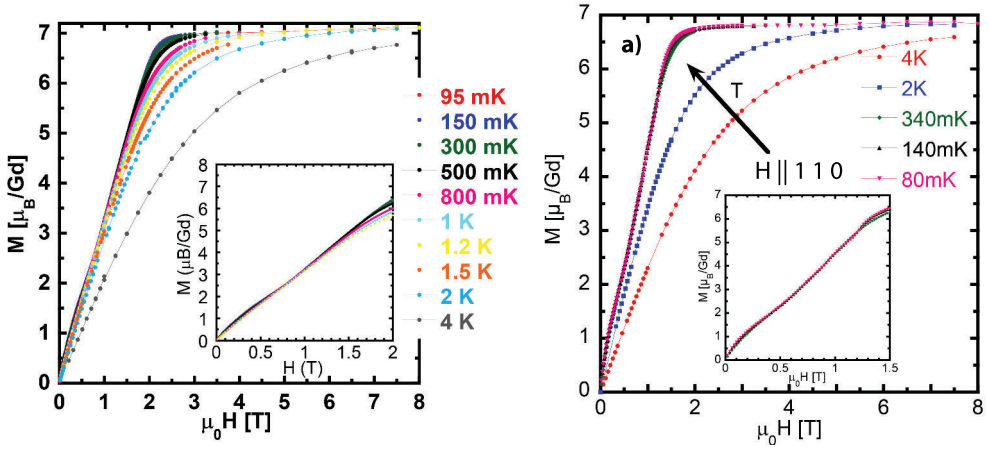

FIGURE 5.5: M vs H for several temperatures. Left: GAG (powder). Right: GGG (single crystal).

Field dependence measurements for several temperatures are presented in figure 5.5 left. The same measurements on GGG are shown in parallel, to easily compare the two compounds. Qualitatively we obtained the same results. Both samples saturate around 7 μB. Below 1.2 K and for applied magnetic fields between 0.5 and 1.5 T, a similar curvature of the low temperature magnetization is seen in GAG. We performed the same derivative protocol of the M vs H measurements as in GGG, to better study the anomaly.

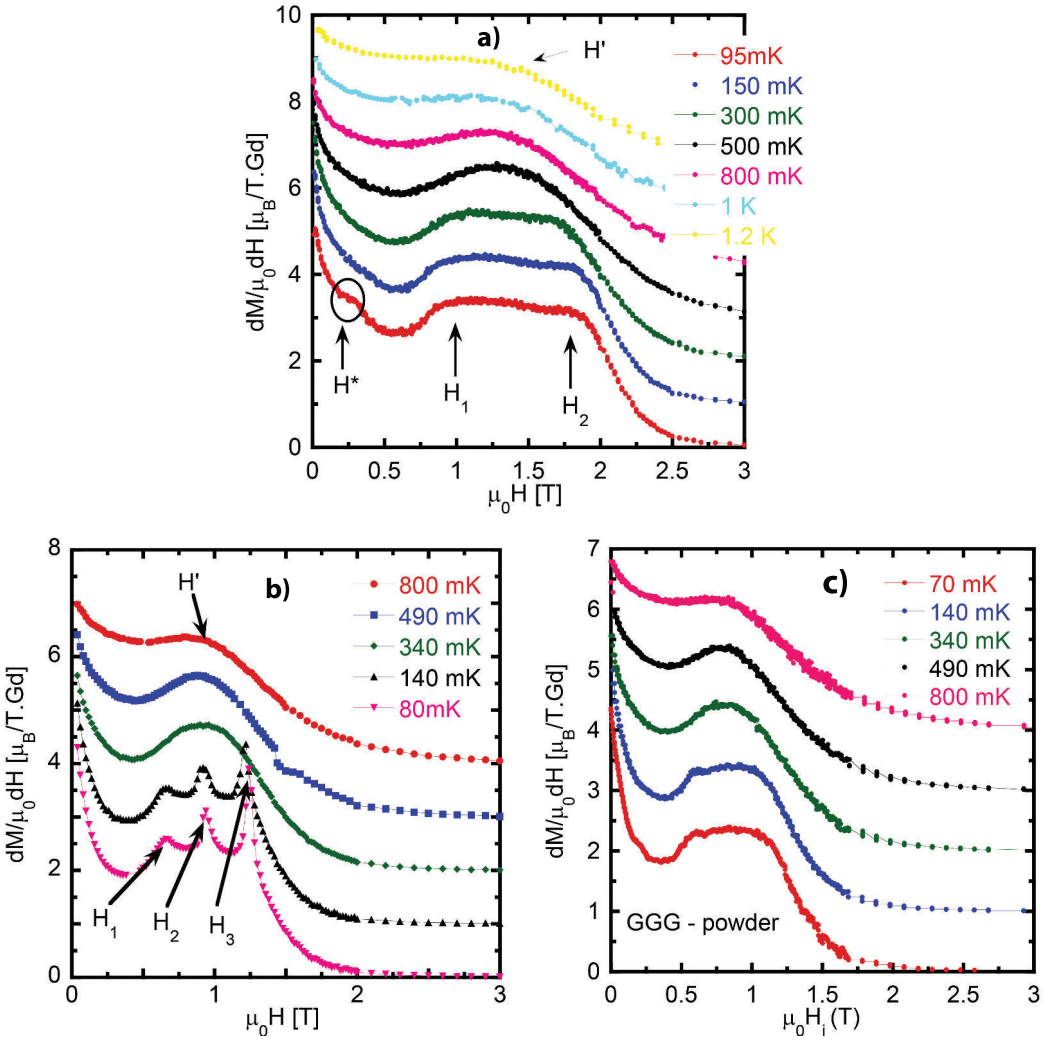

FIGURE 5.6: dM/dH vs H for several temperatures. a) GAG (powder). b) GGG (single crystal). c) GGG (powder)

Figure 5.6 shows the results for GAG and GGG. The same features are observed as in the GGG powder, but shifted to larger applied magnetic fields. We do not have specific heat measurements on our sample, as well as neutron scattering experiments in applied field, to help analyze our data and build the phase diagram. Nevertheless, since GAG has the same lattice topology as GGG, and seems to

present the same ground state, we make the analogy between measurements on the two samples to understand the field induced phases.

From this analogy, we can conclude that short range correlations develop below 1.2 K. For temperatures below 300 mK, a field induced ordered phase occurs between 1.1 and 1.7 T. A broadening of the maximum compared to GGG and also a shift in field is observed. The reason for the broadening is that the measurements were performed on a powder. As we can see from figure 5.6(c), the same broadened effect is observed in the GGG powder sample, and prevents from observing the central peak at H_2. The shift of the field induced phase to higher fields is attributed to larger antiferromagnetic interactions in GAG.

5.4.2 M vs T measurements

To follow the evolution of the anomaly observed in M vs H measurements, magnetization measurements as a function of temperature were performed for several applied magnetic fields. Figure 5.7 shows the same complicated behavior already observed in GGG.

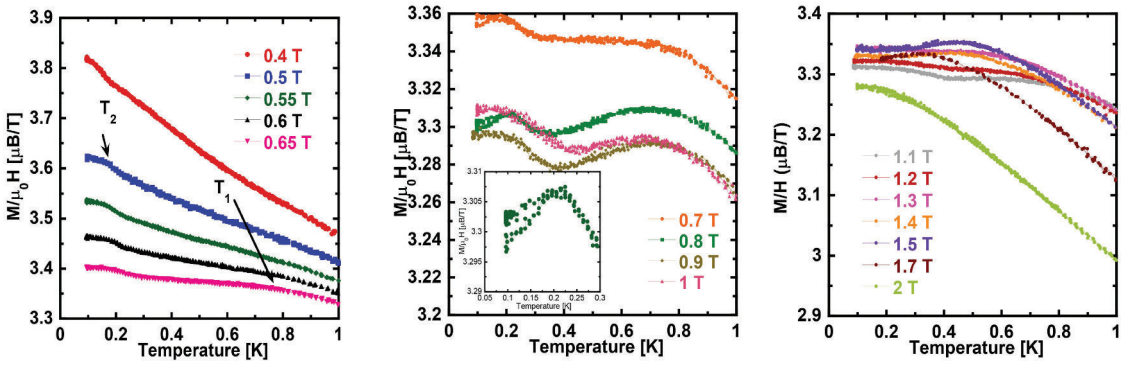

FIGURE 5.7: M vs T for several applied magnetic fields.

A monotonic decrease of the magnetization as we increase the temperature is observed for applied magnetic fields smaller than 0.5 T.
For $H > 0.5$ T, a broad peak and a change in slope, at high, respectively low, temperature are observed. The broad feature is at slightly higher temperature than in GGG, around 750 mK. The change in the magnetization slope is small at low fields and increases in value in the field induced ordered phase.
The same odd re-entrance of the ZFC-FC irreversibility is observed in GAG as

in GGG. Compared to GGG, where this hysteresis was observed around the field where the new sharp peak was found, in GAG, this hysteresis in the zero field cooled - field cooled protocol occurs for a range of fields between 0.7 and 0.8 T.

5.4.3 Phase diagram of GAG

From all these measurements, we have built the phase diagram of GAG presented in figure 5.8.

The low magnetic field characterization showed a broad peak at temperatures below 200 mK, but no clear transition signature is observed. The dynamic study of GAG revealed a spin freezing in the system for temperatures below 340 mK. A frequency dependence of the maximum of χ' is observed, however, it is not consistent with a canonical spin glass ground state.

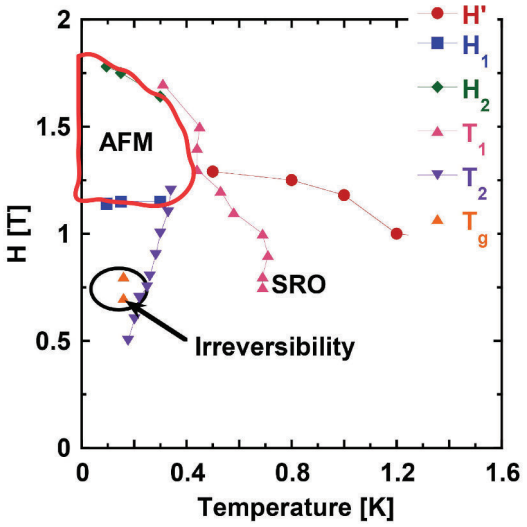

FIGURE 5.8: GAG: H T phase diagram

Below 1.2 K, a short-range order establishes in GAG (red circles). As in GGG, it seems to be splitted into two distinct regions, effect which is highlighted by the existence of a broad peak (pink triangles) and a change of slope (purple triangles) in the temperature dependence of the magnetization at constant applied magnetic field.

Under applied field, an antiferromagnetic induced ordered phase occurs between 1.1 and 1.7 T for temperatures below 300 mK.

An odd behavior, seen in both GGG and GAG, is the irreversibility in ZFC-FC measurements (orange triangles) that occurs at higher applied magnetic fields. In the case of GAG, the hysteresis takes place for applied fields between 0.7 and 0.8 T. The significant difference between the two compounds is made by the region where we can observe the irreversibility in ZFC-FC measurement. In GGG it is found inside the field induced ordered phase, while in GAG outside of it. The fact that the reentrant ZFC-FC effect in GGG was found at the border of the two distinct phases in the interior of the field induced ordered phase, made us believe that the two anomalies are connected. However, the same effect found in GAG, is observed for a wider applied magnetic field range and not even in the field induced ordered phase. It shows that the origin is more complicated. A possibility is that this effect is due to an impurity in the samples. But because the anomaly does not occur at the same fields in both samples seems to rule out this hypothesis. Careful neutron scattering measurements around this field in GAG might help to capture the origin of this phenomenon, and conclude whether it is a characteristic of these Gd antiferromagnetic hyperkagome systems. It will be interesting to measure other Gd based hyperkagome systems to further investigate the origin of this effect.

All these field induced phases seem to converge to a critical point, in the same manner as in GGG. The broadening effect due to measurement on powder prevent from a deeper analysis. It will be interesting to observe if a sharp peak develops inside the field induced region as well as if the anisotropy of the H T phase diagram is found in GAG as well. For this, a single crystal is required, but we do not have one at the moment.

In the end, preliminary zero field neutron scattering measurements on GAG display the same short range correlations as in GGG. However, no sharp Bragg peaks are observed down to 50 mK. Analysis of the data is in progress, results which might unravel some of the unanswered questions. Further measurements under an applied field are needed to refine the present phase diagram: Are we going to find antiferromagnetic, ferromagnetic and incommensurate peaks in the neutron scattering data? Will these peaks evolve in the same way as in GGG ? Or will they occur in different parts of the phase diagram ? A lot of questions remain that might attract the attention of further theoretical and experimental works, to succeed in understanding the magnetic states of Gd based hyperkagome lattice

compounds.

5.5 Conclusions

As mentioned in the introduction, a rich magnetic behavior is expected to be found in 3D frustrated systems. As shown above, the two compounds studied during my PhD display very interesting physics. It is indeed rare to find compounds which exhibit such complex behavior. In addition, the convergence of all these phases to a "critical" point is very interesting.

It is worth noting that while in other 3D frustrated systems, such as pyrochlore oxide compounds, changing the non magnetic ions induce completely different magnetic properties, the substitution of Ga by Al does not seem to affect the magnetic ground state of the Gd garnets. Apart from the strange behavior of the ZFC-FC reentrant irreversibility, it seems to only rescale the energies involved in the system.

Further studies on a GAG single crystal and a full analysis on the neutron scattering data might reveal some of the unanswered questions.
After studying non conventional behavior in classical frustrated materials, I further focused on the study of quantum frustrated molecular magnets, to probe the relation between quantum effects and frustration.

Aimants moléculaires

Dans ce chapitre, nous nous intéressons au cas des aimants moléculaires frustrés pour aborder la thématique de la frustration géométrique dans les systèmes de spins quantiques. L'idée est de s'appuyer sur la versatilité de la chimie moléculaire pour étudier une variété de systèmes frustrés à base d'ions Cu^{2+} ($S = 1/2$). En particulier, nous voulons étudier le rôle de la frustration dans des clusters de taille finie. Dans ces systèmes, l'application d'un champ magnétique permet de sonder le spectre d'excitations par les croisements Zeeman, qui induisent des plateaux d'aimantation, et les résultats expérimentaux peuvent être comparés aux calculs. Notre magnétomètre de Faraday sera donc spécialement adapté à l'étude de tels systèmes.

Nous avons étudiés deux composés, synthétisés par l'équipe de notre collaboratrice, A. K. Powell (KIT Karlsruhe, Allemagne).

Le premier est un cluster à base de tétraèdres de Cuivre en interactions antiferromagnétiques, Cu_{44}. Nous avons mesuré les propriétés magnétiques de ce système entre 300 K et 70 mK. Nous avons pu observer la formation de clusters antiferromagnétiques. Cependant, à très basse température, des interactions interclusters entrent en jeux, qui empêchent d'étudier l'état du spin collectif ainsi formé. De plus, la complexité du système (44 atomes de cuivre) et de la géométrie des échanges mis en jeu ne nous ont pas permis d'approfondir cette étude.

Le second est un réseau kagomé de Cuivre avec une hiérarchie d'interactions J_1, J_2, $J_1 \gg J_2$. La première étant ferromagnétique, et la seconde antiferromagnétique, le système peut être vu comme un réseau de trimères de spins 3/2 en interactions antiferromagnétiques sur un réseau triangulaire. Nos mesures ont montré l'existence d'un plateau d'aimantation à très basse température, qui apparaissait extrêmement prometteur dans l'étude de la frustration de ce composé. Cependant, en approfondissant les mesures, nous avons réalisé que le composé se dégradait dans

le temps, rendant impossible une étude quantitative des propriétés observées. En attendant les résultats des analyses chimiques, et les procédures à suivre pour éviter cette dégradation, nous avons donc préféré interrompre cette étude.

Chapter 6

Molecular Magnets

6.1 Introduction

The first part of my thesis was dedicated to the study of classical frustrated systems. To address the question of the role of frustration on quantum systems, we have chosen to focus on the little studied field of quantum frustrated clusters, and more specifically, quantum molecular magnets.
Molecular magnets are suitable due to possibility of creating finite quantum frustrated systems as well as to change the interactions between magnetic clusters.
The interest to consider finite quantum frustrated systems is two fold. First, entangled spin ground states and excitations can be fully and robustly realized in them with possible imprints of the novel phases which are expected in infinite systems. Second, finite systems allow the comparison between experimental results and exact diagonalization calculation. In addition, by changing the inter-clusters interactions we can mimic and compare our results with perturbative approaches of extended quantum frustrated spin compounds.
Up to this date, few experimental and theoretical studies were performed on such systems. A few examples are the triangular clusters V_{15} [81–83] and Cu_3 [84] or in rings of odd number of spins like Cr_8Ni [85, 86] nanomagnet.

As for theoretical reviews, one of the recent and complete ones is the work of Schnack et al [87, 88]. Figure 6.1 left, shows the excitation spectrum as a function of the total quantum spin, calculated for rings of even number of spins 5/2. Such bipartite structures favor condensation into a Néel state which result into a so called *rotational band* like energy spectrum. The minimum energy level for

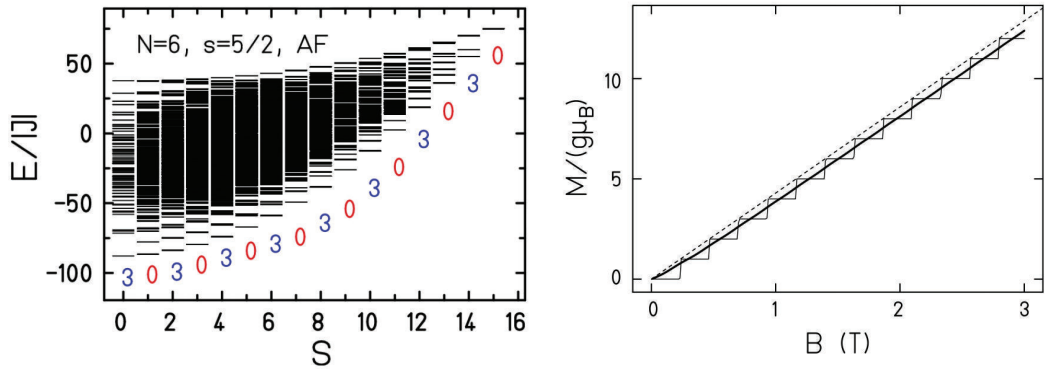

FIGURE 6.1: Left: energy eigenvalues of a spin ring (N = 6, s = 5/2) with antiferromagnetic nearest neighbor coupling as function of total spin S. Right: magnetization for T = 1 mK (staircase) and T = 100 mK (solid curve).

each total quantum spin number describes a parabola (or rotational band), which result in a staircase behavior of magnetization with regularly spaced steps when a magnetic field is applied.

For example, for an antiferromagnetic nearest neighbor exchange interaction, $J/k_B \sim$ -0.78 K, the calculated magnetization for 1 and 100 mK is presented in figure 6.1 right. At the lowest temperature the regular steps behavior can be observed, but unfortunately, at 100 mK the thermal energy is broadening this effect.

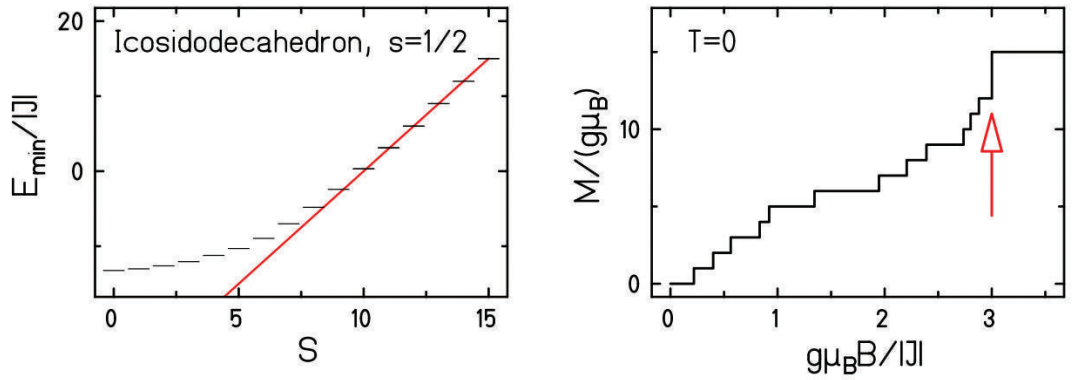

FIGURE 6.2: Minimal energies of icosidodecahedron lattice with antiferromagnetic s = 1/2 interactions. The resulting magnetization at T = 0 K

While Néel antiferromagnets exhibit an energy spectrum in the form of a parabola, in the case of frustrated systems, irregular patterns are expected in the excitation spectrum as a function of the total spin number.

For example, in the case of the icosidodecahedron of quantum spins, s = 1/2, the

energy spectrum displays a linear behavior for collective spin, $S > 10$, as shown in figure 6.2 left. The linear behavior results in irregular steps of the magnetization (jumps, plateaus), as shown in figure 6.2 right. Therefore, if an excitation spectrum presents an irregular pattern as a function of the total spin number, irregular steps in magnetization are expected.

My study focused on two frustrated copper ($s = 1/2$) molecular clusters provided by the group of A. K. Powell from Karlsruhe (KIT Karlsruhe, Germany): one with interconnected tetrahedrons of 44 copper spins and the second with copper spins on a triangular lattice of triangles. The idea was to probe the excitation spectrum of these systems through field induced crossing and anti-crossing of spin excitation energy levels. If the application of a magnetic field displays jumps or plateaus in magnetization of frustrated molecular magnets, the excitation spectrum can be built by comparing measurements with exact diagonalization calculation.

6.2 Cu_{44} molecular magnet

At the beginning of my thesis, through a collaboration with the KIT, we had the opportunity to study the molecular magnet:
$[Cu_{44}(\mu_8\text{-}Br)_2\text{-}(\mu_3\text{-}OH)_{36}(\mu\text{-}OH)_4(ntp)_12Br_8(OH_2)_{28}]Br_2 \cdot 81H_2O$,
which I will label Cu_{44}. Each cluster has 44 $s = 1/2$ copper spins arranged on a distorted tetragonal lattice with antiferromagnetic exchange interactions (see figure 6.3). It is a complex system, but it can be an interesting prototype to study the effect of frustration on the energy spectrum with the condition that the secondary interactions do not lift the frustration in such system. The objective is to probe the existence of possible jumps in magnetization through magnetic measurements. If irregular multiple jumps are observed in the magnetization curve, a characterization of the excitation spectrum in the molecule is possible.

The system was characterized by our collaborators [89] using DC magnetic susceptibility measurements on a polycrystalline sample between 300 and 2 K. From the fit with the Curie-Weiss law (see equation (4.3)) of the inverse susceptibility, they extracted a Curie-Weiss constant of 18.6 emu·K·mol ^{1} and a Curie-Weiss temperatures, θ = - 30 K. The Curie constant is larger than the value for 44 copper free spins (16.5 emu/mol) and it was interpreted by a larger Lande constant value (2.12 in the place of 2). The negative value of θ suggests antiferromagnetic interactions in the system.

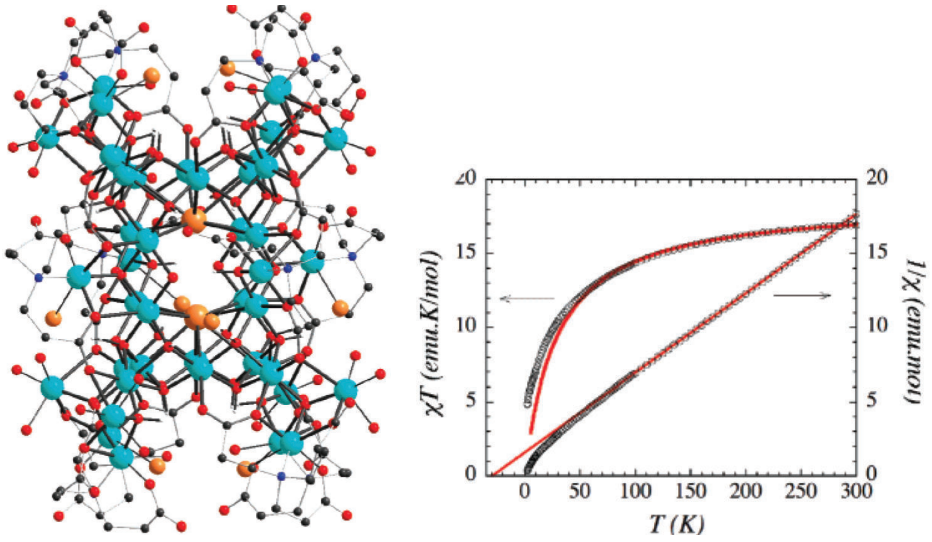

FIGURE 6.3: Left: Structure of the Cu_{44} aggregate (copper - blue ions). Right: Temperature dependence of χT at 0.1 T (from reference [89])

6.2.1 High temperature magnetic characterization

Magnetic measurements were performed on our sample, using a commercial Quantum Design SQUID magnetometer, to check the predicted behavior and the purity of the sample. We performed measurements in temperatures down to 2 K and in magnetic fields up 5 T. We measured a 22.4 mg of polycrystalline sample wrapped in cellophane. The cellophane is chosen specifically for this instrument in order to have a minimal background noise due to the diamagnetic signal.

A first cooling down of the sample in a small applied magnetic field (0.1 T) is presented in figure 6.4. No anomaly is seen in the temperature dependence of the magnetization in this temperature range. A χT data treatment was performed to compare our results with those published by our collaborators from Karlsruhe. The raw data are those extracted directly from the magnetometer and the corrected data are those after the collective diamagnetic signal of every element from the molecular compound, as well as the cellophane used to wrap the sample, was subtracted. The diamagnetic signal of the cellophane is of the order of 10 ^{7} emu/g which is roughly 1000 times smaller than the resulting magnetic signal of the sample at low temperatures in the absence of an applied magnetic field.

If we are in a paramagnetic regime ($\chi = C/(T \quad \theta)$), at high temperatures a χT plot as a function of temperature should recover a constant ($\chi T = C$). The lack of plateau in the curves suggests that we are not in a fully paramagnetic regime.

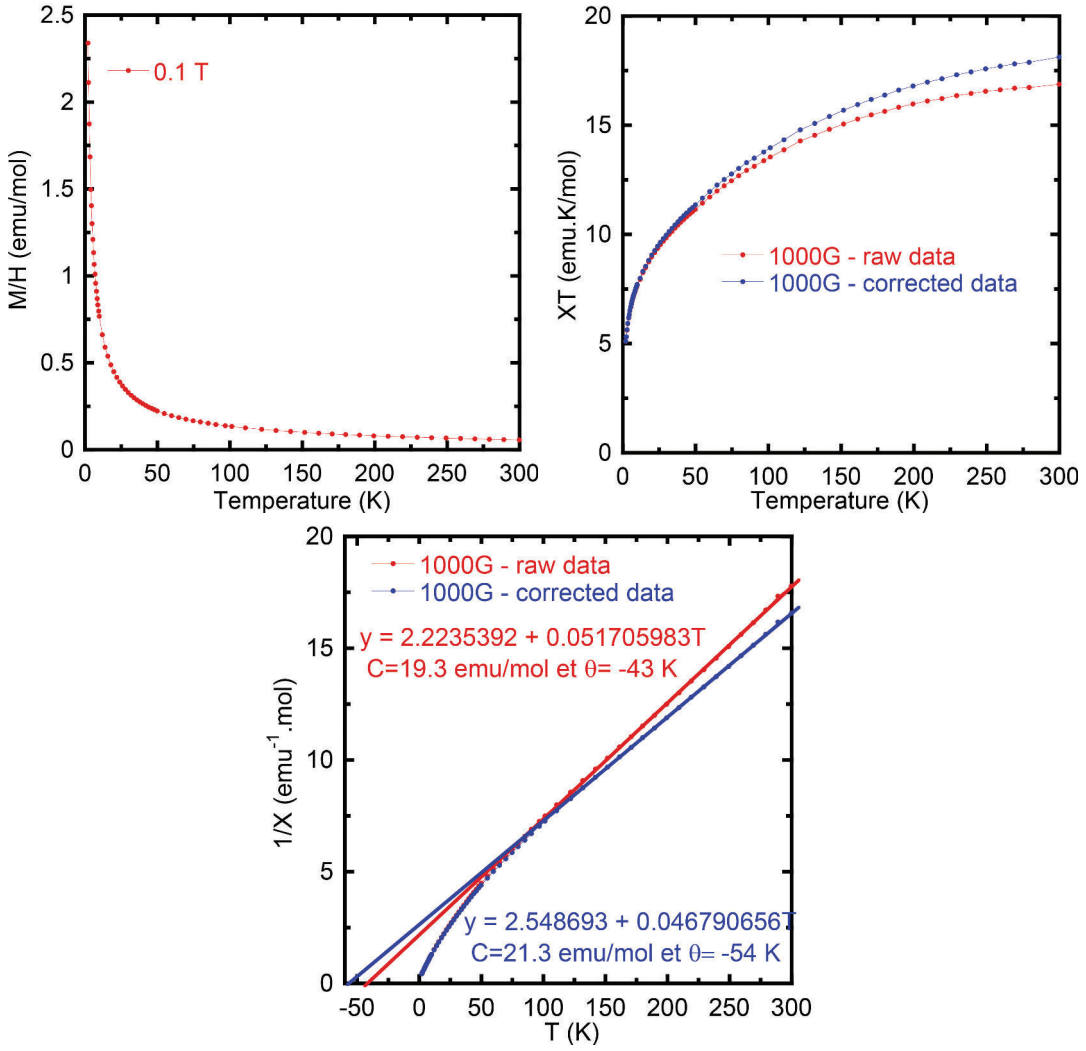

FIGURE 6.4: a) M/H vs T at 0.1 T. b) χT vs T for the raw and corrected data. Corrected data are the results after subtracting the diamagnetic components of the organic compounds and the cellophane used for the measurement. c) $1/\chi$ vs T and the corresponding Curie-Weiss constants and temperature, θ, for the raw and corrected data.

Below 100 K, a quick drop of χT is observed, which suggests the development of antiferromagnetic interactions between spins.

Figure 6.4 c) shows the inverse susceptibility as a function of temperature for the raw and corrected data as well as the corresponding Curie-Weiss law fits. We fitted $1/\chi$ vs T between 100 and 300 K and we obtained a Curie constant of 19 emu.K/mol for the raw data and 21 emu.K/mol for the corrected data. The Curie-Weiss temperature is θ = - 50 K and θ = - 40 K for the corrected, and the raw data respectively, which are consistent with development of antiferromagnetic interactions in the system. The difference between our results and the results of

our collaborators might come from an error in weighing the sample mass or from impurity in the sample or the magnetometer.

Figure 6.5 shows the isothermal magnetization measurements for several tem-

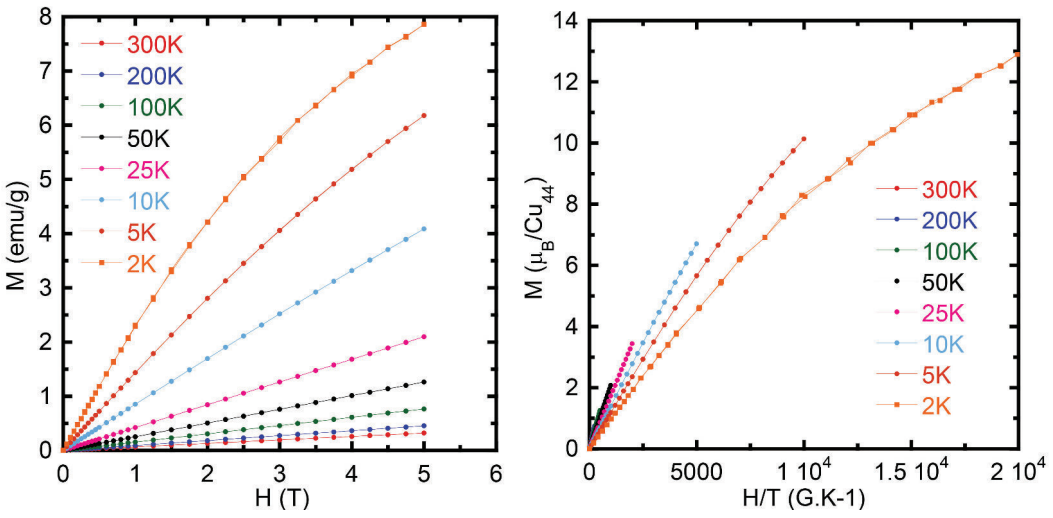

FIGURE 6.5: Left: M vs H for several temperatures. Right: M vs H/T for several temperatures.

peratures between 300 and 2 K. Down to 10 K, there is a linear behavior for a magnetic field up to 5 T. No saturation is reached, in the available field range. In order to better characterize the behavior of the sample (see figure 6.5 right), the magnetization is plotted as a function of H/T. Its use can be understood if the Brillouin function, $B_j(x)$, is introduced

$$M = NgJ\mu_B B_j(x) \tag{6.1}$$

$$x = \frac{gJ\mu_B H}{kT} \tag{6.2}$$

$$B_j(x) = \frac{2J+1}{J}\coth\left(\frac{(2J+1)x}{2J}\right) \quad \frac{1}{2J}\coth\left(\frac{x}{2J}\right) \tag{6.3}$$

where N is the number of atoms per volume, g is the Landé factor, μ_B is the Bohr magneton, x is the ratio of the Zeeman energy of the moment in the external field to the thermal energy k_BT, k_B is the Boltzmann constant and J is the total angular momentum quantum number.

It can easily be seen that if we plot M as a function of H/T, a linear behavior is expected in the regime of large temperature and small applied magnetic field values. In the paramagnetic regime, where the magnetization obeys the Brillouin law, the magnetization depends only on H/T, so that all the magnetization curves

plotted as a function of H/T are superimposed on each other. It will not be true in presence of magnetic interactions. In this case, in the molecular field approximation, x has to be rewritten

$$x = \frac{gJ\mu_B(H + H_m)}{kT} \tag{6.4}$$

where H_m is the molecular field whose sign depends on the nature of the interactions: positive ($H_m > 0$) and negative ($H_m < 0$) for ferromagnetic and antiferromagnetic interactions respectively. It results that when M is plotted as a function of H/T, the magnetic curves are above, respectively below, the paramagnetic ones in the case of ferromagnetic interactions and antiferromagnetic interactions respectively. These effects become relevant when the energy of the interactions are comparable to the temperature, so that magnetic correlations develop. This is the case in our sample below 100 K, where we observe that antiferromagnetic correlations establish which is consistent with the $1/\chi$ analysis.

6.2.2 Low temperature magnetization measurements

The low temperature magnetization measurements were performed using the low temperature SQUID magnetometer described in section 2.1.5. A 5 mg polycrystalline sample wrapped in a copper pouch with Apiezon N grease for thermalization, was measured in a magnetic field up to 8 T between 70 mK and 5 K.

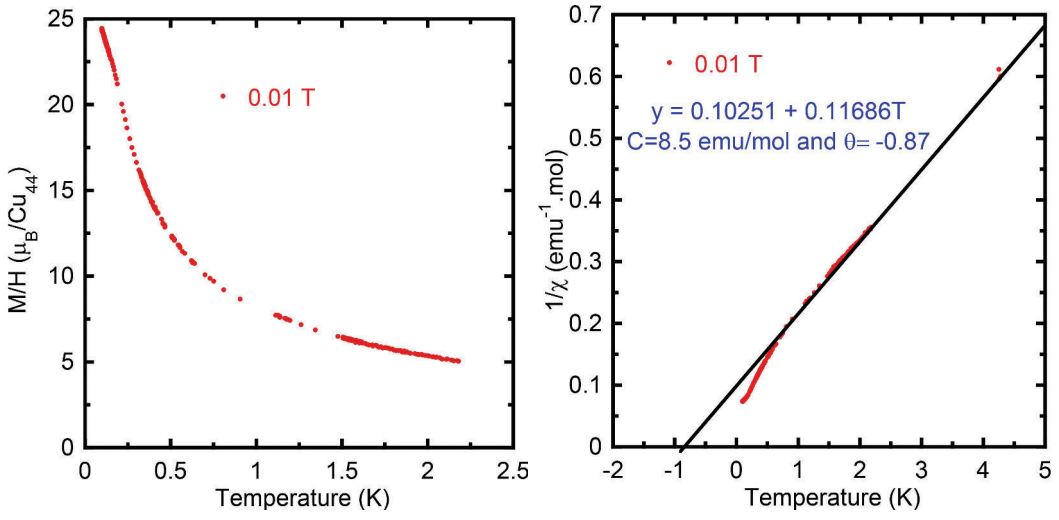

FIGURE 6.6: Left: M/H vs T at 0.01 T. Right: $1/\chi$ vs T at 0.01 T and the corresponding Curie-Weiss fit.

We measured the magnetization of the sample when cooling down from 4 K to 70 mK. We can make a linear fit of $1/\chi$ vs T between 1 and 4 K (see figure 6.6 right). Assuming a Curie-Weiss behavior, it would lead to a Curie constant of 8.5 emu.K/mol and a Curie-Weiss temperature, θ of -0.87 K. At this temperature, we assume that the spins inside the clusters are correlated. Changing equation (4.3) to get the effective moment μ_{eff} of these clusters, we get:

$$C = \frac{g^2\mu_B^2}{3k_B} N_A \cdot \mu_{eff}^2 \tag{6.5}$$

Our low temperature Curie constant is consistent with an effective moment of 4 μ_B. This suggests that the intra-cluster correlations are not fully antiferromagnetic, since in that case we would expect a zero effective moment, with a susceptibility which drops to zero.

We can also extract information from the low temperature Curie-Weiss constant. Assuming that the clusters behave like macro spins at these low temperatures, if the value of the Curie temperature is not zero, it means that interactions occur between clusters and the sign of this temperature will give us the nature of these interactions. Therefore, the obtained value θ = - 0.87 K, is due to interactions between clusters which, as awaited, appears to be more than one order of magnitude weaker than the interactions characterizing the high temperature behavior which are implicitly assumed, intra-molecular. Its sign suggests antiferromagnetic interactions between the clusters. Nevertheless, below 500 mK, $1/\chi$ deviates from the Curie-Weiss law, and becomes larger, suggesting that additional ferromagnetic interactions are at play in the system.

Below 800 mK, we performed zero field cooled - field cooled measurements (ZFC-FC) at several applied magnetic fields. The results presented in figure 6.7 left, display an irreversibility between the ZFC and FC which occurs below 110 mK. The suggested spin freezing is lifted by increasing the applied magnetic field, disappearing for $H > 0.05$ T.

In figure 6.7 right I present the isothermal magnetization measurements between 70 mK and for applied magnetic fields up to 8 T. Unfortunately, no steps in magnetization curve were observed down to the lowest temperature achievable. In addition, no upturn in the magnetic isotherms is observed. This may suggest that i) we are not at low enough temperature to access the energy spectrum of this

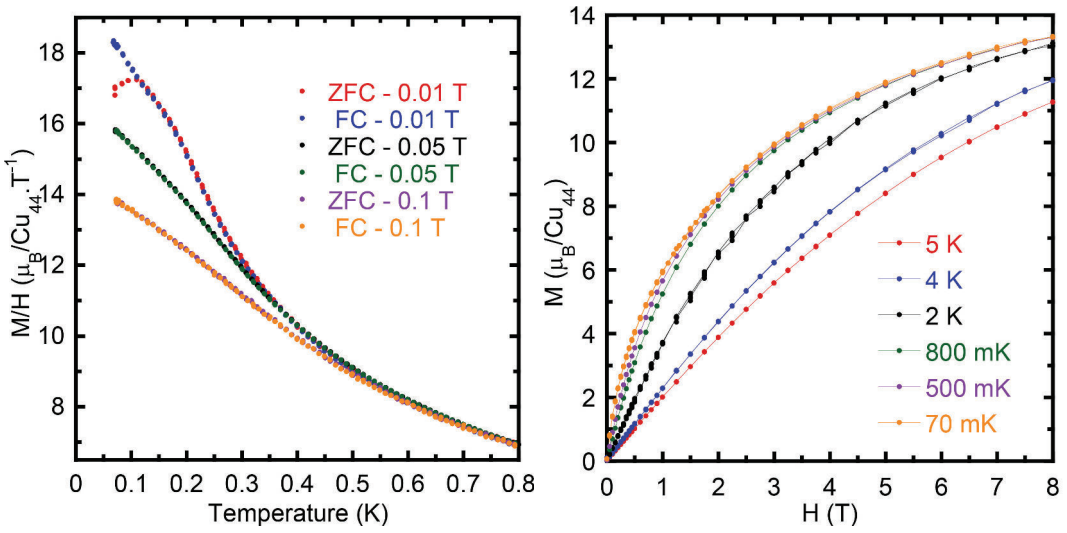

FIGURE 6.7: Left: ZFC-FC measurements for several applied magnetic fields. Right: M vs H for several temperatures.

molecule (the number of excited states is expected to be huge due to the large number of spins) ii) the correlations between the clusters broaden and/or modify the energy spectrum of the clusters, and mask the physics we aimed to probe.

6.2.3 Conclusion

In short, intracluster antiferromagnetic correlations develop in the molecule below 100 K, and stabilize an intracluster effective moment of about 4 μ_B at low temperature. We have shown that antiferromagnetic correlations exist between the clusters at low temperature, but no sign of long range ordering was observed. An irreversibility of the ZFC-FC protocol suggests a freezing of the spins.

No irregular steps or upturn of the magnetization curvature as a function of applied magnetic field is seen, suggesting a weak geometric frustrated effect, if any in the compound.

The complex magnetic behavior and the complexity of the structure make difficult theoretical simulations to get a deeper understanding, we thus decided to focus on another quantum molecular magnet, made of frustrated triangles arranged on a kagome lattice with alternating strong and weak exchange interactions. It is an experimental prototype of the theoretical intra-triangle / inter-triangle model used

in the perturbative approaches of the quantum kagome spin physics. The possibility to change copper with iron ions, might provide evidence of the quantum effects on the quantum system (Cu_3) compared to the classical one (Fe_3).

6.3 Cu_3 molecular magnet

The second frustrated system provided by our collaborators from Karlsruhe is $\{Cu_3Cs(\mu \quad Cl)_3(Hntp)_2(H2O)_3\}_\infty$, or Cu_3. It is an example of a 2D system with a pseudo-kagome lattice as presented in figure 6.8. The copper spins $s = 1/2$,

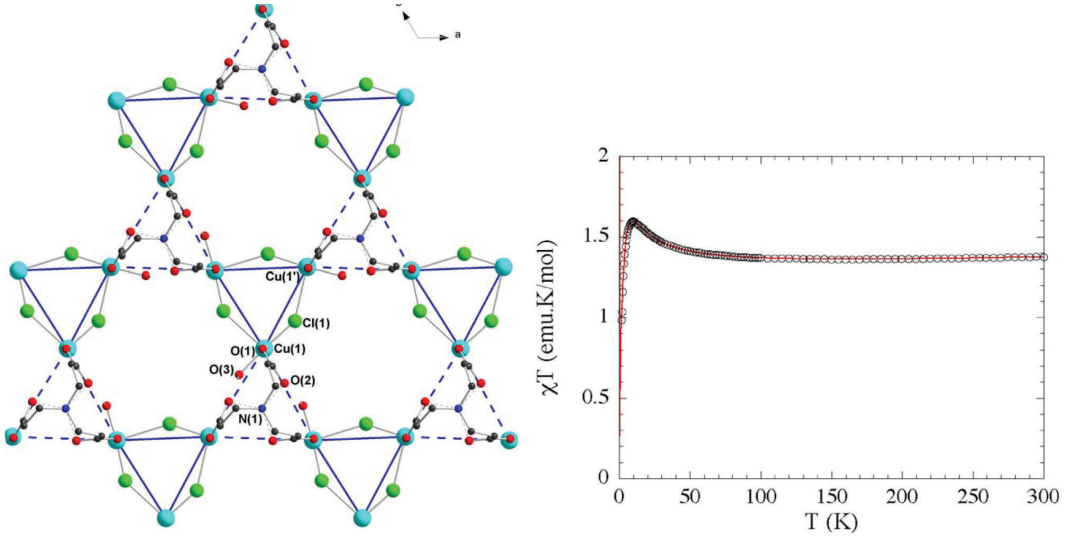

FIGURE 6.8: Muguresu et al.[90] : Left : 2D pseudo-kagome lattice in Cu_3 aggregate. Right: temperature dependence of χT and $1/\chi$ at 0.1 T (solid circles are the experimental data, red thick line is the fit obtained for a triangles with ferromagnetic interactions and weak antiferromagnetic inter-triangles interactions.)

lies on the corners of a triangle with strong intra-triangle interactions and weak inter-triangle interactions. The final structure of the aggregate is a triangular lattice of triangles of 1/2 copper spins.

A first characterization of the system is provided by our collaborators [90]. χT as a function of temperature at 0.1 T is presented in figure 6.8 right. It is constant between 300 and 100 K and then increases, reaching a maximum around 10 K, and finally decreases at low temperatures. To understand this behavior, they used a model with ferromagnetic interactions in each triangle (with a total spin 3/2) and weak antiferromagnetic interactions between triangles of spin 3/2. The thick red

line in figure 6.8 is the fit using $g = 2.14$ and $J/k_B = 5.8$ K and $J'/k_B =$ 0.9 K, where J is the intra-triangle ferromagnetic exchange interaction and J' is the inter-triangle antiferromagnetic exchange interaction.

6.4 First low temperature magnetic characterization

150 mg of Cu_3 powder were provided and from this, samples were prepared for measurements on several distinct magnetometers. The high temperature magnetometers being unavailable at the moment where we received the sample, I performed the first measurements on the low temperature SQUID magnetometer. I took 11 mg out of the sample (sample 1) and wrapped in a copper pouch with Apiezon N grease for thermalization. As we will see below, because the sample experienced aging problems, I will specify the time at which experiments were performed.

Magnetization measurements in a magnetic field up to 8 T between 100 mK and 2 K displayed in figure 6.9 were performed 3 days after we received the sample. The development of a field induced transition is observed below 2 K. Below 500

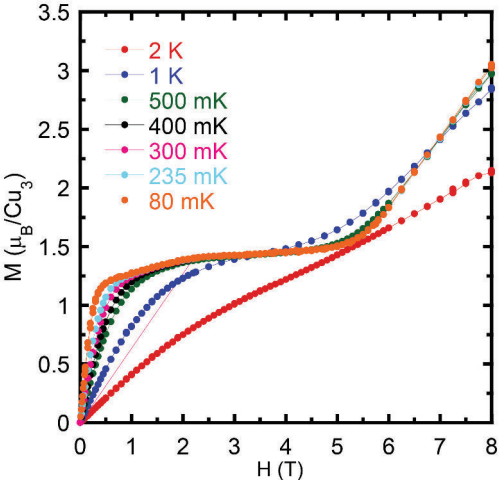

FIGURE 6.9: Very low temperature SQUID magnetometer: M vs H at several temperatures between 100 mK and 2 K and in applied magnetic fields up to 8 T.

mK, a clear plateau develops between $\sim$ 2 and 5.5 T at 1.3 μ_B/fu.

No saturation is observed in the field range of our measurements, thus no clear

conclusion can be extracted from the value of the plateau. As described above, at low temperature, the system is made of trimers (or macro spins) with a spin 3/2 in antiferromagnetic interactions arranged on a triangular lattice. Therefore a plateau at 1/3 of the saturated magnetization is expected. Here, the value of the saturated magnetization is expected to be 3.4 μ_B (if we use the g factor used in the high temperature fit). The value of the magnetization on the plateau is thus above the expected value, but from the curve, the value the magnetization is going to reach seems also to be above.

Having doubts on the absolute value of the plateau (especially because no saturation was reached up to 8 T), we decided to perform magnetization measurements on the high temperature SQUID magnetometers to characterize the sample from room temperature and compare the results with the low temperature SQUID magnetometer.
This case illustrates the need for of a magnetometer able to perform absolute values of magnetization measurements with a high sensitivity up to high applied magnetic fields. If we believe the plateau is a 1/3 of the saturated magnetization, we can estimate that an applied field of $\sim$ 10 T should be enough for this compound to be saturated.

6.4.1 High temperature magnetic characterization

Out of the original sample, $\sim$ 111 mg (sample 2) were put into a recipient for high temperature magnetization measurements using an extraction magnetometer. Due to technical problems on the high temperature magnetometers, I was able to perform the measurements at high temperature only $\sim$ one month after we received the sample.

The first magnetization measurements as a function of applied field at 300 K displayed an anomaly at low fields (see figure 6.10). A linear behavior of the magnetization as a function of applied magnetic field is observed up to 1 T, with a change of the slope at this field and another linear behavior for $1 < H < 10$ T. The anomaly persists down to 50 K. Due to this low field anomaly, we did not perform magnetization measurements as a function of temperature, which would have been very hard to analyze.

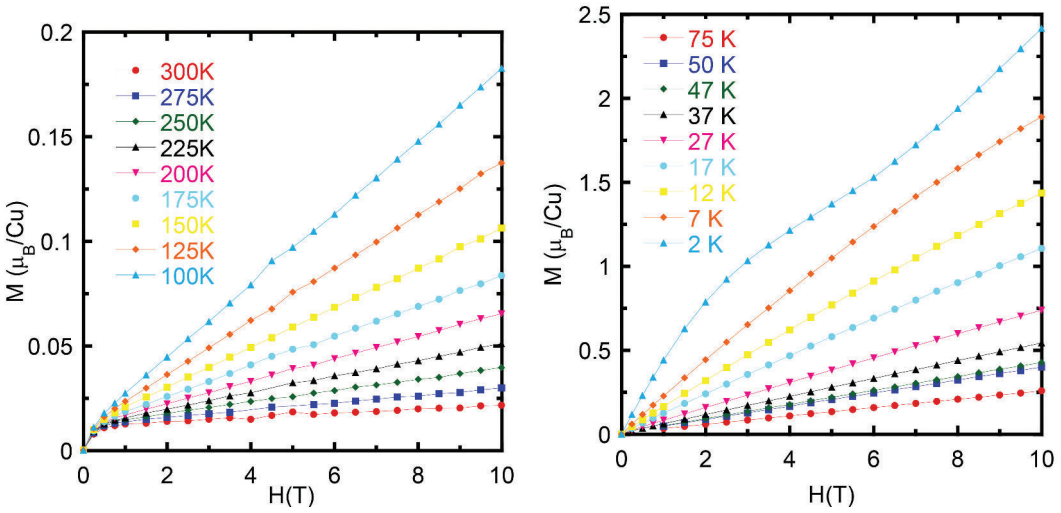

FIGURE 6.10: Extraction magnetometer: M vs H at several temperatures between 2 and 300 K and in applied magnetic fields up to 10 T.

The first thought was that an impurity either in the sample, or in the magnetometer is at the origin of the low field effect. Supposing the magnetization of the sample is linear for temperatures larger than 100 K, we subtracted the linear part for $H > 2$ T, to obtain the "impurity" signal (see figure 6.11). The impurity seems

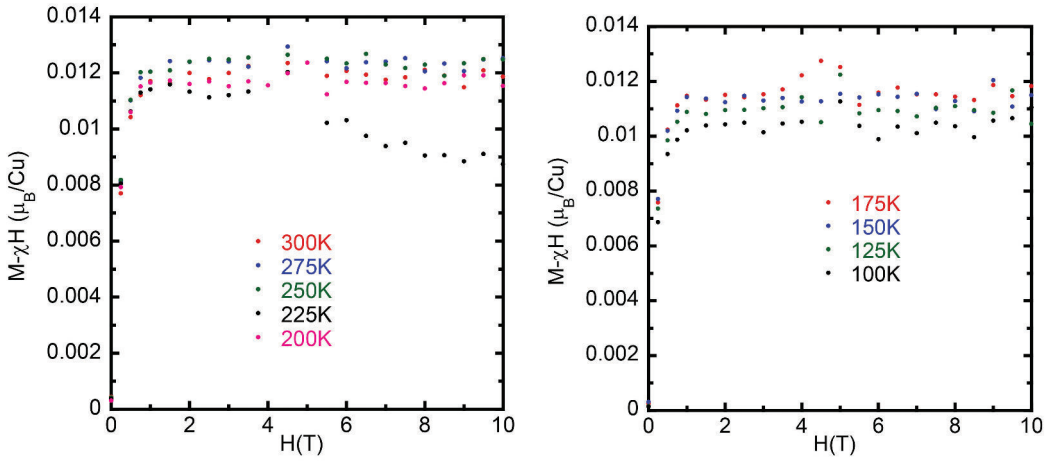

FIGURE 6.11: Extraction magnetometer: $M \quad \chi H$ vs H at several temperatures between 100 and 300 K and in applied magnetic fields up to 10 T.

to have a saturated magnetization of about 0.012 μ_B and is almost temperature independent.

Despite this impurity, it is interesting to look at measurements below 50 K (See figure 6.10 right). At these temperatures, the low field anomaly is small compared

to the signal of the sample. Down to 10 K, the curves are almost linear. But at 2 K, we recover a field induced transition between 2 and 5.5 T. Nevertheless, the shape of the curve is different from the measurements on the low temperature magnetometer, and the curves could not be rescaled to superimpose on each other.

A second experimental test was performed on a VSM SQUID magnetometer to determine if the impurity comes from the sample or from the extraction magnetometer. The measurements were performed approximately two months after the first experiment.

Out of sample 2, we took 21 mg (sample 2a) and wrapped it in plastic for the VSM measurements. Figure 6.12 displays the field dependence measurements for tem-

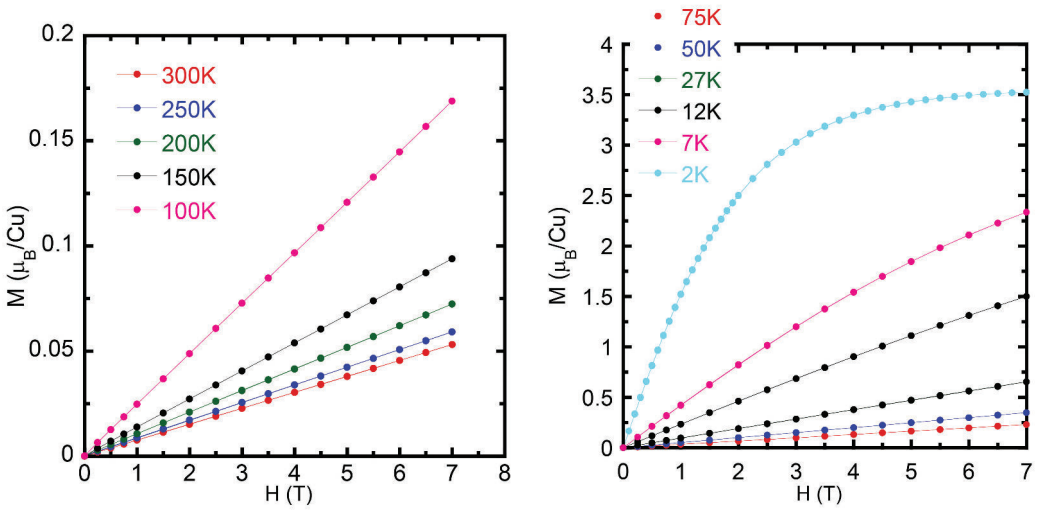

FIGURE 6.12: VSM SQUID magnetometer: M vs H at several temperatures between 2 and 300 K and in applied magnetic fields up to 7 T.

peratures between 2 and 300 K in applied magnetic fields up to 7 T. No anomaly is observed in the low field region and a linear behavior is displayed between 12 and 300 K, thus suggesting that the impurity was not intrinsic to the sample.

But, unfortunately, the field induced transition seen on the extraction magnetometer is not observed anymore. A reason might be that the slope change is small around 2 T at 2 K, and the actual temperature of the sample in the VSM experiment can be larger because of the heating effect due to fast moving during the measurement. With a behavior which seems different in both magnetometers, no clear conclusion arises.

6.4.2 Second low temperature magnetization measurements

In the VSM SQUID magnetometer we observed the lack of field induced transition at 2 K, and apart from the temperature which can be larger than the one displayed by the thermometer, another reason can be the instability of the sample. To test this hypothesis and observe the sample evolution, we performed a second round of test (approximately 2.5 months after the first measurements) using the exactly same sample. The results are displayed in figure 6.13. They show a difference

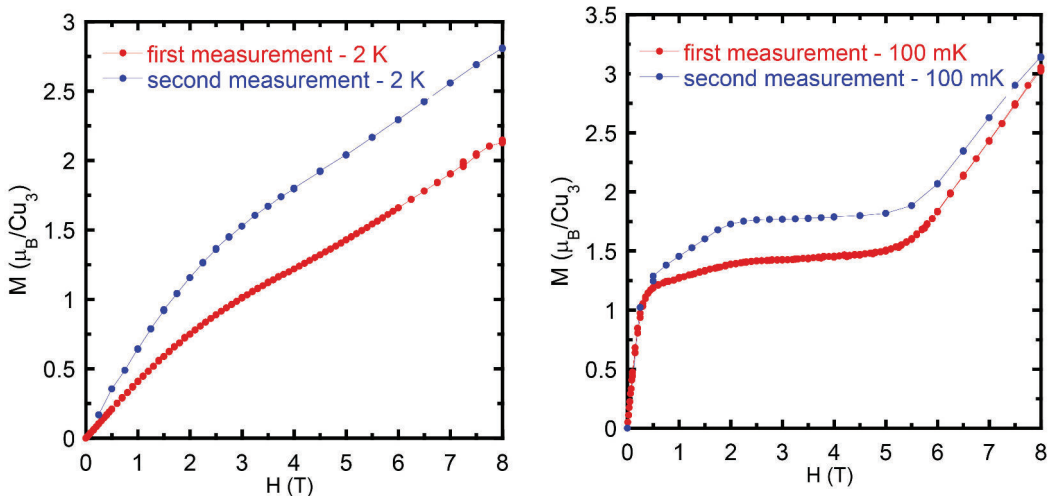

FIGURE 6.13: Very low temperature SQUID magnetometer: M vs H at 100 mK and 2 K and in applied magnetic fields up to 8 T.

between the measurements at both temperatures. At 2 K, the field induced phase is almost vanished. At the lowest temperature, 100 mK, we observe a shift in the amplitude and in the form of the plateau.

These observations indicate that the sample has strongly deteriorated. A possibility is that a part of the sample has turned into another compound with no antiferromagnetic interactions. In that case, the sample would be inhomogeneous, with domains that consist of the Cu_3 compound and exhibit the 1/3 plateau, mixed with another variety which is more easily magnetized.

6.4.3 Conclusions

As a conclusion, magnetization measurements were performed on a Cu_3 powder sample using different magnetometers. The first low temperature measurements

were performed a few days after the sample was received with the last measurements approximately two months after.
A metamagnetic transition develops around 2 K, which becomes a large plateau in the magnetization for temperatures below 1 K. The absolute value of the plateau, as well as the lack of saturation up to 3 μ_B/formula (expected saturated magnetization), were the first indication of possible problems in the compound. Different results were observed when performing magnetization measurement on two high temperatures magnetometers ($2 < T < 300$ K). With inconclusive results after low and high temperatures measurements, a second low temperature measurement was performed on the same sample (approximately two months after the first measurement). The transition at 2 K has almost vanished and a shift of the plateau to larger values is observed at 100 mK. The existence of the plateau and the feature below 2 T at the lowest temperature, might suggest that only a part of the sample is deteriorated. The samples have been sent back to the chemists who had performed the synthesis for a careful composition analysis, but we do not have the results yet.

As a perspective, Cu_3 is an interesting compound to study the triangular lattice with the extend to study the kagome lattice with alternative exchange interactions. The study of magnetic plateaus due to quantum frustration effects is possible, however, precautions in manipulating the sample is required. Unfortunately, no clear response from the chemists is provided so far, therefore no further investigation was conducted.

Chapter 7

Conclusions

The second part of my thesis was dedicated to the low temperature magnetic study of frustrated magnets, and addressed both classical and quantum systems.

First, I presented a complete low temperature study on the classical frustrated magnet, $Gd_3Ga_5O_{12}$ (GGG), which lies in the family of gallium garnets. In this compound, the rare-earth element *Gd* is placed on a hyperkagome lattice, which is made of triangles connected via their corners in three dimensions.
This compound has been studied for several decades already, but the very low temperature behavior is still not fully understood. We have performed a systematic study of the low temperature magnetization as a function of magnetic field and temperature, with the applied magnetic field along the [110] crystallographic direction (magnetization measurements had not been reported along this direction before).
Previous studies showed different results between neutron scattering and magnetic measurements. For this reason, we performed magnetic measurements and neutron scattering on the same ^{160}Gd isotope GGG powder. By correlating measurements on a powder (neutron scattering and magnetic measurements) and a single crystal (magnetic measurements), we could determine a refined $H \quad T$ phase diagram [75]. Our measurements recover the short range correlations previously reported down to very low temperature, and the existence of a field induced antiferromagnetic phase. In addition, our study reveals a much more complicated behavior in the field induced phase, as well as in the short range ordered regime. The phase diagram we propose presents several phase boundaries which converge to a sort of "critical" point at 0.9 K and $\sim$ 0.3 K.

To better understand the origin of the complicated H T phase diagram of GGG, we were interested in studying the isomorphous compound $Gd_3Al_5O_{12}$ (GAG). In this compound, Gd ions lie on the same hyperkagome lattice, but the distance between them is smaller. Studying the magnetic phase diagram of GAG thus allows to test the robustness of the magnetic state of GGG.
I reported the first low temperature magnetic study on GAG, performed on a powder sample. We show that GAG shows a similar magnetic behavior as GGG. We observe antiferromagnetic correlations as previously reported [79, 80], but no clear signature of an antiferromagnetic transition is found down to 100 mK. We recover the field induced antiferromagnetic phase and several phase boundaries discovered in GGG. In the same manner as in GGG, all these phases seem to converge to a single point in the H T phase diagram.

The reasons for such complex behavior, with the coexistence of ordered and disordered phases are not solved yet. In addition, the convergence of all these phases to a kind of critical point in both samples, is very interesting. The analysis of the neutron scattering data which is in progress and further studies on a GAG single crystal might elucidate some of the unanswered questions.

After studying this unconventional behavior in classical frustrated materials, I further focused on the study of quantum frustrated molecular magnets, to probe the relation between quantum effects and frustration. The objective was to evidence quantum properties induced by frustration in copper molecular clusters, which have been synthesized in Karlsruhe in collaboration with A. K. Powell. In these clusters, the copper ions carry a spin 1/2 and are coupled by antiferromagnetic interactions in frustrated geometries, such as triangles or tetrahedra.

The main idea was to use the high sensitive Faraday magnetometer to access the excitations spectrum of these compounds through the field induced Zeeman crossings of spin excitation energy levels. Then, exact computations of these states and excitations can be foreseen.
I presented preliminary results on two compounds, performed with the existent magnetometers at Néel Institute, down to 70 mK: i) the Cu_{44} cluster (formula $[Cu_{44}(\mu_8\text{-}Br)_2\text{-}(\mu_3\text{-}OH)_{36}(\mu\text{-}OH)_4(ntp)_12Br_8(OH_2)_{28}]Br_2 \cdot 81H_2O$ [89] which is made of tetrahedra, and ii) Cu_3 clusters (formula $\{Cu_3Cs(\mu\text{-}Cl)_3(Hntp)_2(H2O)_3\}_\infty$ [90] which are made of frustrated triangles and are arranged on a kagome lattice, with alternating strong and weak exchange interactions.

In Cu_{44}, intracluster antiferromagnetic correlations develop in the molecule below 100 K, and stabilize an intracluster effective moment of about 4 μ_B at low temperature. We have shown that antiferromagnetic correlations exist between the clusters at low temperature, but no sign of long range ordering was observed. No irregular steps or upturn of the magnetization curvature as a function of applied magnetic field is seen, which would have been a signature of frustration in thus compound. This suggests the absence of visible effect of geometric frustration, if any in the compound. Unfortunately, the complex magnetic behavior and the complexity of the structure make difficult theoretical simulations to get a deeper understanding.

In Cu_3, a preliminary study was performed by our collaborators from Karlsruhe. To understand this behavior, they used a model with ferromagnetic interactions in each triangle (with a total spin 3/2) and weak antiferromagnetic interactions between triangles of spin 3/2. Our study could evidence the development of a field induced transition around 2 K, which becomes a large plateau in the magnetization for temperatures below 1 K. Unfortunately, the sample was not stable over time. Measurements performed two months after we received the sample showed that the transition at 2 K has almost vanished and a shift of the plateau to larger values was observed at the lowest temperatures, which prevented us from making quantitative analysis of our results.

Although these studies on molecular magnets did not provide the expected results, they have shown that molecular magnets are promising systems to approach the question of frustration in quantum systems.

Part III

Conclusions

I have presented in this manuscript the present stage of the development of a Faraday force magnetometer which we expect to see soon operating at very low temperatures (30 mK) and high applied magnetic fields (16 T) with a high sensitivity (10 ^{5} emu).

A standard ^{3}He-^{4}He dilution fridge was designed and built at Néel Institute. Its characterization is presented. At first, a base temperature of 45 mK with a cooling power of 20 μW at 100 mK was reached. Unfortunately, the dilution refrigerator operating conditions degraded in time. Several unsuccessfully tests to find the origin of this effect were presented. One of the problem found is the existence of vibrations in the lower part of the dilution refrigerator, which could not be solved due to the design of the fridge. A second dilution refrigerator was recently designed and built, but it was not characterized due to lack of time.

The Faraday magnetometer uses the capacitive detection method, proved to be suitable at very low temperatures and high applied magnetic fields. Two sample holders were developed for this magnetometer. A nanofabricated microelectromechanical system (MEMS membrane) and a second second sample holder, made of insulating material (plastic sample holder). We encountered problems in the technological process of the MEMS and we have received operational membranes only recently, but tests with the plastic sample holders allowed to approve our electronic detection.

A cold amplifier stage was developed with the aim of increasing the sensitivity of the measurement. The measurements in the absence of the applied magnetic field, resulted in a sensitivity of $\Delta C/C_0 = 10^{-5}$, which is consistent with a sensitivity of 10 ^{7} A.m^2 (10 ^{4} emu). Unfortunately, problems were encountered when tests under applied field were conducted. Two problems were identified: i) The vibrations mentioned above interfere with the sensitive capacitive measurement. ii) The sensor was shifted of about 4 cm from the magnetic field homogeneity area of the main coil. Therefore, the magnetic samples were in the field gradient of the main coil, leading to false measurements.

This thesis project was initially targeted to the use of the Faraday magnetometer to probe the effects of magnetic frustration in quantum molecular magnets. Due to the encountered problems in the construction of this magnetometer, we have focused on the study of magnetic frustrated systems by magnetization measurements, using the existent magnetometers at Néel Institute.

The first compound we describe in this manuscript is a classical frustrated magnet, $Gd_3Ga_5O_{12}$ (GGG). Our study complements the low temperature magnetization study reported in the literature by providing additional data with the applied magnetic field along the [110] crystallographic direction. A refined H T phase diagram has been deduced which, compared to previous work, highlighted the presence of several phase boundaries in the short range ordered phase and field induced antiferromagnetic phase present in the compound.

To further understand the complicated behavior of GGG, a magnetic study was performed on the isomorphous compound, $Gd_3Al_5O_{12}$ (GAG). This was conducted on a powder sample. It revealed a magnetic behavior similar to the one in GGG. It is rare to find compounds which exhibit the extremely complex H T phase diagram of GGG. In addition, the convergence of all the observed phases, those reported in literature which we have confirmed as well as those we have found out, to a "critical" point in both samples, is appealing. The full analysis of the neutron scattering data is in progress to get a deeper insight in the zero field properties of this compound. In addition, further studies on a GAG single crystal are required to quantitatively compare the GGG and GAG phase diagram, and solve some unanswered questions.

We next focused on the study of frustration effects in molecular magnets where the quantum nature of the magnetic moments cannot be ignored. The first compound (formula $[Cu_{44}(\mu_8\text{-}Br)_2\text{-}(\mu_3\text{-}OH)_{36}(\mu\text{-}OH)_4(ntp)_12Br_8(OH_2)_{28}]Br_2 \cdot 81H_2O$), containing Cu_{44} clusters with tetrahedral motives, proved to display a complex magnetic behavior. Owing to the number of quantum spins S=1/2 in each Cu_{44} cluster, the large number of exchange interactions and the apparent absence of hierarchy in these exchange interactions, no numerical analysis can be reasonably worked out to get a deeper understanding.

The second compound, $\{Cu_3Cs(\mu\text{-}Cl)_3(Hntp)_2(H_2O)_3\}_\infty$, containing planar triangular network of Cu triangles, with strong intra-triangle ferromagnetic interactions and weak inter-triangular antiferromagnetic interactions displayed a magnetization plateau at low temperatures, below 1 K. Unfortunately, chemical instability induced the degradation of the magnetic signal, so that the value of the magnetization plateau could not be determined accurately. However, the preliminary results are very promising and a stable compound is awaited from the chemists.

Although the magnetometer is still not operational, I have acquired a lot of skills during these three years. Working closely with the cryogenic and electronic departments, I had the opportunity to learn from experts in these domains. Therefore, I have acquired a better understanding on how dilution refrigerator operates. Facing a lot of problems, forced me to look and find solutions, thus acquiring experience, that otherwise would have been impossible. I am confident that we are not far from making the magnetometer working. Unfortunately, my time for this project is limited, and soon coming to an end, but I believe that the work provided in this thesis will allow this magnetometer to operate within a short delay.

It was a challenge for me to try to develop the Faraday magnetometer and in the same time to find answers raised by magnetic frustrated systems. However, I was able to overcome most of the encountered problems with the help of my supervisor, collaborators and not lastly several scientist researchers at Néel Institute. During my thesis, I had the opportunity to work on the fascinating domain of magnetic frustration, and I am looking forward to improve my knowledge on the subject, especially on the quantum part. In addition, these experimental studies allowed me to further improve my knowledge on very low temperature magnetization measurements.

Bibliography

[1] T. Sakakibara, H. Mitamuraa, T. Tayama, and H. Amitsuka. *Japanese Journal of Applied Physics*, 33:5067–5072, 1994.

[2] D. Slobinsky, R. A. Borzi, A. P. Mackenzie, and S. A. Grigera. *Review of Scientific Instruments*, 83:125104, 2012.

[3] F. London. *Proceedings of the International Conference on Low Temperature Physics: Oxford*, page 157, 1951.

[4] P. Das, R. De Bruyn Ouboter, and K.W. Taconis. *Proceedings of the International Conference on Low Temperature Physics: London*, page 1253, 1965.

[5] F. Pobell. Matter and methods at low temperatures. *Springer Science Media*, 1996.

[6] E. Lennon. *Thesis*, 2003.

[7] Commercial capacitance bridge: Ah 2550a. *Technical manual*. URL http://www.andeen-hagerling.com/ah2550a.htm.

[8] V. Simonet. *Private communication*.

[9] Michael Fowler. Historical beginnings of theories of electricity and magnetism. *University of Virginia, Physics*, 1997.

[10] Shen Kuo. The dream pool essays. 1088.

[11] C. Paulsen. Introduction to physical techniques in molecular magnetism: Structural and macroscopic techniques - yesa 1999, edited by f. palacio, e. ressouche and j. schweizer. *Servicio de Publicaciones de la Universidad de Zaragoza*, page 1, 2001.

[12] M. McElfresh. Fundamentals of magnetism and magnetic measurements. featuring quantum design magnetic property measurement system. 1994.

[13] J. Chadwick. *Nature*, 139:312, 1932.

[14] B. Grenier. *Cours de DEA : Diffusion neutronique. CEA, Grenoble*, page 312, 2003-2004.

[15] M. Blume. *Physical Review*, 130:1670, 1963.

[16] S.V.Maleyev. *Soviet Journal of Experimental and Theoretical Physics*, 14: 1168, 1961.

[17] R. M. Moon, T. Riste, and W. C. Koehler. *Physical Review*, 181:920, 1969.

[18] G. Toulouse. *Communications on Physics*, 2:115, 1977.

[19] P. Chandra and B. Doucot. *Physical Review B*, 38:9335, 1988.

[20] W. F. Giauque and M. F. Ashley. *Physical Review*, page 81.

[21] L. Pauling. *Journal of the American Chemical Society*, 57:12, 1935.

[22] J. D. Bernal and R. H. Fowler. *The Journal of Chemical Physics*, 1:515, 1933.

[23] M. J. Harris, S. T. Bramwell, D. F. McMorrow, T. Zeiske, and K. W. Godfrey. *Physical Review Letters*, 79:2554, 1997.

[24] A. P. Ramirez, A. Hayashi, R. J. Cava, R. Siddharthan, and B. S. Shastry. *Nature*, 399:333–335, 1999.

[25] K. Binder and A. P. Young. *Reviews of Modern Physics*, 58:801, 1986.

[26] M. A. Ruderman and C. Kittel. *Physical Review*, 96:99, 1954.

[27] K. Yosida. *Physical Review*, 106:893, 1957.

[28] T. Kasuya. *Progress of Theoretical Physics*, 1956.

[29] V. Cannella and J. A. Mydosh. *Physical Review B*, 6:4220, December 1972.

[30] J. Souletie and J. L. Tholence. *Physical Review B*, 32(1):516, 1985.

[31] F. Lefloch, J. Hammann, M. Ocio, and E. Vincent. *Europhysics Letters*, 18: 647–652, 1992.

[32] I. Ritchey, P. Chandra, and P. Coleman. *Physical Review B*, 91:10, 1993.

[33] P. Chandra, P. Coleman, and I. Ritchey. *Journal Physique francaise*, 3:591–610, 1993.

[34] M. J. P. Gingras, C. V. Stager, B. D. Gaulin, N. P. Raju, and J. E. Greedan. *Journal Of Applied Physics*, 79:8, 1996.

[35] A. S. Wills, V. Dupuis, E. Vincent, J. Hammann, and R. Calemczuk. *Physical Review B*, 62:14, 2000.

[36] V. Dupuis, E. Vincent, J. Hammann, J. E. Greedan, and A. S. Wills. *Journal Of Applied Physics*, 91:10, 2002.

[37] G. H. Wannier. *Physical Review*, 79:357, 1950.

[38] J. Villain, R. Bidaux, J.P. Carton, and R. Conte. *Journal Physique*, 41: 1263–1272, 1980.

[39] J. T. Chalker, P. C. W. Holdsworth, and E. F. Shender. *Physical Review Letters*, 68:855, 1992.

[40] M. E. Zhitomirsky. *Physical Review Letters*, 88:057204, 2002.

[41] T. Inami, T. Morimoto, M. Nishiyama, S. Maegawa, Y. Oka, and H. Okumura. *Physical Review B*, 64:054421, 2001.

[42] D. Grohol, K. Matan, J.H. Cho, S.H. Lee, J. W. Lynn, D. G. Nocera, and Y. S. Lee. *Nature*, 4:323–328, 2005.

[43] K. Matan, D. Grohol, D. G. Nocera, T. Yildirim, A. B. Harris, S. H. Lee, S. E. Nagler, and Y. S. Lee. *Physical Review Letters*, 96:247201, 2006.

[44] A. S. Wills and A. Harrison. *Journal of the Chemical Society, Faraday Transactions*, 92:2161–2166, 1996.

[45] B. Fak, F. C. Coomer, A. Harrison, D. Visser, and M. E. Zhitomirsky. *Europhys Letter*, 81:17006, 2008.

[46] S. Yan, D. A. Huse, and S. R. White. *Science*, 332:1173–1176, 2011.

[47] S. Depenbrock, I. P. McCulloch, and U. Schollwöck. *Physical Review Letters*, 109:067201, 2012.

[48] P. Sindzingre and C. Lhuillier. *Europhysics Letters*, 88, 2009.

[49] P. Mendels, F. Bert, M. A. de Vries, A. Olariu, A. Harrison, F. Duc, J. C. Trombe, J. S. Lord, A. Amato, and C. Baines. *Physical Review Letters*, 98: 077204, 2007.

[50] T.H. Han, J. S. Helton, S. Chu, D. G. Nocera, J. A. Rodriguez-Rivera, C. Broholm, and Y. S. Lee. *Nature*, 98:077204, 2012.

[51] J. S. Helton, K. Matan, M. P. Shores, E. A. Nytko, B. M. Bartlett, Y. Yoshida, Y. Takano, A. Suslov, Y. Qiu, J.H. Chung, D. G. Nocera, and Y. S. Lee. *Physical Review Letters*, 98:107204, 2007.

[52] A. Olariu, P. Mendels, F. Bert, F. Duc, J. C. Trombe, M. A. de Vries, and A. Harrison. *Physical Review Letters*, 100:087202, 2008.

[53] A. Zorko, S. Nellutla, J. van Tol, L. C. Brunel, F. Bert, F. Duc, J.C. Trombe, M. A. de Vries, A. Harrison, and P. Mendels. *Physical Review Letters*, 101: 026405, 2008.

[54] C. Lhuillier and G. Misguich. Frustrated quantum magnets. *Conference: International School on High Magnetic Fields Location: Corsica, France*, 2001.

[55] A. Honecker. *Journal of Physics: Condensed Matter*, 11, 2004.

[56] L. E. Svistov, A. I. Smirnov, L. A. Prozorova, O. A. Petrenko, L. N. Demianets, and A. Ya. Shapiro. *Physical Review B*, 67:094434, 2006.

[57] Y. Narumi, K. Katsumata, Z. Honda, J.-C. Domenge, P. Sindzingre, C. Lhuillier, Y. Shimaoka, T. C. Kobayashi, and K. Kindo. *Europhysics Letters*, 65, 2004.

[58] D. G. Onn, H. Meyer, and J. P. Remeika. *Physical Review Letters*, 156:663, 1967.

[59] S. Hov, H. Bratsberg, and A.T. Skjeltorp. *Journal of Magnetism and Magnetic Materials*, 15-18:455–456, 1980.

[60] J. Overmeyer. Paramagnetic resonance. *Academic Press, New York*, chap 15, 1963.

[61] Y. Singh, Y. Tokiwa, J. Dong, and P. Gegenwart. *Physical Review B*, 88: 220413, 2013.

[62] R. Dally, T. Hogan, A. Amato, H. Luetkens, C. Baines, J. Rodriguez-Rivera, M. J. Graf, and S. D. Wilson. *Physical Review Letters*, 113(247601), 2014.

[63] A. C. Shockley, F. Bert, J-C. Orain, Y. Okamoto, and P. Mendels. *Physical Review Letters*, 115(047201), 2015.

[64] W. I. Kinney and W. P. Wolf. *Journal of Applied Physics*, 50:2115–2117, 1979.

[65] P. Schiffer, A. P. Ramirez, D. A. Huse, and A. J. Valentino. *Physical Review Letters*, 73:2500, 1994.

[66] P. Schiffer, A. P. Ramirez, D. A. Huse, P. L. Gammel, U. Yaron, D. J. Bishop, and A. J. Valentino. *Physical Review Letters*, 74:2379, 1995.

[67] O. A. Petrenko, C. Ritter, M. Yethiraj, and D. McK Paul. *Physical Review Letters*, 80:4570, 1998.

[68] O.A. Petrenko, G. Balakrishnan, D. McK Paul, M. Yethiraj, G. J. McIntyre, and A. S. Wills. Field induced magnetic order in the frustrated magnet gadolinium gallium garnet. *Journal of Physics: HFM Conference Series*, 145 (1), May 2008.

[69] S. R. Dunsiger, J. S. Gardner, J. A. Chakhalian, A. L. Cornelius, M. Jaime, R. F. Kiefl, R. Movshovich, W. A. MacFarlane, R. I. Miller, J. E. Sonier, and B. D. Gaulin. *Physical Review Letters*, 85:3504, 2000.

[70] P. Bonville, J. A. Hodges, J. P. Sanchez, and P. Vulliet. *Physical Review Letters*, 96:167202, 2004.

[71] T. Yavors'kii, M. Enjalran, and M. J. P. Gingras. *Physical Review Letters*, 97:267203, 2006.

[72] P. P. Deen, O. A. Petrenko, G. Balakrishnan, B. D. Rainford, C. Ritter, L. Capogna, H. Mutka, and T. Fennell. *Physical Review B*, 82:174408, 2010.

[73] O.A. Petrenko, D. McK Paul, C. Ritter, T. Zeiske, and M. Yethiraj. *Physica B*, 266:41–48, 1999.

[74] N. d'Ambrumenil, O. A. Petrenko, and H. Mutka. *Physical Review B*, 82: 174408, 2010.

[75] P. P. Deen, O. Florea, E. Lhotel, and H. Jacobsen. *Physical Review B*, 91: 014419, 2015.

[76] O. Cépas and B. Canals. *Physical Review B*, 86:024434, 2012.

[77] J. A. M. Paddison, H. Jacobsen, O. A. Petrenko, M. T. Fernández-Díaz, P. P. Deen, and A. L. Goodwin. *Science*, 350:179–181, 2015.

[78] S. Ghosh, T. F. Rosenbaum, and G. Aeppli. *Physical Review Letters*, 101: 157205, 2008.

[79] J. A. Quilliam, S. Meng, H. A. Craig, L. R. Corruccini, G. Balakrishnan, O. A. Petrenko, A. Gomez, S. W. Kycia, M. J. P. Gingras, and J. B. Kycia. *Physical Review B*, 87:174421, 2013.

[80] A. C. Sackville Hamilton, G. I. Lampronti, S. E. Rowley, and S. E. Dutton. *Journal of Physics: Condensed Matter*, 2014.

[81] D. Gatteschi, L. Pardi, A. L. Barra, A. Muller, and J. Döring. *Nature London*, 354:463, 1991.

[82] I. Chiorescu, W. Wernsdorfer, A. Muller, H. Bogge, and B. Barbara. *Physical Review Letters*, 84:3454, 2000.

[83] Y. Furukawa, Y. Nishisaka, K. I. Kumagai, P. Kogerler, and F. Borsa. *Physical Review B*, 75:220402, 2007.

[84] U. Kortz, N. K. Al-Kassem, M. G. Savelieff, N. A. Al Kadi, and M. Sadakane. *Inorganic Chemistry Communication*, 40:4742, 2001.

[85] O. Cador, D. Gatteschi, R. Sessoli, F.K. Larsen, A.-L. Barra J. Overgaad, S. J. Teat, G.A. Timco, and R.E.P. Winpenny. *Angewandte Chemie International Edition*, 43:5196, 2004.

[86] Y. Furukawa, K. Kiuchi, K. Kumagai, Y. Ajiro, Y. Narumi, M. Iwaki, K. Kindo, A. Bianchi, S. Carretta, P. Santini, and F. Borsa. *Physical Review B*, 79:134416, 2009.

[87] J. Schnack. Effects of frustration on magnetic molecules: a survey from olivier kahn until today. *Dalton Transactions*, 39:4677, 2010.

[88] J. Schnack, M. Luban, and R. Modler. *Europhysics Letter*, 56:863–869, 2001.

[89] M. Murugesu, R. Clerac, C. E. Anson, and A. K. Powell. *Inorganic Chemistry Communication*, 43:7269–7271, 2004.

[90] M. Murugesu, R. Clerac, C. E. Ansona, and A. K. Powell. *Journal of Physics and Chemistry of Solids*, 65:667–676, 2004.

List of Figures

List of Tables

Abstract

The objective of this work was to develop a Faraday force magnetometer to measure absolute values of the magnetization at very low temperatures (30 mK) and high applied magnetic fields (16 T) with a high sensitivity (10^{-5} emu). This magnetometer will be especially dedicated to the study of the field induced properties of frustrated magnets.

In a first part, I present the development of this magnetometer. It involves the optimization of the dilution refrigerator and field gradient coils, and the development of a capacitive detection with a cold amplifier stage to improve the measurement sensitivity. Preliminary magnetic measurements are shown. The changes in the design required to make the magnetometer operational are discussed.

In a second part, I focus on experimental studies of frustrated magnets: Gadolinium garnets, described by classical spins, and Copper based frustrated molecular compounds, to probe quantum effects. These measurements were performed from 70 mK to 300 K, with the existing magnetometers at the Institut Néel.

In $Gd_3Ga_5O_{12}$, we have complemented the $H - T$ phase diagram. This phase diagram was proven to be robust by our study on the isomorphous compound, $Gd_3Al_5O_{12}$. We evidence the convergence of all the observed phases to a unique point in both samples. In quantum systems, we performed preliminary studies on Cu_{44} clusters with tetrahedral motives, and on a triangular system Cu_3. Although promising, these studies were not pursued due to sample problems.

Résumé

L'objectif de cette thèse était de développer un magnétomètre à force de Faraday pour mesurer des valeurs absolues de l'aimantation à très basse température (30 mK) et fort champ magnétique (16 T) avec une haute sensibilité (10^{-5} emu). Ce magnétomètre sera principalement utilisé pour sonder les propriétés induites sous champ dans les systèmes magnétiques frustrés.

Dans une première partie, je détaille le développement de ce magnétomètre. Cela comprend l'optimisation du réfrigérateur à dilution et de bobines de gradient de champ ainsi que le développement d'une détection capacitive avec un étage amplificateur à froid pour améliorer la sensibilité de la mesure. Les mesures magnétiques préliminaires sont présentées. Les changements nécessaires pour rendre le magnétomètre opérationnel sont discutés.

Dans une seconde partie, je présente l'étude expérimentale de systèmes magnétiques frustrés: des grenats de Gadolinium, décrits par des spins classiques, et des composés moléculaires frustrés à base de Cuivre, pour sonder les effets quantiques. Ces mesures ont été réalisées entre 70 mK et 300 K sur les magnétomètres existant à l'Institut Néel.

Dans $Gd_3Ga_5O_{12}$, nous avons complété le diagramme de phases $H - T$. Nous avons montré la robustesse de ce diagramme de phases par notre étude sur le composé isomorphe $Gd_3Al_5O_{12}$. Nous avons mis en évidence la convergence de toutes les phases observées en un unique point dans les deux systèmes. Dans les systèmes quantiques, nous avons réalisé des études préliminaires sur des clusters Cu_{44} à base de tétrèadres, et un système triangulaire Cu_3. Bien que prometteuses, nous n'avons pas approfondi ces études à cause de problèmes d'échantillons.